EFFECTS OF MASS TRANSFER AND CHEMICAL NONEQUILIBRIUM ON SLENDER BLUNTED CONE PRESSURE AND HEAT-TRANSFER DISTRIBUTIONS AT $M_\infty = 13.2$

Clark H. Lewis, J. C. Adams, and G. E. Gilley

ARO, Inc.

December 1968

VON KÁRMÁN GAS DYNAMICS FACILITY
ARNOLD ENGINEERING DEVELOPMENT CENTER
AIR FORCE SYSTEMS COMMAND
ARNOLD AIR FORCE STATION, TENNESSEE

NOTICES

When U. S. Government drawings specifications, or other data are used for any purpose other than a definitely related Government procurement operation, the Government thereby incurs no responsibility nor any obligation whatsoever, and the fact that the Government may have formulated, furnished, or in any way supplied the said drawings, specifications, or other data, is not to be regarded by implication or otherwise, or in any manner licensing the holder or any other person or corporation, or conveying any rights or permission to manufacture, use, or sell any patented invention that may in any way be related thereto.

Qualified users may obtain copies of this report from the Defense Documentation Center.

References to named commercial products in this report are not to be considered in any sense as an endorsement of the product by the United States Air Force or the Government.

EFFECTS OF MASS TRANSFER AND CHEMICAL NONEQUILIBRIUM ON SLENDER BLUNTED CONE PRESSURE AND HEAT-TRANSFER DISTRIBUTIONS AT M_∞ = 13.2

Clark H. Lewis, J. C. Adams, and G. E. Gilley
ARO, Inc.

FOREWORD

The work reported herein was sponsored by NASA Ames Research Center, Moffett Field, California, under NASA Purchase Request A-1369A (RD-6).

The results of research presented were obtained by ARO, Inc. (a subsidiary of Sverdrup & Parcel and Associates, Inc.), contract operator of the AEDC, AFSC, Arnold Air Force Station, Tennessee, under Contract F40600-69-C-0001. The research was conducted from March 1, 1968 to July 15, 1968, under ARO Project No. VW1876, and the manuscript was submitted for publication on August 30, 1968.

The authors are indebted to E. O. Marchand for his assistance in obtaining the ideal gas (γ = 1.4) inviscid blunt body and characteristics solutions, to H. S. Brahinsky for obtaining the nonequilibrium blunt body solution, and to D. H. Wurst for assistance in making the computer calculations and machine plots of the data. The extension of the thermodynamic and transport properties was done by A. W. Mayne. Thanks are due Dr. N. A. Jaffe for indicating an error in the machine program for computing the mixture thermal conductivity which was corrected and the data recalculated.

The free-stream conditions and mass injection rates used in the calculations presented in this report were furnished by Mr. George Lee of NASA Ames Research Center. The required nonequilibrium free-stream composition data were obtained from a nonequilibrium streamtube expansion by ARO, Inc. for the given NASA wind tunnel conditions.

This technical report has been reviewed and is approved.

Eugene C. Fletcher
Lt Col, USAF
AF Representative, VKF
Directorate of Test

Roy R. Croy, Jr.
Colonel, USAF
Director of Test

ABSTRACT

The effects on the pressure and heat-transfer distributions of injecting helium and argon into an air laminar boundary layer over a spherically blunted 7.5-deg half-angle cone at M_∞ = 13.2 and Re_∞/in. = 1520 were considered. Calculations are presented for a binary perfect gas boundary layer including transverse curvature and displacement effects, an ionizing air nonequilibrium boundary layer without higher-order effects, and a nonequilibrium stagnation point thin viscous shock layer model. The effects of inviscid chemical equilibrium and nonequilibrium external conditions and wall catalyticity were investigated. Neglecting all higher-order effects, comparison of binary gas and ionizing air boundary-layer results showed reasonable agreement. Strong effects of inviscid chemical nonequilibrium on stagnation point heat transfer were found. Arguments are given for using inviscid nonequilibrium stagnation conditions rather than the usual chemical equilibrium conditions for nonequilibrium boundary-layer calculations.

CONTENTS

APPENDIXES

I. ILLUSTRATIONS

Figure

NOMENCLATURE

Unless otherwise noted, all lengths are nondimensionalized with respect to the nose radius (see Fig. 1, Appendix I, for cone geometry)

C_{f_∞}	Skin-friction coefficient
C_i	Specie mass fraction
c_p	Constant pressure specific heat
D_{ij}	Binary diffusion coefficient
ECW	Equilibrium catalytic wall
FCW	Fully catalytic wall
f'	Velocity ratio, u/u_e
f''	Velocity gradient, $\partial(u/u_e)/\partial\eta$
g	Stagnation enthalpy ratio
H	Stagnation enthalpy
h	Static enthalpy
j	Diffusive mass flux
k	Thermal conductivity; reaction rate
Le	Lewis number
M	Mach number
$\dot{m}$	Mass flow rate
NCW	Noncatalytic wall
NEQ	Nonequilibrium
Pr	Prandtl number
p	Static pressure
p_o'	Normal shock stagnation pressure

$\dot{q}$	Heat flux
R	Gas constant
Re	Reynolds number
R_n	Nose radius, 1 in.
r	Radius
$\dot{S}$	Net rate of mass production due to surface reactions
s	Surface distance from the forward stagnation point
T	Temperature
TVC	Transverse curvature
U_∞	Free-stream velocity
u	Tangential velocity component
v	Normal velocity component
x	Surface distance
y	Distance normal to the surface
Z	Air specie mass fraction
α	Local body angle
$\gamma, \overline{\gamma}$	Ratio of specific heats
Δ	Shock layer thickness
δ	Boundary-laye. thickness
δ^*	Boundary-layer displacement thickness
δ^*_m	Boundary-layer displacement thickness with mass transfer
ϵ	Density ratio, ρ_∞/ρ_s
η	Transformed distance normal to the surface
θ	Temperature ratio, T/T_e
μ	Dynamic viscosity

ρ	Density
τ	Shear stress

SUBSCRIPTS

e	Edge of boundary layer
eff	At the effective body surface
f	Outer (air) species
i	Injected species
o	Stagnation
s	Normal shock conditions
TVSL	Thin viscous shock layer
w	Wall
∞	Free-stream conditions

SECTION I
INTRODUCTION

The study at the Arnold Engineering Development Center (AEDC), von Karman Gas Dynamics Facility (VKF) of effects of mass transfer into laminar boundary layers at hypersonic wind tunnel conditions began several years ago with the work of Whitfield and Griffith (Ref. 1). They investigated the effects of tangential injection of helium and nitrogen on the zero-lift drag of a 9-deg half-angle cone at $M_\infty \tilde{=} 10$ and 20. The effects of gas injection normal to the surface were investigated by Lewis, Marchand, and Little (Ref. 2) for sharp 9-deg half-angle cones at $M_\infty \tilde{=} 9$ and a 5-deg half-angle cone at $M_\infty = 3.93$ and 5.64. In this latter work, the analysis of mass transfer effects on zero-lift drag was restricted to normal injection of air or nitrogen into an air or nitrogen boundary layer based on the method of Clutter and Smith (Ref. 3). The effects of injecting helium, argon, and carbon dioxide into air or nitrogen sharp cone laminar boundary layers were investigated by Mayne, Gilley, and Lewis (Ref. 4) using the boundary-layer theory of Jaffe, Lind, and Smith (Ref. 5). In Ref. 5, a binary mixture of perfect (nonreacting) gases was considered, and the effects of transverse curvature (TVC) were correctly included whereas the treatment in Ref. 3 was only approximate. (See Ref. 6 for a discussion of the effects of the TVC approximation.)

The effects of mass transfer into a nonreacting air boundary layer were considered by Lewis, et al. (Ref. 7) based on the methods of Jaffe, Lind, and Smith. The effects of nonequilibrium chemistry on the inviscid flow field, and the no-injection ionizing air laminar boundary layer were also considered in Ref. 7. The nonequilibrium laminar boundary-layer theory used in this most recent study was an extension of the method developed and described by Blottner (Ref. 8).

The theoretical models and numerical techniques used in the previous studies have been extended and modified for use in calculations to be discussed in this report. The theoretical models will be described in the following section, and then the conditions used in the calculations will be given. A presentation and discussion of the results of the calculations will be given followed by the concluding remarks.

SECTION II
THEORETICAL MODELS

The inviscid gas models used to describe the outer flow field are presented and discussed below. Next, the binary perfect gas and multicomponent ionizing air boundary-layer models are described. Finally, a thin shock layer model is described for the ionizing air stagnation region with injection of either helium or argon.

2.1 INVISCID FLOW FIELD MODELS

The boundary-layer outer edge properties were obtained from either ideal gas (γ = 1.4) blunt body and characteristics solutions or from a nonequilibrium blunt body solution and a streamtube expansion using an ideal gas (γ = 1.4) blunt body and characteristics solution surface pressure distribution. The binary perfect gas laminar boundary-layer calculations used the ideal gas blunt body and characteristics solutions and the ionizing air boundary-layer calculations used the nonequilibrium blunt body and streamtube expansion data.

2.1.1 Ideal Gas Model

The ideal gas (γ = 1.4) blunt body and characteristics solutions for the geometric, spherically blunted cone were obtained by the method developed by Inouye, Rakich, and Lomax (Ref. 9). The blunt body region was solved by the inverse method described by Lomax and Inouye (Ref. 10) in which the bow shock wave location and shape were iterated until the zero streamline satisfactorily matched the blunt body (sphere) geometry. The numerical scheme is very stable, and blunt body solutions were obtained in about three minutes and the characteristics solutions required about 15 minutes on a CDC 1604B digital computer with an on-line printer.

The blunt body and characteristics solutions over the geometric body perturbed by the displacement thickness (including mass transfer effects) were obtained by the method described by Marchand, Lewis, and Davis (Ref. 11). The method, an extension of the method of Inouye, Rakich, and Lomax (Ref. 9), provides a blunt body solution over the sphere perturbed by the displacement thickness (an ellipsoid) and a least-squares curve fit of the downstream "effective body" defined by $r_{eff} = r_w + \delta^* \cos \alpha$. The method has been found to yield accurate fits of the effective body geometry and smooth numerical results over the entire perturbed body. Some details regarding the procedure used and some results from no-injection calculations are given in Ref. 11.

2.1.2 Inviscid Nonequilibrium Model

Only the nonperturbed inviscid nonequilibrium flow field solution was used in this study. The theoretical model used was the inverse blunt body method of Curtis and Strom (Ref. 12) to obtain the nonequilibrium inviscid stagnation point boundary-layer edge conditions, and the nonequilibrium streamtube program of Lordi, Mates, and Moselle (Ref. 13) was used to obtain the inviscid properties along the boundary-layer edge away from the stagnation point. The ideal gas ($\gamma = 1.4$) blunt body and characteristics solutions provided the surface pressure distribution used in the streamtube expansions. It should be noted that the choice of inviscid nonequilibrium stagnation conditions rather than equilibrium stagnation conditions was made on practical rather than theoretical grounds. In most previous studies, it has been assumed that the correct inviscid stagnation conditions were thermodynamic equilibrium. This model is theoretically correct if the boundary layer is sufficiently thin with respect to the shock layer thickness in the stagnation region. However, if the boundary layer is thick with respect to the shock layer, the conditions at the "edge" will not be, in general, the equilibrium stagnation conditions. In attempting to account for this departure from chemical equilibrium in the stagnation region, the inviscid nonequilibrium blunt body solution method of Curtis and Strom was used to obtain the inviscid stagnation conditions. The stagnation streamline is not included in the blunt body solution method of Ref. 12, and the stagnation point data were obtained from extrapolations of the solution from $s_o = 0.1$ to $s = 0$. The nonequilibrium streamtube expansion was begun at $s = s_o$ with the initial data from the blunt body solution at the same location. Attempts to obtain nonequilibrium solutions over the conical afterbody were not successful, and therefore the pressure distributions used in the streamtube expansions were obtained from the ideal gas ($\gamma = 1.4$) blunt body and characteristics solutions. It should be noted that the nonequilibrium blunt body solution was completely inviscid and did not include the boundary-layer option described by Curtis and Strom (Ref. 12).

The effects of chemical nonequilibrium on the inviscid stagnation conditions were considered. Stagnation point boundary-layer calculations were made using both chemical equilibrium and nonequilibrium inviscid conditions. The effects on the stagnation heat-transfer rate were considered, and the results are presented below.

2.2 VISCOUS FLOW FIELD MODELS

Most of the calculations presented in this report were made using a binary perfect gas, laminar boundary-layer model

including transverse curvature and displacement effects. Limited calculations are presented from an ionizing air, thin laminar boundary-layer theory and a thin viscous shock-layer model. The theoretical models are described below, and the conditions used in the calculations are given in a later section.

2.2.1 Binary Perfect Gas Boundary-Layer Model

The method of Jaffe, Lind, and Smith (Ref. 5) was used to solve the laminar boundary-layer equations including transverse curvature effects for a binary mixture of helium or argon and air. All gases were treated as perfect and, for these calculations, the thermodynamic and transport properties were extended as described in Appendix III.

It was not possible to match all of the wind tunnel free-stream and stagnation conditions with the perfect gas data in the binary gas boundary-layer program. The procedure used was to compute the stagnation enthalpy from $H_\infty = c_p T_\infty + 1/2 M_\infty^2 \gamma R T_\infty$ with $c_p = 6011.6$ ft^2/sec^2-$^\circ$R, $T_\infty = 274^\circ$R, $M_\infty = 13.2$, $\gamma = 1.4$, and $R = 1717.6$ ft^2/sec^2-$^\circ$R. The inviscid normal shock stagnation temperature T_o' was then computed from the thermodynamic properties in the binary gas boundary-layer program, and then an effective specific heat ratio $\bar{\gamma}$ was computed from $\bar{\gamma}/(\bar{\gamma} - 1) = H_\infty/(RT_o')$. The ideal gas ($\gamma = \bar{\gamma}$) normal shock stagnation pressure was calculated from the Rayleigh pitot formula. The results of this procedure are given below:

	Ames Tunnel Conditions	Binary Gas
H_∞, ft^2/sec^2	6.509×10^7	5.9047×10^7
M_∞	13.2	13.2
U_∞, ft/sec	10,850	10,680
T_∞, $^\circ$R	274	290
p_∞, lbf/ft^2	0.1944	0.1944
γ, $\bar{\gamma}$	1.4	1.313
T_o', $^\circ$R	---	8204
p_o', lbf/ft^2	40.4	41.65

The free-stream Mach number and pressure were matched and the remaining quantities were calculated from ideal gas relations. The input conditions at the edge of the boundary layer were obtained from an ideal gas ($\gamma = \bar{\gamma}$) one-dimensional expansion using the ideal gas ($\gamma = 1.4$) blunt body and characteristics solutions. The effects of the mismatch in experimental and theoretical conditions due to the ideal gas model chosen are difficult to determine; however, the results of previous studies such as Whitfield and Griffith (Ref. 1) and Griffith and Lewis (Ref. 14) where both perfect gas and equilibrium air calculations were made indicated small effects due to variations in boundary-layer edge conditions with gas properties.

The procedure used to calculate the effects of boundary-layer displacement is called a first-order treatment. The inviscid outer flow is perturbed by the boundary-layer displacement thickness including the effects of mass transfer δ_m^* through

$$\int_0^{\delta_m^*} \rho_e u_e r \, dy = \int_0^{\delta} (\rho_e u_e - \rho u) r \, dy + \int_0^{x} \rho_w v_w r_w \, dx \qquad (1)$$

where, without mass transfer, the displacement thickness $\delta_m^* = \delta^*$, which is the axisymmetric form of the classical two-dimensional displacement thickness. It should be noted that this is not the definition proposed by Fannelop (Ref. 15) since he neglected higher-order terms which are significant under low density conditions.

The inviscid outer flow sees an effective body defined by

$$r_{eff} = r_w + \delta_m^* \cos \alpha \qquad (2)$$

The effect of displacement was obtained by iterating the inviscid outer flow with the viscous inner flow until there was negligible change in the effective body pressure distribution. Consistent with classical boundary-layer theory, the normal pressure gradient was ignored, and the effects of shock-generated external vorticity, slip, and temperature jump were also not considered in the present study. It has been shown by Lewis (Ref. 6) and Marchand, Lewis, and Davis (Ref. 11) that strong coupling effects can exist between higher-order boundary-layer effects which can significantly affect wall shear stress and heat-transfer rates. However, since numerical methods have not been developed to consider binary gas or ionizing air boundary layers including all the higher-order effects, these first-order results including

tranverse curvature and displacement should provide useful estimates for engineering purposes.

The boundary conditions on the species continuity equations originally proposed by Jaffe, Lind, and Smith (Ref. 5) were later changed (Ref. 16) to agree with the proposal of Baron (Ref. 17). It was originally proposed in Ref. 5 that the concentration of the injected gas be 100 percent at the wall and, of course, zero at the outer edge. Baron proposed that the correct wall boundary condition be zero net flux of the outer flow component (air). Using Baron's idea, the wall boundary conditions on both the specie conservation equation (Z_w) and the energy equation (g_w) are unknown a priori. One must therefore solve for the unknown boundary conditions by iteration using the condition of zero net flux of air at the wall to determine the injected gas specie mass fraction and the mixture enthalpy at the wall. A numerical scheme was developed by Mayne, Gilley, and Lewis (Ref. 4) based on Baron's proposal, and that method was used in the present calculations.

2.2.2 Viscous Nonequilibrium Flow Field Analysis

The determination of the viscous flow field near a body surface requires a detailed calculation of the boundary-layer equations. This task was accomplished through the numerical solution of these governing relations which provide convective heat flux results as well as velocity, temperature, density, and specie concentration profiles across the boundary layer. Furthermore, the effects of inert gas injection into the boundary layer have been included so as to permit study of the transpiration cooling problem under nonequilibrium conditions.

The computer program used to solve the boundary-layer equations employs a highly modified version of the method developed by Blottner (Ref. 8) to study nonequilibrium, nonsimilar, laminar boundary-layer flows over both blunt and sharp-nosed bodies of revolution as well as sharp plates and wedges. All basic portions of Blottner's analysis have been retained, e.g., consideration of the diffusive mass flux for a multicomponent mixture of perfect gases and expressing the net mass rate of production for each specie in a form especially suited for numerical computation. For further details on the theoretical formulation of the governing equations, see Blottner (Refs. 18 and 19) and Lenard (Ref. 20).

In order to examine the effects of inert gas injection into a nonequilibrium boundary layer, the wall boundary conditions for the governing specie conservation equations must be modified to allow mass transfer through a porous surface.

Following Chung (Ref. 21) and Moore and Lee (Ref. 22), the solid boundary (wall) was viewed as a rigid semipermeable membrane which does not permit the air species to flow into the pores but does allow the inert species to flow into the boundary layer. Although chemically inert, many surfaces can act as a catalyst for the recombination of oxygen and nitrogen atoms in a dissociated mixture so that a catalytic wall boundary condition must also be considered. Moore (Ref. 23), in an appendix to his thesis, discusses and formulates these boundary conditions for two different cases with inert gas injection, one in which the wall is taken to be completely noncatalytic with respect to atom recombination and the other in which local chemical equilibrium is assumed to exist at the gas-solid interface. In the absence of mass transfer these two boundary conditions reduce to the noncatalytic and equilibrium wall conditions, respectively, formulated by Blottner and Lenard (Ref. 24). Hence, Moore's formalism of the wall boundary conditions for the species may be considered general and used both with and without mass transfer effects; these boundary conditions were used in the present study by adding them to the computer program. The outer edge boundary conditions were obtained from the nonequilibrium blunt body and streamtube expansion as discussed previously. In addition, the usual conditions of no slip and temperature jump at the surface and a prescribed constant wall temperature ($540^{\circ}R$) were made.

In addition to the wall and outer edge boundary conditions, initial conditions are required to completely determine the resulting downstream solution. In order to obtain the correct initial conditions, the system of boundary-layer equations (which are nonlinear partial differential equations) was reduced to the limiting form of ordinary nonlinear differential equations with two-point boundary conditions at the stagnation point. Such two-point boundary value problems are extremely difficult to solve using the more common "shooting" method since so many specie equations are involved. Hence, a finite-difference method was developed such that the two-end conditions were always satisfied; the fundamentals of this technique may be found in Chapter VII of the book on numerical analysis by Conte (Ref. 25). More details of this finite-difference technique applied to the solution of nonlinear equations may be found in the papers by Holt (Ref. 26) and Fay and Kaye (Ref. 27). Basically, the nonlinear ordinary differential equations were written in linearized finite-difference form so that the resulting linear algebraic equations are of tridiagonal form and a sweeping method of solution was used. Iteration was then applied until successive solutions ($f'(\eta)$, $\theta(\eta)$, and $C_i(\eta)$) were sufficiently close to each other. This procedure was found to converge rapidly for all cases in the present study.

Using the above-obtained initial conditions, solutions to the complete nonsimilar boundary-layer equations were obtained in a step-by-step procedure marching downstream using the implicit finite-difference method by Blottner which was mentioned previously. No stability problems were encountered, either with or without mass transfer, for the conditions studied.

Considerations have also been given to the possibility that a boundary-layer-type analysis may not be valid under the conditions of the present study. It may be that nonequilibrium and viscous effects have equal importance over the entire shock layer, especially in the nose region of the body. In order to examine this possibility, an analysis has been performed where the entire shock layer at the stagnation point was treated as viscous. As shown by Cheng (Ref. 28), Chung (Ref. 29), Inger (Ref. 30), Howe and Viegas (Ref. 31), and Lee and Zierten (Ref. 32), the governing equations for such an analysis are identical in form with the boundary-layer equations under the restrictions that the shock layer be thin, i.e., $\Delta \ll 1$, with all curvature effects neglected. Recent work by Howe and Sheaffer (Ref. 33), Goldberg (Ref. 34), Goldberg and Scala (Ref. 35), and Chen, et al. (Ref. 36), has further shown the validity of such an analysis for cases with mass injection at the wall.

The basic thin, hypersonic shock layer model as formulated by Cheng assumes a strong bow shock wave of negligible thickness that is concentric with the body at the stagnation line. Across the shock, the static pressure and normal velocity components are discontinuous according to the usual Rankine-Hugoniot relations; in addition, the so-called "shock slip" effects (discontinuities in composition, tangential velocity, and total enthalpy) are allowed immediately behind the shock. Between the shock and the body there is assumed a thin ($\Delta \ll 1$) layer of continuum, viscous reacting gas flow. In this layer, the influence of body curvature and surface slip phenomena are also neglected in comparison to the shock layer vorticity and "shock slip" effects, provided the body surface is highly cooled. An important consequence of this thin, hypersonic shock layer model is that the governing Navier-Stokes equations reduce to the familiar parabolic partial differential equations of boundary-layer theory as mentioned previously.

For application in the present study, a modification of the above model was adopted. Across the shock, the static pressure, enthalpy, and normal velocity component were taken to be discontinuous according to the Rankine-Hugoniot conditions for a real gas. However, through the shock the chemical composition was taken as frozen at the free-stream

conditions. Furthermore, stagnation or total enthalpy was taken as constant across the shock. Hence, none of the so-called "shock slip" effects was considered in the current work. Other than this, all other features of the thin, hypersonic shock layer were retained including the centrifugal effects due to a normal pressure gradient across the layer. Between the shock and the body the flow was considered to be in chemical nonequilibrium with the shock standoff distance determined as part of the solution. Effects of inert gas injection into the shock layer were also included for both noncatalytic and catalytic wall conditions. The program itself is basically the same as the stagnation point boundary-layer program described previously since the only modifications were to permit determination of the shock standoff distance and the inclusion of the normal pressure gradient terms. The manner of iterative solution was exactly the same as in the boundary-layer case. Future plans include the addition of "shock slip" effects to this program since only with this capability can the low Reynolds number regime of high altitude hypersonic flight be explored.

SECTION III
CONDITIONS USED IN THE CALCULATIONS

The free-stream and stagnation conditions used in the binary gas boundary-layer calculations are given in Table I (Appendix II). The injection rates were assumed constant and are given below:

Injected Gas	Binary Gas	Ionizing Air
Argon ($\rho_w v_w$, lbf-sec/ft^3)	11.82×10^{-5}	11.82×10^{-5}
Helium ($\rho_w v_w$, lbf-sec/ft^3)	3.08×10^{-5}	3.08×10^{-5}
Argon ($\rho_w v_w / \rho_\infty u_\infty$)	0.0284	0.0268
Helium ($\rho_w v_w / \rho_\infty u_\infty$)	0.0074	0.0070

It will be shown later that the higher injection rate of the argon had a significant effect on the numerical results.

The porous-wall temperature was assumed constant at $T_w = 540^\circ R$.

The wall and outer-edge specie mass fractions for the ionizing air boundary layer and shock layer are given in Tables II through IV. Where computed, both equilibrium catalytic wall and noncatalytic wall conditions are given. The equilibrium wall conditions were computed from the equilibrium composition at the wall (or outer edge) pressure and wall temperature. With injection the added constraint of zero net flux of the air species at the wall was imposed. The frozen normal shock specie mass fractions for the thin viscous shock layer are equivalent to the free-stream mass fractions.

For comparison of the effects of equilibrium and non-equilibrium inviscid outer edge conditions, no-injection thin boundary-layer calculations were made with both sets of conditions and the inviscid outer edge mass fractions are given in Table II.

The chemical reaction rate constants used in the non-equilibrium boundary-layer and shock-layer calculations are given in Table V.

SECTION IV
RESULTS AND DISCUSSION

4.1 BINARY GAS RESULTS

The results from the binary perfect gas, laminar boundary-layer calculations including the effects of displacement and transverse curvature are shown in Figs. 2-7 for the no-injection conditions, in Figs. 8-14 for the argon-injection conditions, and in Figs. 15-21 from the helium-injection calculations.

The effects of displacement on all quantities plotted can be seen by comparison of the last iteration (e.g. second iteration without injection) value with the zeroth-iteration results. The convergence of the solutions with displacement can be seen by comparison of (n + 1)- with n-iteration results. From the results shown in Figs. 8-13, it is clear that the convergence of the calculations for the displacement effect with argon injection were much slower (i.e., more iterations were required for negligible change between iterations) than either the helium* or no-injection calculations.

*Because of an error pointed out to the authors by Dr. N. A. Jaffe, the helium-injection calculations were corrected and only the zeroth and final interation results are shown. The error had negligible effect on the argon-injection results.

The higher injection rate used in the argon calculation caused the slower convergence. It should be noted that difficulty was encountered in making the first-iteration argon injection calculation at s = 4.32 which caused the calculation to be terminated at that point. The effective body data were extrapolated over the remainder of the body, and the calculation was continued for the second iteration. This difficulty with high injection rates was encountered in the earlier sharp cone studies of Lewis, Marchand, and Little (Ref. 2) and Mayne, Gilley, and Lewis (Ref. 4), and the extrapolation procedure used in the present study was also used successfully in the previous studies.

The primary interest in the present investigation was in the predictions of heat-transfer and pressure distributions over the cone with and without injection. The heat-transfer distributions are shown in dimensional (Btu/ft^2-sec) and two-dimensionless forms ($\dot{q}/\rho_\infty U_\infty^3$ and $\dot{q}/\dot{q}(0)$). The data are not shown in the form of the Stanton number since the enthalpy of the gas mixture at the wall is a function of the concentration of the injected gas at the wall which is unknown a priori. Also the driving potential for heat transfer is not simply the enthalpy difference when injection or chemical reactions are considered but is a more complicated function. An alternate and somewhat preferable nondimensional heat-transfer coefficient is $\dot{q}/\rho_\infty U_\infty^3$, which is useful in scaling results for small variations in free-stream conditions. The commonly used ratio $\dot{q}/\dot{q}(0)$ is also given.

The mass fractions of the injected gases (argon and helium) at the wall are shown in Figs. 14 and 21. The high uniform injection rate of the argon increased the mass fraction of argon from 0.14 at the stagnation point to 0.85 at the end of the body, whereas the variation in helium mass fraction increased from 0.025 at s = 0 to 0.44 at s = 5.10. It has been observed previously that blowoff of the boundary layer (i.e., where $\tau_w \sim f''_w \rightarrow 0$) is related to the concentration of the injected gas approaching 100 percent when uniform surface mass transfer is considered.

The effects of injection on the heat-transfer are shown in Fig. 22 with a plot of the ratio of heat transfer with helium or argon injection to the no-injection heat-transfer rate. Both displacement and transverse curvature effects were included in the injection and no-injection calculations with the final iteration results used in all cases. The higher injection rate of the argon is seen to substantially reduce the heat-transfer rate in comparison with the helium injection results.

Attention is directed to the increase in heat-transfer in the stagnation region ($s < 0.85$) with helium injection over the no-injection heat-transfer rate as shown in Fig. 22. Some of the quantities affecting the wall heat-transfer rate are given below:

	Helium Injection	No Injection
T_w, ^oR	540	540
ρ_w, slugs/ft^3	3.93216×10^{-5}	4.49397×10^{-5}
μ_w, lbf-sec/ft^2	3.5938×10^{-7}	3.50729×10^{-7}
c_{p_w}, ft^2/sec^2-R	6593	6019
Pr_w	0.60447	0.73725
Le_w	2.8649	1.00
k_w, lbf/sec-^oR	3.9198×10^{-3}	2.8634×10^{-3}
Z_w	0.97705	1.00
Z_w'	0.003347	0.0
g_w	0.060274	0.055026
g_w'	0.205042	0.2158078
$\dot{q}$, ft-lbf/ft^2-sec	38,146	36,205
$(\partial T/\partial y)_w$	0.81×10^6	1.06×10^6
$(\partial Z/\partial y)_w$	1.466	0.0

The heat-transfer rate to the wall with or without mass transfer is shown in Appendix IV to be $\dot{q}_w = (k\ \partial T/\partial y)_w$ for a nonreacting binary gas mixture. For this condition, mass transfer can only affect the wall heat transfer through the mixture thermal conductivity and temperature gradient. Considering the ratio

$$\frac{\dot{q}_{He\ inj}}{\dot{q}_{no\ inj}} = \frac{(k\ \partial T/\partial y)_{He\ inj,w}}{(k\ \partial T/\partial y)_{no\ inj,w}}$$

and the data given above, one finds the ratio to be 1.05 in good agreement with the results shown in Fig. 22. For the case of helium injection, it is thus seen that the increase

in thermal conductivity of the gas mixture at the wall is greater than the reduction in the temperature gradient at the wall. This interesting result was also found by Anfimov (Ref. 37) for injection of low molecular weight gases (He and H_2) into a nonreacting binary gas mixture. In agreement with the results given later in this report, he did not find the increase in stagnation point heat transfer when He was injected into a reacting air mixture. This phenomenon appears to be confined to low injection rates of low molecular weight gases into nonreacting binary gas mixtures. It will be of special interest to compare these results with experimental heat-transfer data to determine the magnitude and direction of the change in surface heat-transfer rate with low injection rates of helium.

4.2 NONEQUILIBRIUM FLOW FIELD RESULTS

4.2.1 Stagnation Point

It is instructive first to examine the stagnation point solutions. Information concerning the no mass injection condition is shown in Table II. These basic sets of solutions are shown: a boundary-layer model which used the nonequilibrium inviscid outer edge specie concentrations, a boundary-layer model which used equilibrium outer edge specie concentrations as computed from equilibrium considerations at the given p_o' and T_o' (note that these are perfect gas values) with reference mass fractions $C_{O_2}^{(ref)} = 0.23456$ and $C_{N_2}^{(ref)} = 0.76544$, and a thin viscous shock-layer model using the conditions behind the chemically frozen (free-stream composition) normal shock. Note the large difference in outer edge specie concentrations between the boundary-layer nonequilibrium and equilibrium cases; the equilibrium values for oxygen are highly dissociated and slightly dissociated for nitrogen, whereas the nonequilibrium values are essentially frozen at their free-stream level for which the oxygen was slightly dissociated. This rather striking difference becomes strongly reflected in the stagnation point heat-transfer results for the fully catalytic wall condition. However, before examining this, a review of various wall conditions and their interpretation is in order.

As used here, the fully catalytic wall (FCW) condition is taken to mean that the wall is perfectly catalytic with respect to atom recombination so that only the basic molecular species oxygen and nitrogen exist at the surface. Further, it is assumed that the values for oxygen and nitrogen composition at the wall are exactly the same as the outer edge reference values used in the equilibrium composition calculation.

Such is purely an assumption since in the case of a multicomponent gas the basic element mass fractions may change due to multicomponent diffusion across a nonisothermal layer. This assumption can only be justified a posteriori by examining the complete multicomponent formalism for equilibrium catalytic wall (ECW) boundary conditions. Such has been done for the thin viscous shock layer case, and the results are shown in Table VI. It is seen that the fully catalytic wall assumption is certainly valid for this case; repetition of the equilibrium wall calculations for the boundary-layer cases established the same conclusion with respect to the fully catalytic wall assumption for these conditions. It should be pointed out that the validity of this assumption is due mainly to the extremely cold wall temperature (540°R) used throughout this analysis. As the wall temperature is increased, the fully catalytic wall assumption will lose its validity and recourse must be taken to the multicomponent equilibrium wall formalism.

An alternate boundary condition for the species is the noncatalytic wall (NCW) restriction. Here no atom recombination is allowed on the surface, and thus the atoms tend to "pile up" near the wall, creating a "blanketing" effect. The model surface will exhibit characteristics somewhere between the two limiting extremes described above, i.e., a finite surface catalyticity with respect to atom recombination. This condition, which is difficult to treat due to lack of knowledge concerning surface catalyticity effects, has not been considered in the present analysis since the fully catalytic (or equilibrium) wall and the noncatalytic wall form an upper and lower bound, respectively, on the heat-transfer rate with respect to atom recombination on the surface.

Since the noncatalytic wall condition allows no atom recombination on the surface, the wall heat transfer can be materially reduced for cases involving high dissociation (and ionization) levels in the gas. An excellent example of this effect may be seen in the boundary-layer solution with equilibrium outer edge conditions. Note the factor of two difference in the stagnation point heat flux; this is due to the recombination of atoms on the surface in the fully catalytic wall case as opposed to no recombination on the surface in the noncatalytic wall case under conditions of high dissociation levels at the outer edge of the boundary layer. Such does not occur in the boundary-layer case with a nonequilibrium outer edge because here the dissociation level is very low, which is reflected in a very modest increase in stagnation point heat flux for the fully catalytic wall condition in comparison with the noncatalytic wall conditions. It should be further noted that the flow is essentially frozen between the outer edge and the wall for the noncatalytic wall condition, and this will be shown later in the

discussion. The important fact to be gained from the above is that the assumption on the outer edge condition (either equilibrium or nonequilibrium) can be controlling with respect to the resulting stagnation point heat flux. Hence, one should try to determine the best choice for the outer edge condition from some independent source if possible. The thin viscous shock layer analysis provides such a tool.

Since the thin viscous shock layer (TVSL) analysis treats the flow field as fully viscous and in chemical nonequilibrium between the shock and the body, there is no arbitrary choice as to the location of some "edge" (with its corresponding conditions) since the shock standoff is now obtained as part of the solution. The only restriction made is that the normal shock crossing be chemically frozen with translational, rotational, and vibrational modes in equilibrium immediately behind the shock. Reference to Table II shows that the stagnation point heat fluxes are in good agreement with the nonequilibrium outer edge boundary-layer results for both wall conditions. This agreement may be interpreted as evidence that perhaps the outer edge of the boundary-layer analysis should properly be treated as a nonequilibrium condition. It should be noted, however, that vorticity is included in the viscous shock layer model (increasing the heat-transfer rate) and not in the classical boundary-layer model. Thus, the good agreement in wall heat-transfer between the two models must be viewed with caution. Of course, one may even question the applicability of a thin viscous shock layer treatment for the present set of conditions. In order to verify this analysis, the shock Reynolds number, Re_s, must be examined. For the particular set of free-stream conditions shown in Table I, $Re_s = 149.93$ based on body nose radius; the corresponding density ratio, ϵ, across the frozen normal shock was $\epsilon = 0.1389$ with static pressure $p_s = 41.471$ lbf/ft^2 and static temperature $T_s = 8069.2^\circ$R immediately behind the shock. As shown by Cheng (Ref. 28), the conditions for validity of a thin viscous shock layer model are $(1/\epsilon Re_s) \ll 1$, $\Delta = 0(\epsilon) \ll 1$ and $\epsilon M_\infty^2 \gg 1$. For the present conditions

$$1/\epsilon Re_s = 1/(149.93 \times 0.1389) \doteq 0.0480 \ll 1$$

$$\Delta = 0(\epsilon) = 0(0.1389) \ll 1$$

$$\epsilon M_\infty^2 = (0.1389)(13.2)^2 = 24.2019 \gg 1$$

which satisfy these criteria and, hence, justify a thin viscous shock layer analysis. Thus, it is believed that the thin viscous shock layer is an applicable model upon which to assess the validity of a boundary-layer-type model by comparison of solutions.

From Table II it is seen that the inviscid shock standoff Δ is 0.1091 for the inviscid nonequilibrium solution, 0.1095 for the inviscid perfect gas solution, and 0.0753 or 0.0758 for the thin viscous shock layer fully catalytic and noncatalytic wall, respectively. The reduction in shock layer thickness for the thin viscous shock layer cases is due to the large density gradients near the cold wall which tend to thin the layer. For the boundary layer with nonequilibrium outer edge, the boundary-layer thickness δ (defined to be the y location where $f' = 0.995$) is seen to be 0.0695 and 0.0696 for the fully catalytic and noncatalytic wall, respectively. Hence, the viscous boundary-layer occupies about 65 percent of the inviscid shock layer; note further that the boundary-layer thickness is slightly less than the thin viscous shock-layer thickness. All of these factors contribute to the possibility that a boundary-layer-type analysis is indeed a valid model for the present body and set of conditions.

With respect to mass addition at the stagnation point, Tables III and IV show results for the injection of argon and helium, respectively. First note that the injected mass flux for helium is roughly one order or magnitude less than for argon; such has an important effect on the results which follow. In all equilibrium catalytic wall (ECW) calculations, the complete multicomponent equilibrium wall boundary condition including mass injection of an inert specie was used. It is seen that helium injection had a very small influence on the heat flux, boundary-layer thickness, and shock-layer thickness due to the small injection rate. Argon had a larger influence with a slight thickening of both boundary and shock layers due to the mass addition.

For purposes of comparison it is instructive to consider the stagnation point heat flux for the thin viscous shock layer relative to the nonequilibrium boundary-layer using inviscid nonequilibrium outer edge conditions. Such has been done in Table VII where corresponding wall conditions have been matched, e.g., boundary layer with noncatalytic wall to thin viscous shock layer with noncatalytic wall conditions. Also shown are results from Goldberg (Ref. 34), who employed a viscous shock layer model in complete chemical equilibrium, and Cheng (Ref. 28), who used a perfect gas viscous shock layer with $\epsilon = 0.13$, $M_\infty \rightarrow \infty$, and a highly cooled wall. The increase in heat transfer at the stagnation point is due mainly to vorticity interaction which is accounted for in the thin viscous shock layer solution but neglected in the boundary-layer solution. This vorticity effect manifests itself through a finite gradient in the streamwise velocity near the outer edge of the shock layer. Such can be seen in Fig. 23 which shows comparisons of the thin viscous shock layer velocity and temperature profiles with respect to

corresponding nonequilibrium boundary-layer profiles using nonequilibrium inviscid outer edge conditions. The fuller characteristic of the boundary-layer velocity profile is a direct consequence of imposing a zero gradient (no external vorticity) on the velocity profile at the outer edge. Although Fig. 23 is for a noncatalytic wall without mass injection, the results are typical for all cases, even including mass injection. Figure 24 shows the specie distributions at the stagnation point from the viscous shock layer analysis; note that both wall conditions (with and without mass injection) are presented. The important fact to be gained from these profiles is that the flow field remains essentially frozen in all cases. There are no regions of extreme chemical production or depletion due to nonequilibrium phenomena, and hence multicomponent diffusion of species is the predominant mass transport mechanism. Note, however, that for the case of an equilibrium catalytic wall, both with and without mass injection, there is a region very near the surface which is highly influenced by the wall catalyticity condition, which is to be expected.

Much of the foregoing has been concerned with trying to establish whether a boundary-layer analysis is valid for the present body and set of conditions and, if so, what the correct outer edge conditions should be. At this point it is well to summarize our findings since this question is of fundamental importance. With respect to the outer edge conditions for the boundary-layer analysis, it was shown that the stagnation point heat flux was highly dependent on whether the outer edge was taken to be in chemical equilibrium or nonequilibrium; furthermore, the wall catalyticity (equilibrium catalytic or noncatalytic) was of equal importance since it controlled the energy transfer due to atom recombination on the body surface. Based on this information alone, one cannot determine the more correct outer edge condition and, hence, some other source must be consulted. The thin viscous shock layer provided us with such a tool. For the body and set of conditions under examination, it was shown that a thin viscous shock layer analysis was applicable. Comparison of stagnation point heat fluxes (shown in Table II) revealed that the nonequilibrium outer edge boundary-layer conditions were in good agreement with the thin viscous shock layer for both wall catalyticities with the thin viscous shock layer having the higher heat flux value due to the inclusion of vorticity interaction which was not considered in the boundary-layer treatment. Furthermore, it was shown that the boundary-layer thickness with nonequilibrium outer edge conditions was about 65 percent of the inviscid shock layer thickness, i.e., $\delta/\Delta_{inviscid} \approx 0.65$, as well as being thinner than the thin viscous shock layer thickness, $\delta/\Delta_{TVSL} \approx 0.92$. Based on these results it is felt that the boundary-layer

analysis which used the nonequilibrium outer edge conditions is indeed applicable to the present problem. We believe these findings and conclusions to be of considerable importance and interest since, to our knowledge, prior investigations have used equilibrium outer edge conditions exclusively with no consideration given to their validity on physical grounds.

The above discussion was concentrated solely on the stagnation point where it was shown that a boundary-layer analysis was indeed applicable to the present problem. Hence, solutions have been obtained over the complete body using the nonsimilar, nonequilibrium boundary-layer program described earlier. These results will now be presented.

4.2.2 Downstream Region

One of our primary objectives in this work concerned the effects of inert gas injection on various boundary-layer parameters. Hence, a measure of the inert gas concentration at the wall is of interest since it essentially controls the inert gas influence on the boundary layer. Figure 25 shows the wall concentration of the air species defined by $Z_w = 1 - C_{w,\text{inert gas}}$, and thus the more inert gas present at the wall, the smaller the value for Z_w. The important point to note here is the large influence of wall catalyticity on inert gas concentration over the downstream region of the body. Near the end of the body the noncatalytic wall condition gives a 40- to 85-percent increase in the inert gas concentration at the wall as compared to the equilibrium catalytic wall condition. This is both surprising and enlightening.

One would expect the mass injection process to have a thickening effect on the boundary-layer displacement thickness. Such is true as shown in Fig. 26. Note first that for the case of no mass injection, the effect of wall catalyticity is negligible. Such is not true with inert gas injection; here the noncatalytic wall condition has a much larger displacement effect than does the equilibrium catalytic wall in the downstream region. Considering the way that viscous interaction involves the displacement thickness, one should expect larger viscous interaction effects for the noncatalytic wall condition than for the equilibrium catalytic wall with mass injection.

Turning now to the heat-transfer results, Figs. 27 and 28 show the heat flux distributions for all conditions over the entire body. It is seen that the noncatalytic wall reduces the heat flux as expected and by a substantial amount in the case of argon injection. It is interesting to note that the difference between the equilibrium catalytic wall and

noncatalytic wall results remains essentially constant over the entire body for the no-mass-injection condition. For cases with mass injection, the type of plot shown in Fig. 29 is instructive since it shows directly the reduction in heat flux due to mass addition relative to the no-injection result for a given wall catalyticity. Here the effectiveness of argon injection with a noncatalytic wall becomes immediately apparent. Hence, it is clear that it is highly desirable to have noncatalytic surfaces if one desires to substantially reduce the wall heat transfer by normal injection of an inert gas (transpiration cooling) into a nonequilibrium boundary layer.

It is also of interest to examine the skin-friction distribution shown in Fig. 30. For the case of no mass injection, there is no influence due to wall catalyticity on the skin friction. However, when mass injection is considered, the noncatalytic wall reduces the skin friction as compared with the equilibrium catalytic wall. Since the skin-friction drag results from integrating the wall shear stress distribution over the body, the possibility of reducing such drag by injection of an inert gas is well-known. Table VIII shows this reduction in skin-friction drag with inert gas injection; as expected, the noncatalytic wall condition results in the lower drag for both gases.

In summary, the above discussion has pointed out the possibility of reducing both heat transfer and skin friction by injection of an inert gas (argon or helium in this case). In addition, a further reduction in both heat transfer and skin friction is possible with such inert gas injection by using a noncatalytic surface as opposed to an equilibrium catalytic surface. However, such a choice will increase the resulting boundary-layer displacement thickness which could result in larger viscous interaction effects. Hence, some sort of a "tradeoff" may prove desirable in future applications.

4.3 COMPARISON OF BINARY GAS AND NONEQUILIBRIUM FLOW FIELD RESULTS

A comparison of the binary gas and nonequilibrium ionizing air boundary-layer results is shown in Fig. 31. For purposes of this comparison, binary gas calculations were made without transverse curvature and displacement effects.

The comparison shows good agreement for all the quantities plotted in Fig. 31 for the case of no mass injection. Smaller differences in the calculated results were found for the case of helium injection than for argon injection. The effects of the higher injection rate of argon on the

displacement thickness comparison can be seen in Fig. 31a. Some of the difference in the calculated heat-transfer rates is removed when the slight variation in free-stream conditions is included. This can be seen by comparison of the differences in calculated dimensional heat-transfer rate in Fig. 31c with the dimensionless heat-transfer rate $\dot{q}/\rho_\infty U_\infty^3$ shown in Fig. 31e.

The relatively good agreement between these binary gas and ionizing air boundary-layer results should support the confidence in the binary gas results including transverse curvature and displacement. The scope of these calculations did not include ionizing air boundary-layer calculations with higher-order boundary-layer effects. The reacting gas boundary-layer calculations were made to assess the effects of nonequilibrium chemistry without higher-order boundary-layer effects and thus would be useful in interpreting the binary gas boundary-layer calculations. The comparisons in Fig. 31 show a measurable nonequilibrium effect on the heat transfer with argon injection near the end of the conical afterbody. Some of the difference between binary gas and ionizing air calculated heat-transfer results might be reduced if transverse curvature and displacement were included in the ionizing air model. Therefore, the effects of nonequilibrium chemistry cannot be predicted accurately from these calculations and comparisons.

4.4 EFFECTS OF WALL TEMPERATURE

The effects of wall temperature on the stagnation point heat-transfer rate for the binary gas and ionizing air boundary-layer models without mass transfer are shown in Fig. 32. Since the experimental no-injection wall temperature may not have been the assumed value of 540°R (the same as the wall temperature conditions with injection), it was considered desirable to investigate the effects of wall temperature variation. The change in heat-transfer rate with wall temperature was small for $540 \leq T_w \leq 700$°R and the rate of change was approximately constant for $800 \leq T_w \leq 1500$°R where the upper limit was the maximum value considered. With the data shown in Fig. 32, it is possible to correct the ratio $\dot{q}_{inj}/\dot{q}_{no\ inj}$ shown in Figs. 22 and 29 for the effect of wall temperature. It is interesting to note that for the range of wall temperatures considered the difference between equilibrium catalytic wall (ECW) and noncatalytic wall (NCW) heat transfer remained essentially constant, and similarly for $T_w > 800$°R the difference between the nonreacting binary gas and ionizing air with NCW was insensitive to wall temperature.

SECTION V
CONCLUDING REMARKS

Binary gas laminar boundary-layer calculations were made including mass transfer, transverse curvature, and displacement effects. Nonequilibrium ionizing air boundary layer and stagnation point thin viscous shock layer calculations were made including mass transfer and catalytic wall effects. The comparison of binary gas and ionizing air boundary-layer results including mass transfer but excluding higher-order boundary-layer effects showed reasonably good agreement except in the case of argon injection and supported the use of the binary gas results including transverse curvature and displacement effects. The data were presented to aid in making comparisons between the calculated results and experimental data. Final assessment of the applicability of the theoretical models used and the numerical results obtained must await such comparison with experimental data currently unavailable.

REFERENCES

1. Whitfield, J. D. and Griffith, B. J. "Hypersonic Viscous Drag Effects on Blunt and Slender Cones." AIAA J., Vol. 2, No. 10, October 1964, pp. 1714-1722.

2. Lewis, C. H., Marchand, E. O., and Little, H. R. "Mass Transfer and First-Order Boundary-Layer Effects on Sharp Cone Drag." AIAA J., Vol. 4, No. 10, October 1966, pp. 1697-1703 and AIAA J., Vol. 4, No. 11, November 1966, pp. 1954-1960.

3. Clutter, D. W. and Smith, A. M. O. "Solution of the General Boundary-Layer Equations for Compressible Laminar Flow, Including Transverse Curvature." Douglas Aircraft Company Report LB 31088, 1963; revised 1964. See also AIAA J., Vol. 3, 1965, pp. 639-647.

4. Mayne, A. W., Gilley, G. E., and Lewis, C. H. "Binary Boundary Layers on Sharp Cones in Low Density Supersonic and Hypersonic Flow." AIAA Paper 68-66 presented at the Sixth AIAA Aerospace Sciences Meeting, New York, New York, January 1968.

5. Jaffe, N. A., Lind, R. C., and Smith, A. M. O. "Solution to the Binary Diffusion Laminar Boundary Layer Equations Including the Effect of Second-Order Transverse Curvature." AEDC-TR-66-183 (AD 647285), February 1967.

6. Lewis, C. H. "Comparison of a First-Order Treatment of Higher-Order Boundary-Layer Effects with Second-Order Theory and Experimental Data." University of Tennessee Ph.D. dissertation, June 1968.

7. Lewis, C. H., Adams, J. C., Brahinsky, H. S., et al. "Effects of Nonequilibrium and Mass Transfer on a Blunt Ogive Pressure Distribution." AEDC-TR-68-31 (AD 666910), March 1968.

8. Blottner, F. G. "Nonequilibrium Laminar Boundary Layer Flow of Ionized Air." AIAA J., Vol. 2, No. 11, November 1964, pp. 1921-1927.

9. Inouye, M., Rakich, J. V., and Lomax, H. "A Description of Numerical Methods and Computer Programs for Two-Dimensional and Axisymmetric Supersonic Flow over Blunt-Nosed and Flared Bodies." NASA TN D-2970, August 1965.

10. Lomax, H. and Inouye, M. "Numerical Analysis of Flow Properties about Blunt Bodies Moving at Supersonic Speeds in an Equilibrium Gas." NASA TR R-204, July 1964.

11. Marchand, E. O., Lewis, C. H., and Davis, R. T. "Second-Order Boundary-Layer Effects on a Slender Blunt Cone at Hypersonic Conditions." AIAA Paper 68-54, January 1968.

12. Curtis, J. and Strom, C. "Computations of a Nonequilibrium Flow of a Viscous, Radiating Fluid about a Blunt Axisymmetric Body." AFFDL-TR-67-40, June 1967.

13. Lordi, J., Mates, R. E., and Moselle, J. R. "Computer Program for the Numerical Solution of Nonequilibrium Expansions of Reacting Gas Mixtures." CAL-AD-1689-A-6, October 1965.

14. Griffith, B. J. and Lewis, C. H. "Laminar Heat Transfer to Spherically Blunted Cones at Hypersonic Conditions." AIAA J., Vol. 2, No. 3, March 1964, pp. 438-444. See also AEDC-TDR-63-102 (AD 408568), June 1963.

15. Fannelop, T. K. "Displacement Thickness for Boundary Layer with Surface Mass Transfer." AIAA J., Vol. 4, No. 5, June 1966, pp. 1142-1144.

16. Jaffe, N. A., Lind, R. C., and Smith, A. M. O. "Solution to the Binary Diffusion Laminar Boundary-Layer Equations with Second-Order Transverse Curvature." AIAA J., Vol. 5, No. 9, September 1967, pp. 1563-1569.

17. Baron, J. R. "The Binary Mixture Boundary Layer Associated with Mass Transfer Cooling at High Speeds." MIT Naval Supersonic Lab TR 16, May 1956.

18. Blottner, F. G. "Nonequilibrium Laminar Boundary Layer Flow of a Binary Gas." GE TIS R63SD17, June 1963.

19. Blottner, F. G. "Nonequilibrium Laminar Boundary Layer Flow of Ionized Air." GE TIS R64SD56, November 1964.

20. Lenard, M. "Chemically Reacting Boundary Layers." GE TIS R64SD14, March 1964.

21. Chung, P. M. "Chemically Reacting Nonequilibrium Boundary Layers." Advances in Heat Transfer, Vol. 2, Academic Press, Inc., 1965, pp. 109-270.

22. Moore, J. A. and Lee, J. T. "Discontinuous Injection of Inert Gas into the Nonequilibrium Laminar Boundary Layer." TRW 06388-6018-R000, July 1967.

23. Moore, J. A. "Chemical Nonequilibrium in Viscous Flows." Ph.D. dissertation, State University of New York at Buffalo, May 1967.

24. Blottner, F. G. and Lenard, M. "Finite Rate Plasma Generation in the Laminar Air Boundary Layer of Slender Re-Entry Bodies." Paper presented at the Eight Symposium on Ballistic Missile and Space Technology, San Diego, California, 16-18 October 1963.

25. Conte, S. D. Elementary Numerical Analysis. McGraw-Hill, Inc., 1965.

26. Holt, J. F. "Numerical Solution of Nonlinear Two-Point Boundary Problems by Finite Difference Methods." Assoc. for Computing Mach. Communications, Vol. 7, No. 6, June 1964, pp. 366-373.

27. Fay, J. A. and Kaye, H. "A Finite-Difference Solution of Similar Nonequilibrium Boundary Layers." AIAA J., Vol. 5, No. 11, November 1967, pp. 1949-1954.

28. Cheng, H. K. "The Blunt-Body Problem in Hypersonic Flow at Low Reynolds Number." CAL Report AF-1285-A-10, June 1963.

29. Chung, P. M. "Hypersonic Viscous Shock Layer of Nonequilibrium Dissociated Gas." NASA TR R-109, May 1961.

30. Inger, G. I. "Nonequilibrium Hypersonic Stagnation Flow at Low Reynolds Numbers." Aerospace Report SSD-TDR-64-118, September 1964.

31. Howe, J. T. and Viegas, J. R. "Solutions of the Ionizing Radiating Shock Layer, Including Reabsorption and Foreign Species Effects, and Stagnation Region Heat Transfer." NASA TR R-159, May 1963.

32. Lee, R. H. C. and Zierten, T. A. "Merged Layer Ionization in the Stagnation Region of a Blunt Body." Aerospace Report TR-1001 (S2240-10)-1, June 1967.

33. Howe, J. T. and Sheaffer, Y. S. "Mass Addition in the Stagnation Region for Velocity up to 50,000 Feet per Second." NASA TR R-207, August 1964.

34. Goldberg, L. "The Structure of the Viscous Hypersonic Shock Layer." GE TIS R65SD50, December 1965.

35. Goldberg, L. and Scala, S. M. "Mass Transfer in the Low Reynolds Number Viscous Layer around the Forward Region of a Hypersonic Vehicle." GE TIS R65SD27, July 1965.

36. Chen, S. Y., Aroesty, J. and Mobley, R. "The Hypersonic Viscous Shock Layer with Mass Transfer." Rand Momorandum RM-4631-PR, May 1966.

37. Anfimov, N. A. "Heat and Mass Transfer near the Stagnation Point with Injection and Suction of Various Gases through the Body Surface." Mekhanika Zhidkosti I Gaza, January-February 1966, pp. 14-20.

38. Dommett, R. L. "Thermodynamic Properties of Air at High Temperatures." RAE TN GW429, 1956.

39. Peng, T. C. and Pindroh, A. L. "An Improved Calculation of Gas Properties at High Temperatures: Air." Boeing Company Document No. D2-11722, February 1962.

40. Amdur, I. and Mason, E. A. "Properties of Gases at Very High Temperatures." Physics of Fluids, Vol. 1, No. 5, 1958, pp. 370-383.

41. Hirschfelder, J. O., Curtiss, C. F., and Bird, R. Molecular Theory of Gases and Liquids. John Wiley and Sons, New York, 1964.

APPENDIXES

I. ILLUSTRATIONS
II. TABLES
III. FLUID PROPERTIES USED IN THE BINARY GAS BOUNDARY-LAYER PROGRAM
IV. SURFACE HEAT-TRANSFER RELATIONS

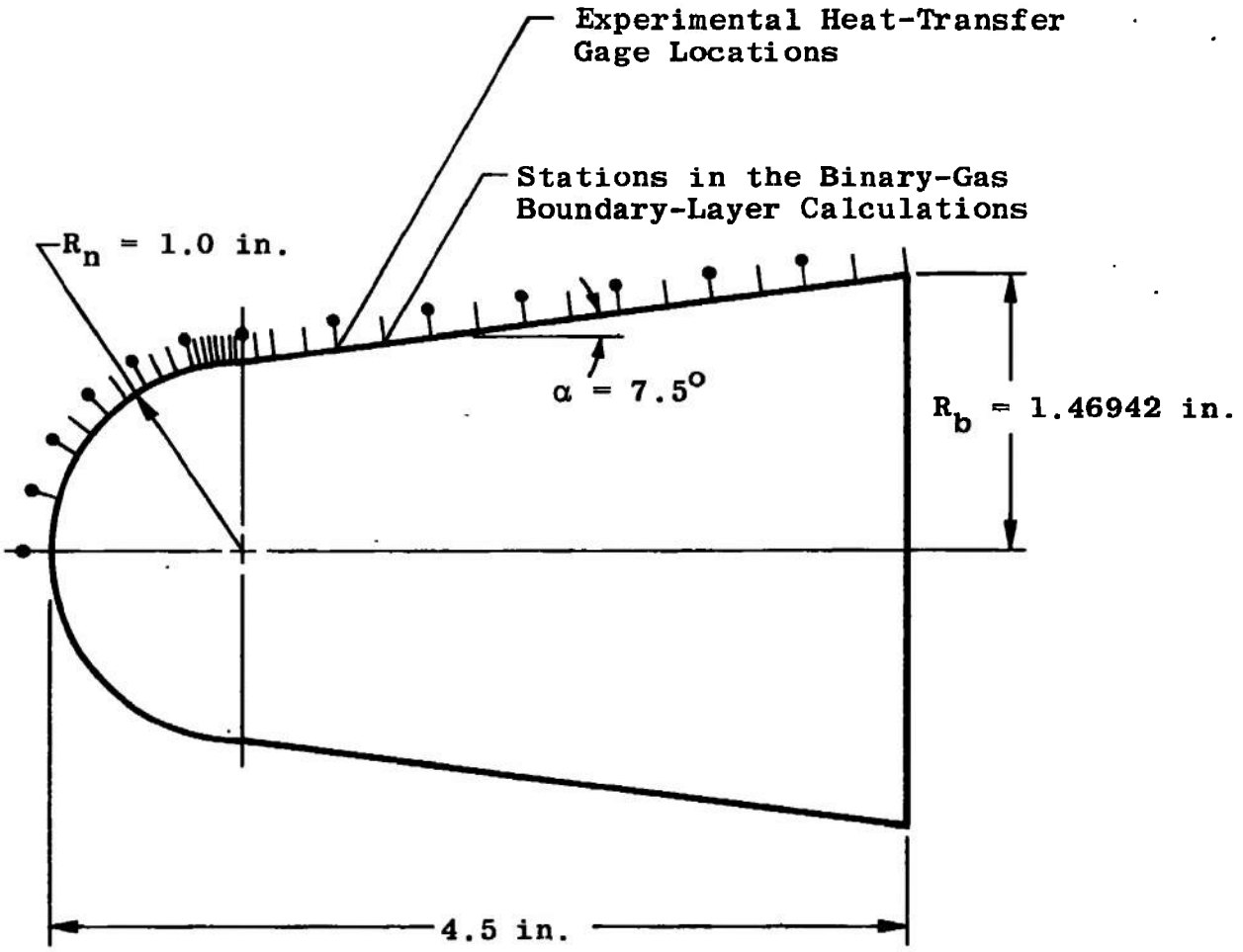

Fig. 1 Cone Geometry

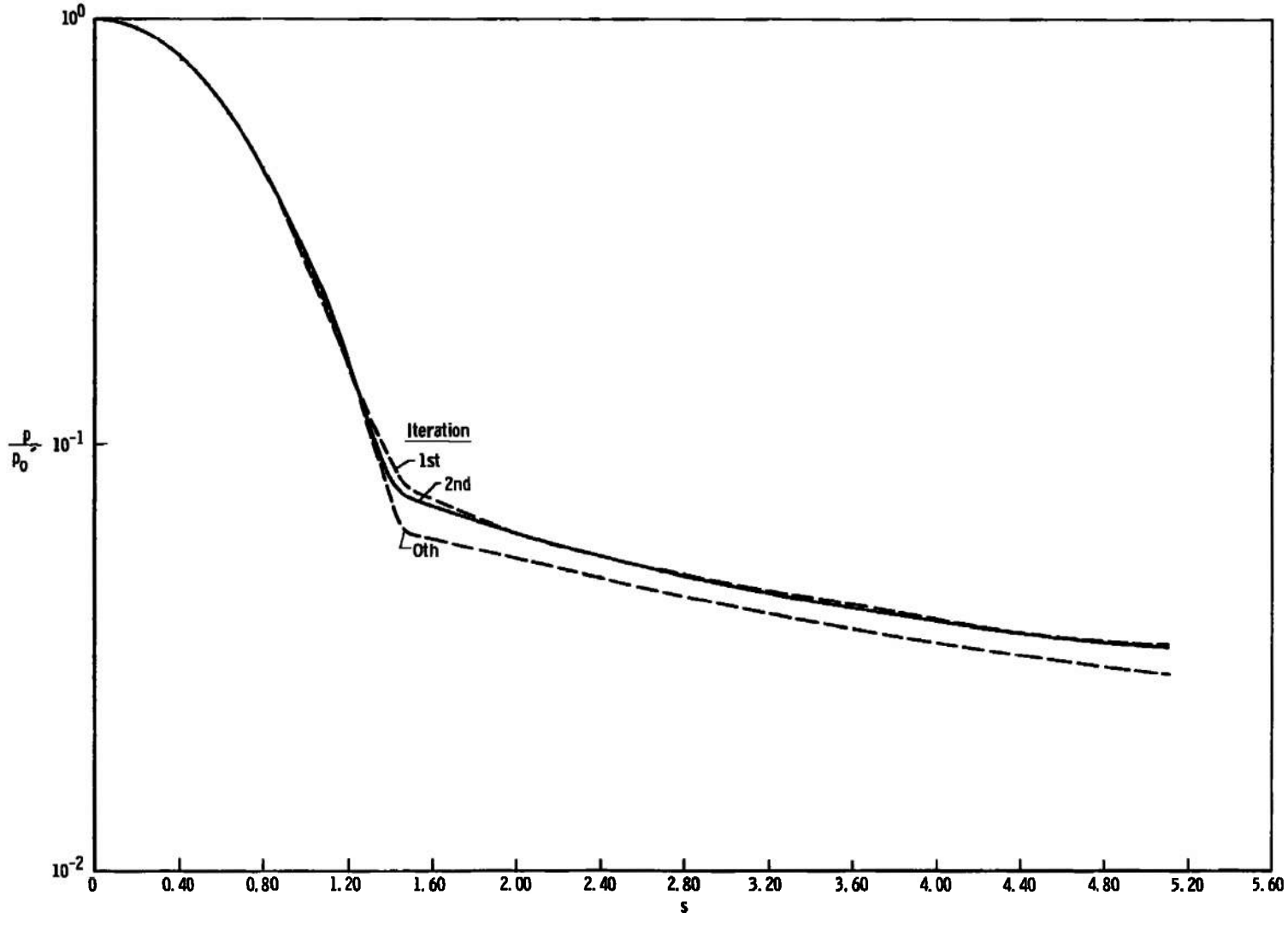

Fig. 2 Pressure Distribution over the Cone without Mass Transfer

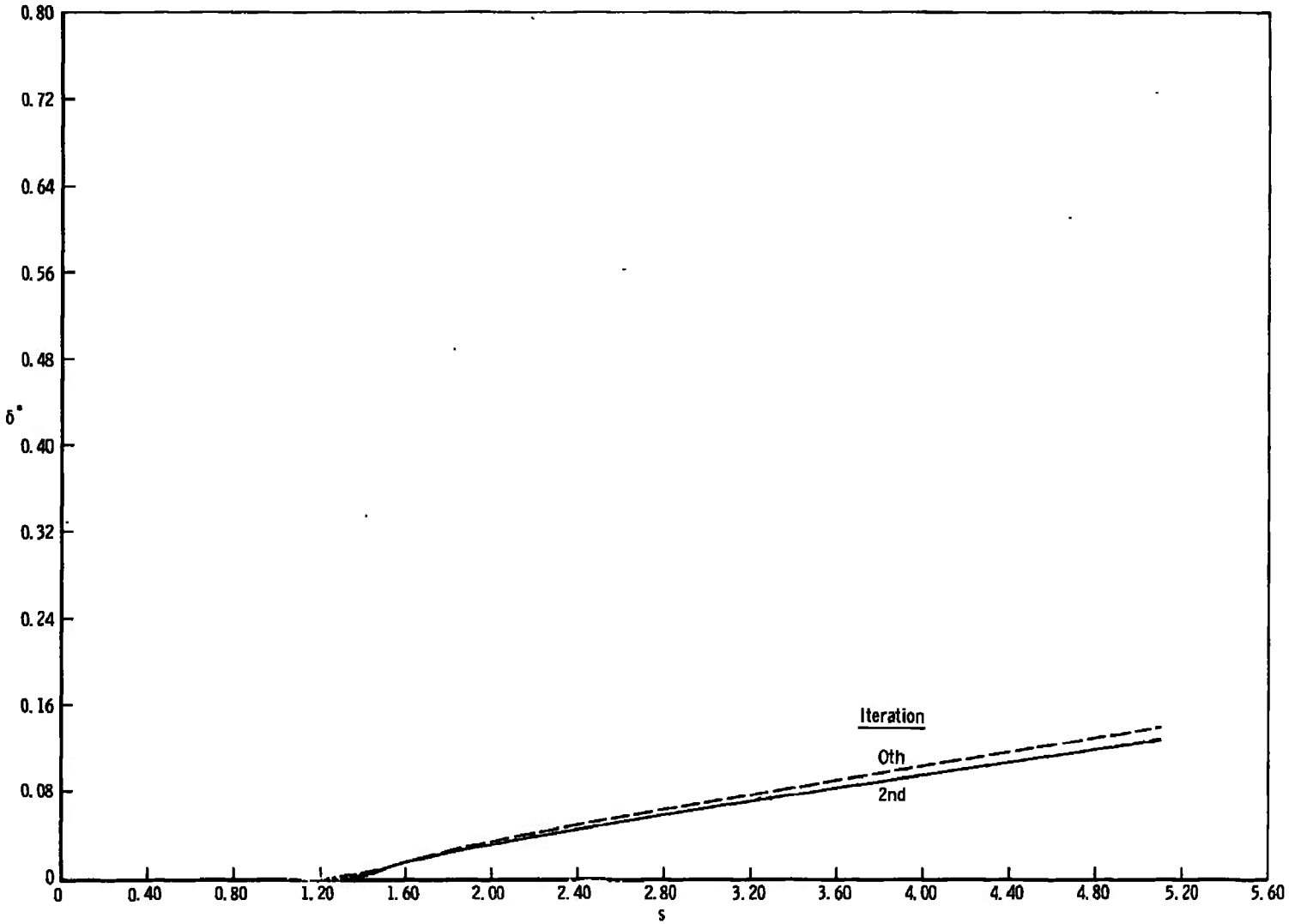

Fig. 3 Displacement Thickness over the Cone without Mass Transfer

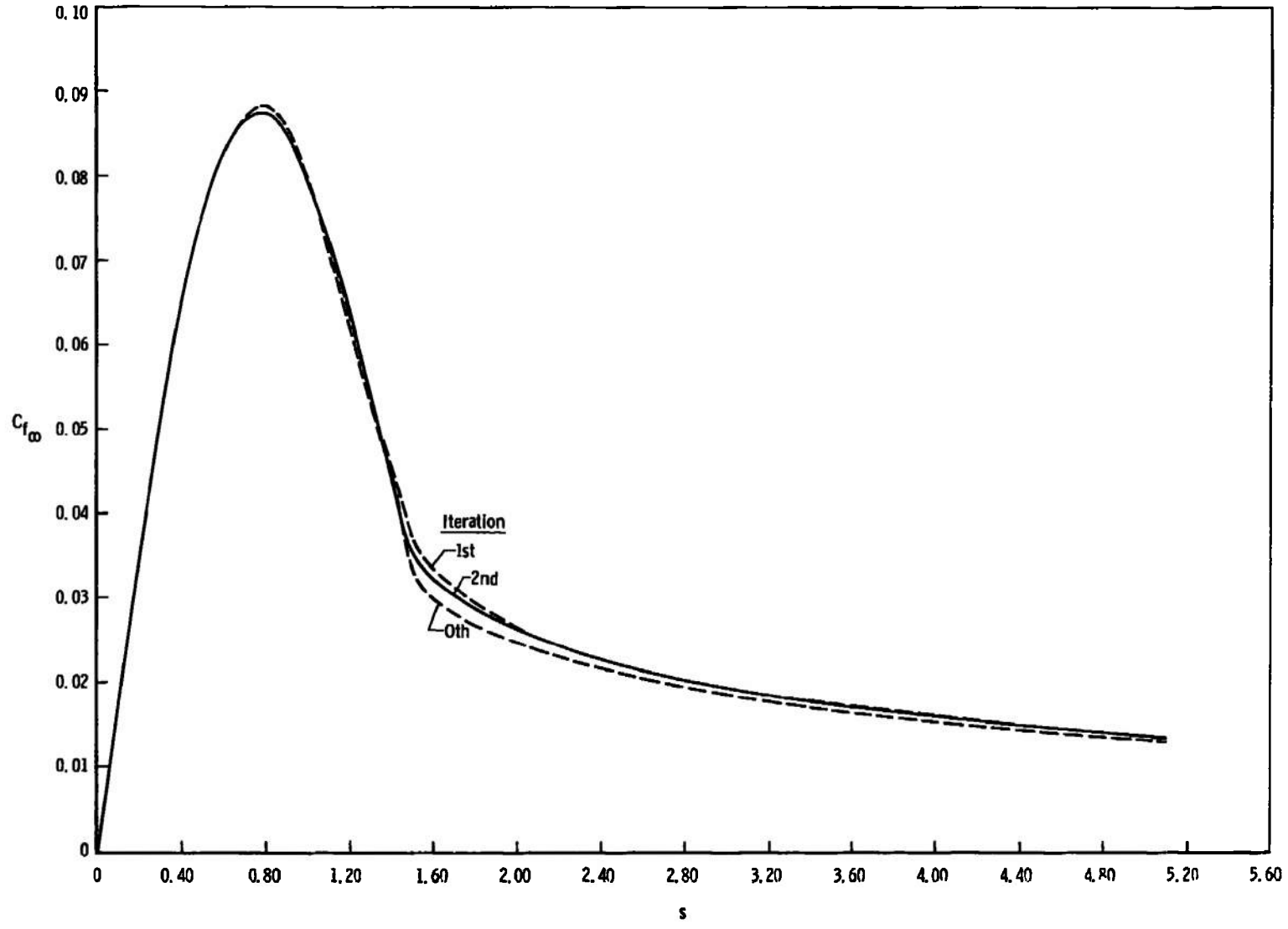

Fig. 4 Skin-Friction Coefficient over the Cone without Mass Transfer

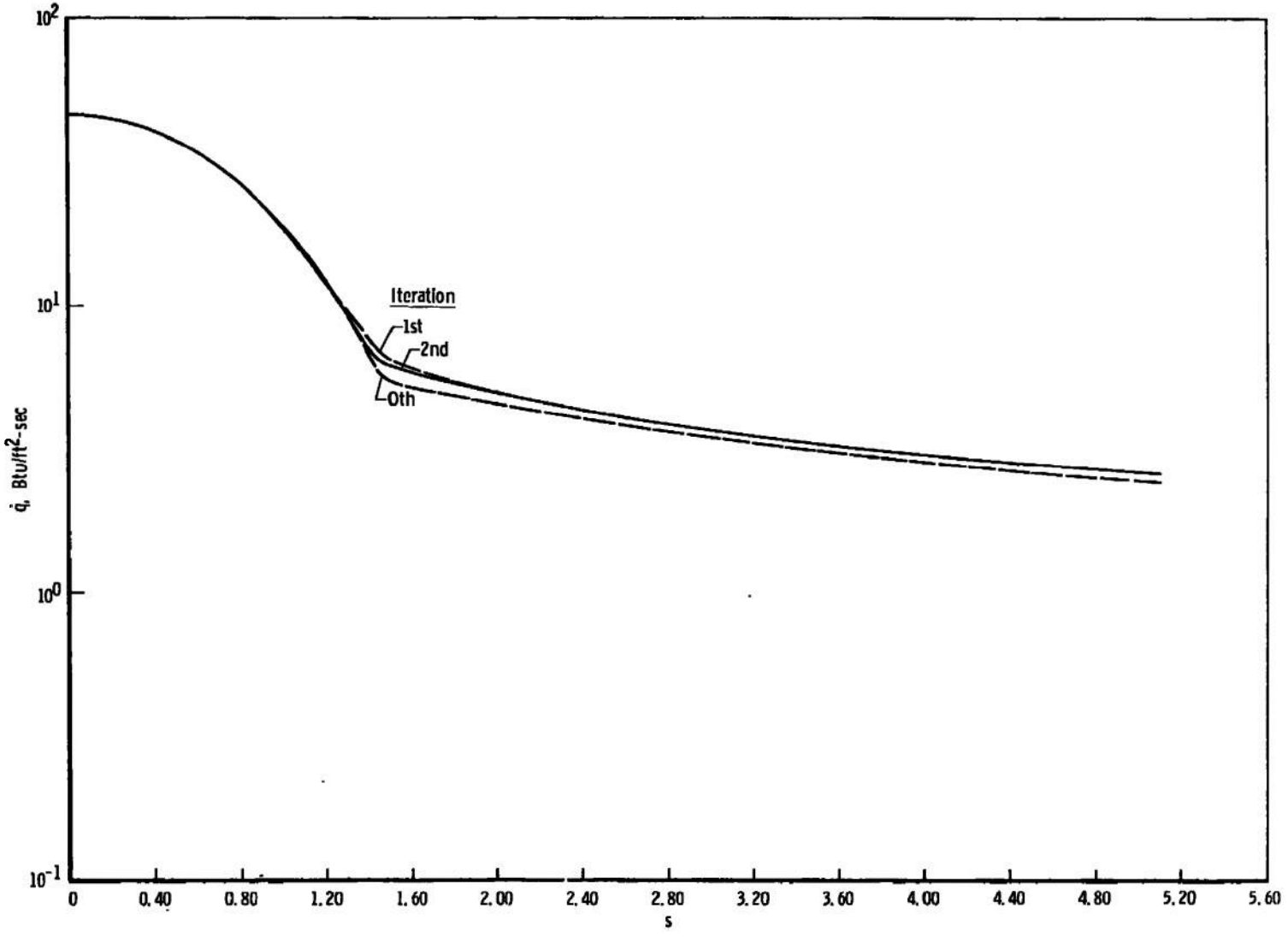

Fig. 5 Dimensional Heat-Transfer Rate over the Cone without Mass Transfer

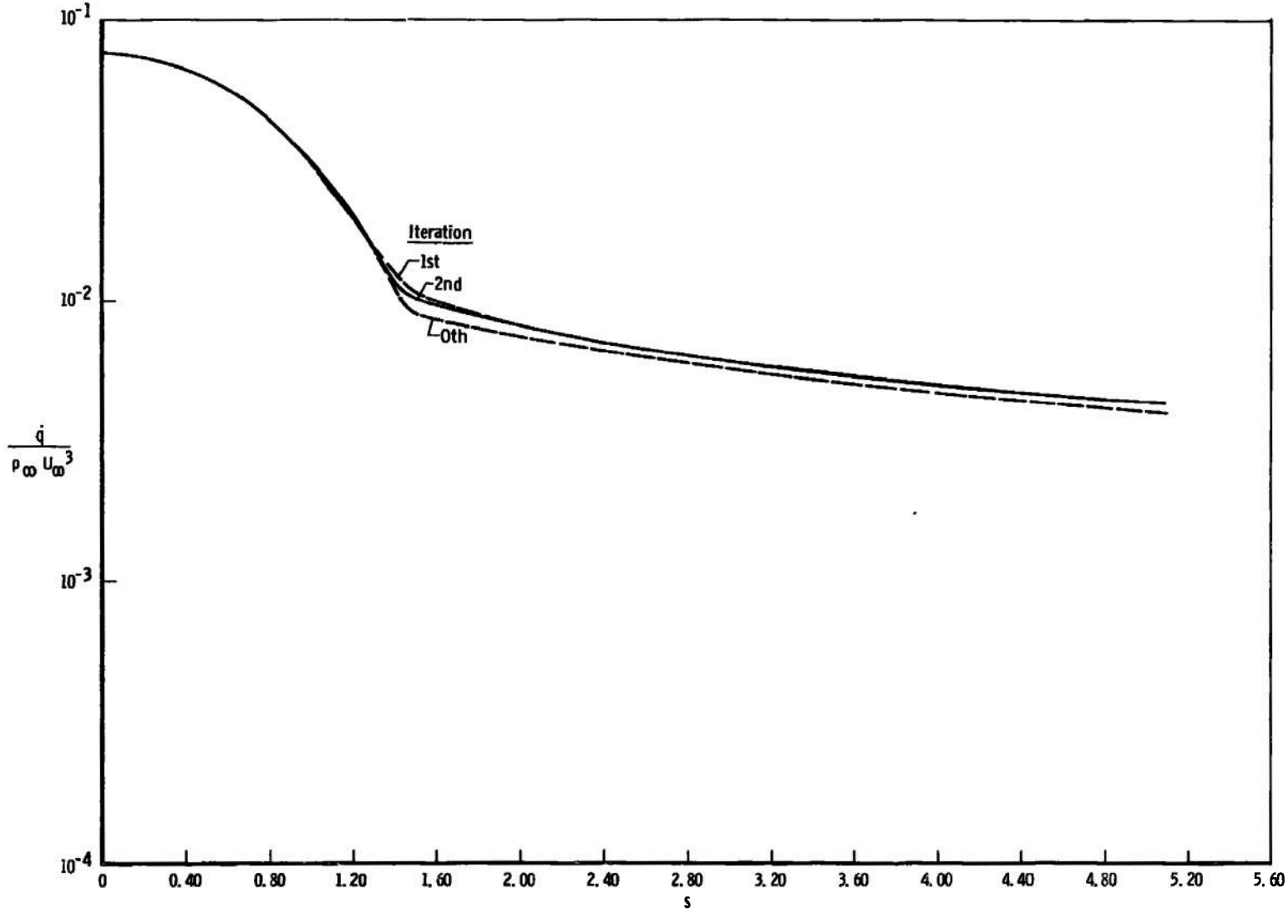

Fig. 6 Dimensionless Heat-Transfer Rate $\dot{q}/\rho_\infty U_\infty^3$ over the Cone without Mass Transfer

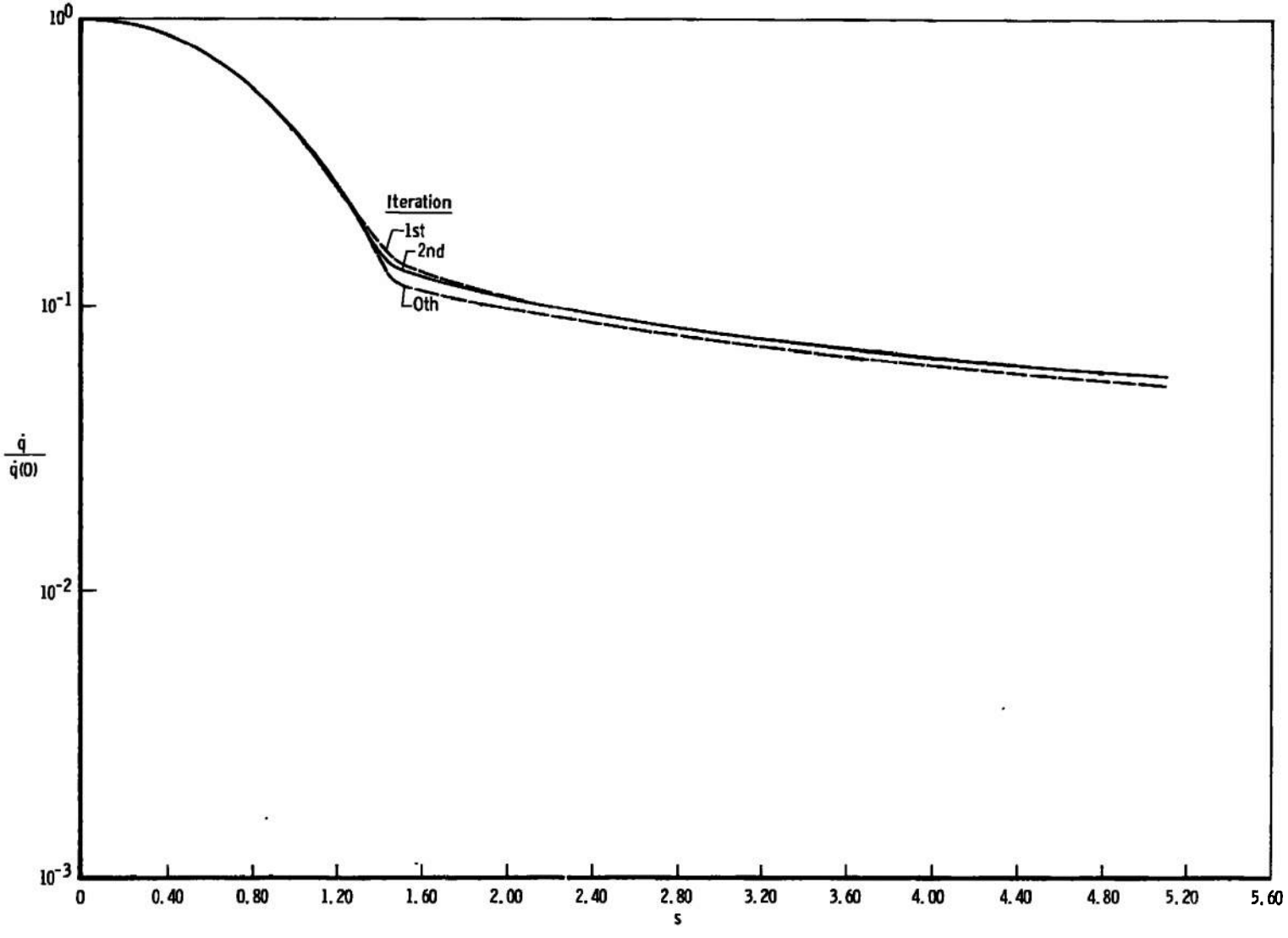

Fig. 7 Dimensionless Heat-Transfer Rate $\dot{q}/\dot{q}(0)$ over the Cone without Mass Transfer

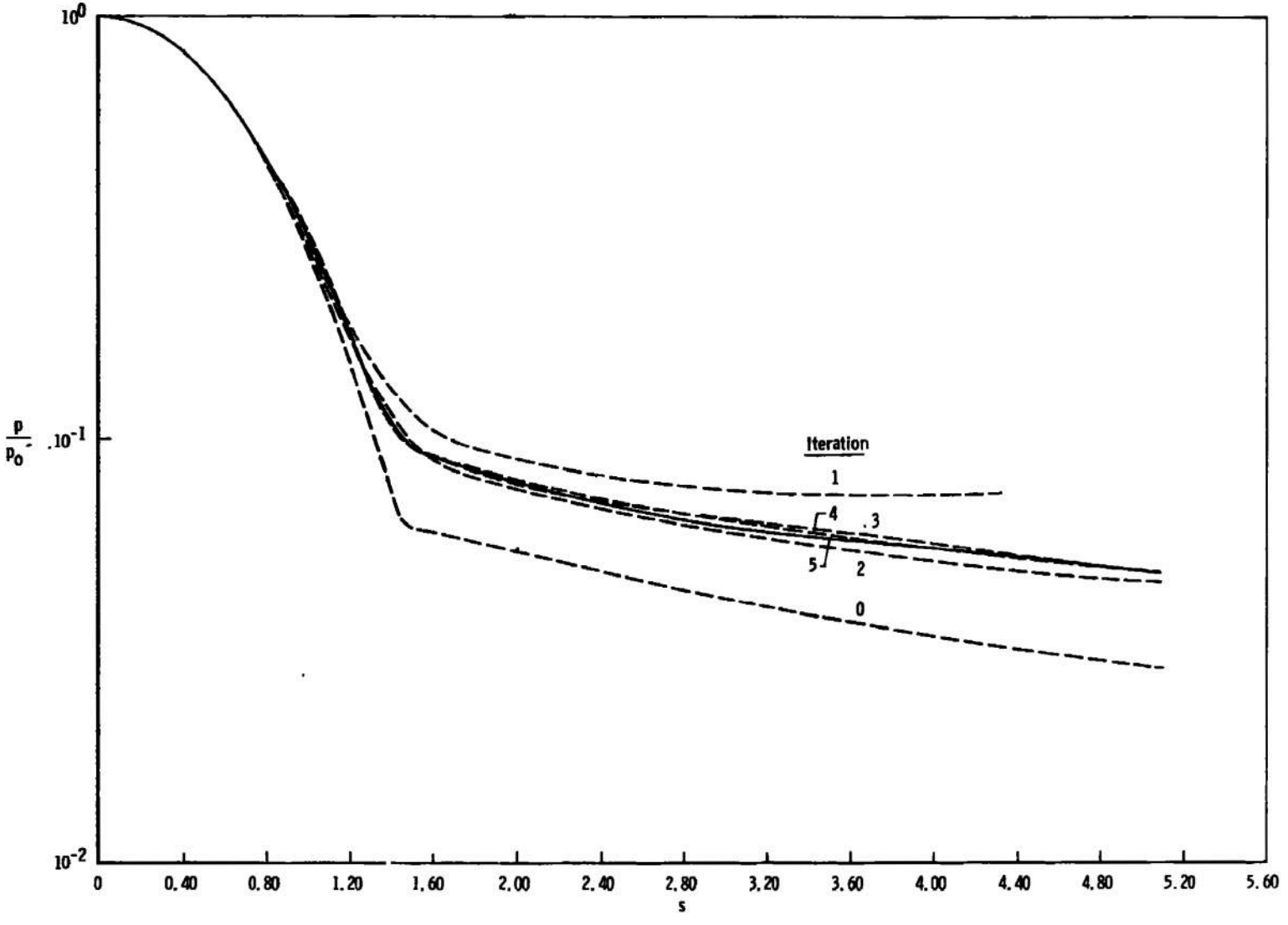

Fig. 8 Pressure Distribution over the Cone with Argon Injection

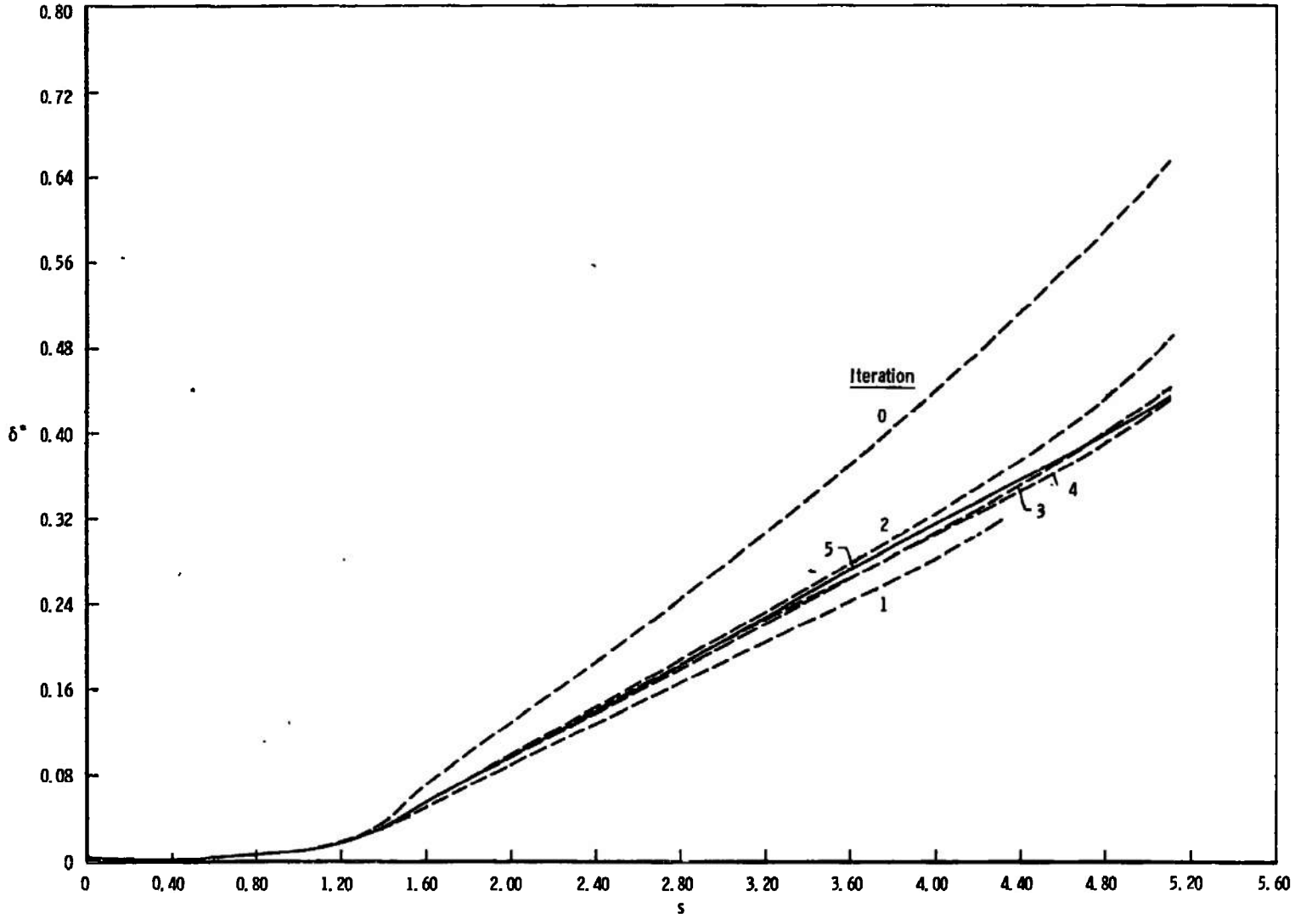

Fig. 9 Displacement Thickness over the Cone with Argon Injection

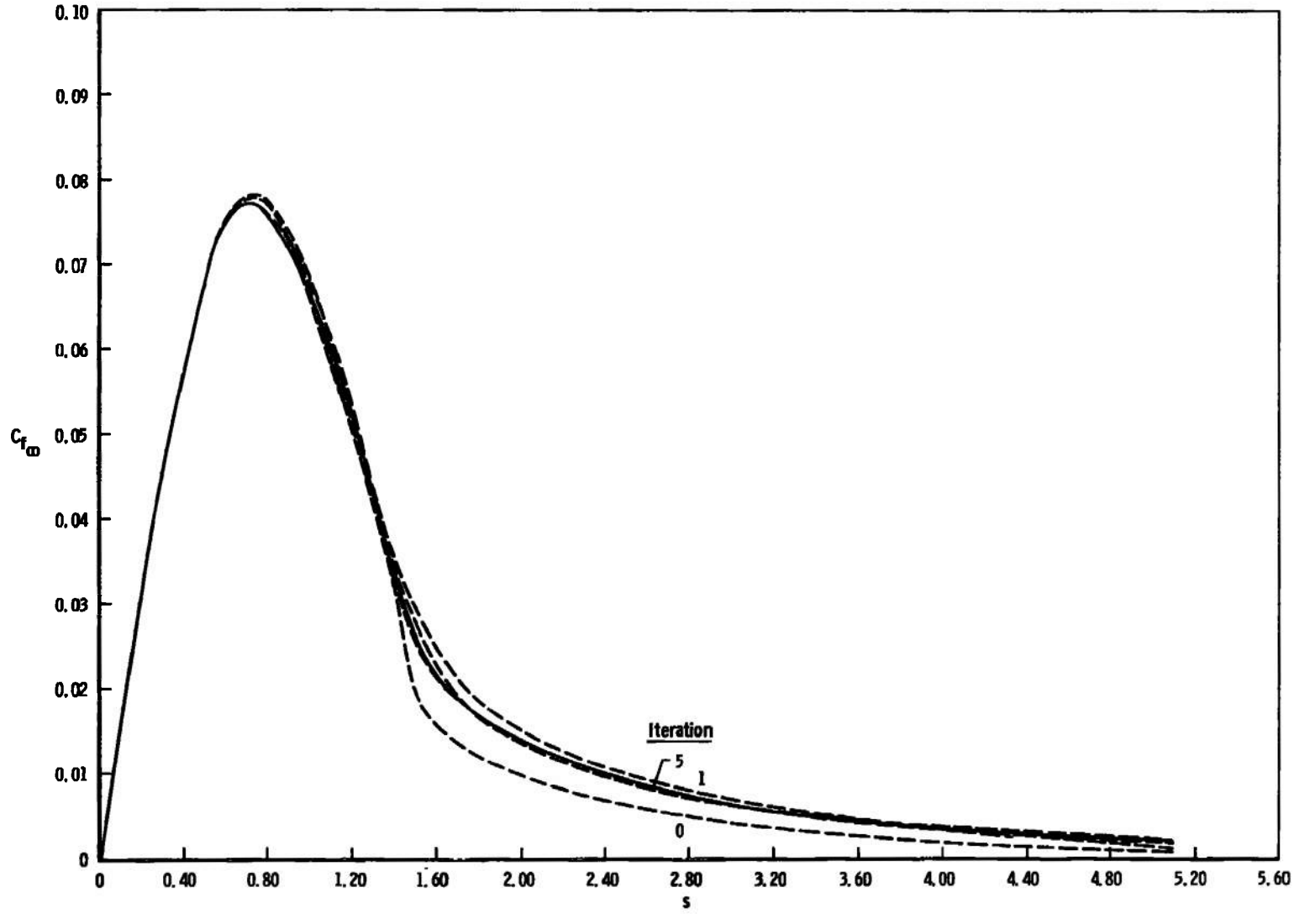

Fig. 10 Skin-Friction Coefficient over the Cone with Argon Injection

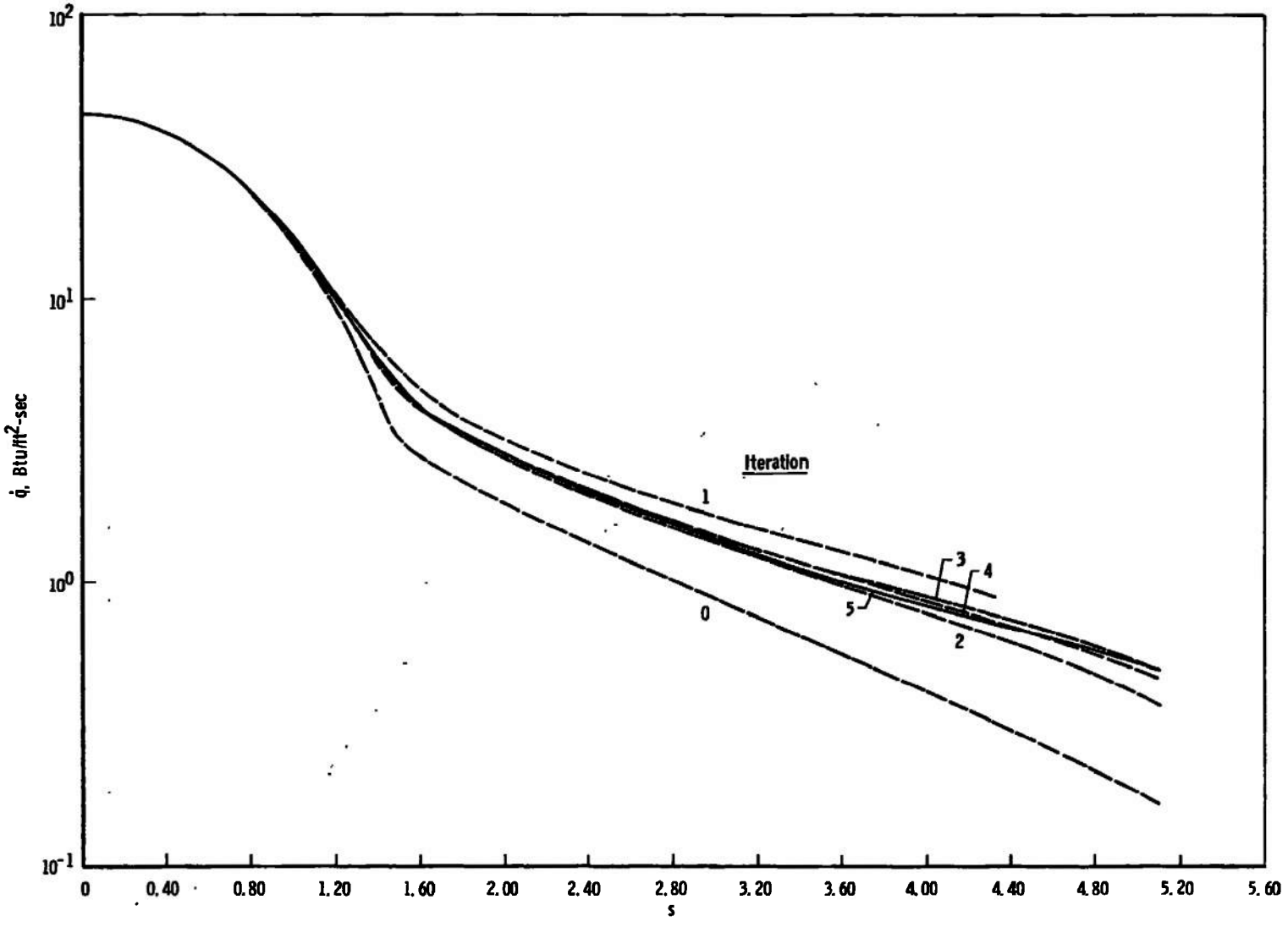

Fig. 11 Dimensional Heat-Transfer Rate to the Cone with Argon Injection

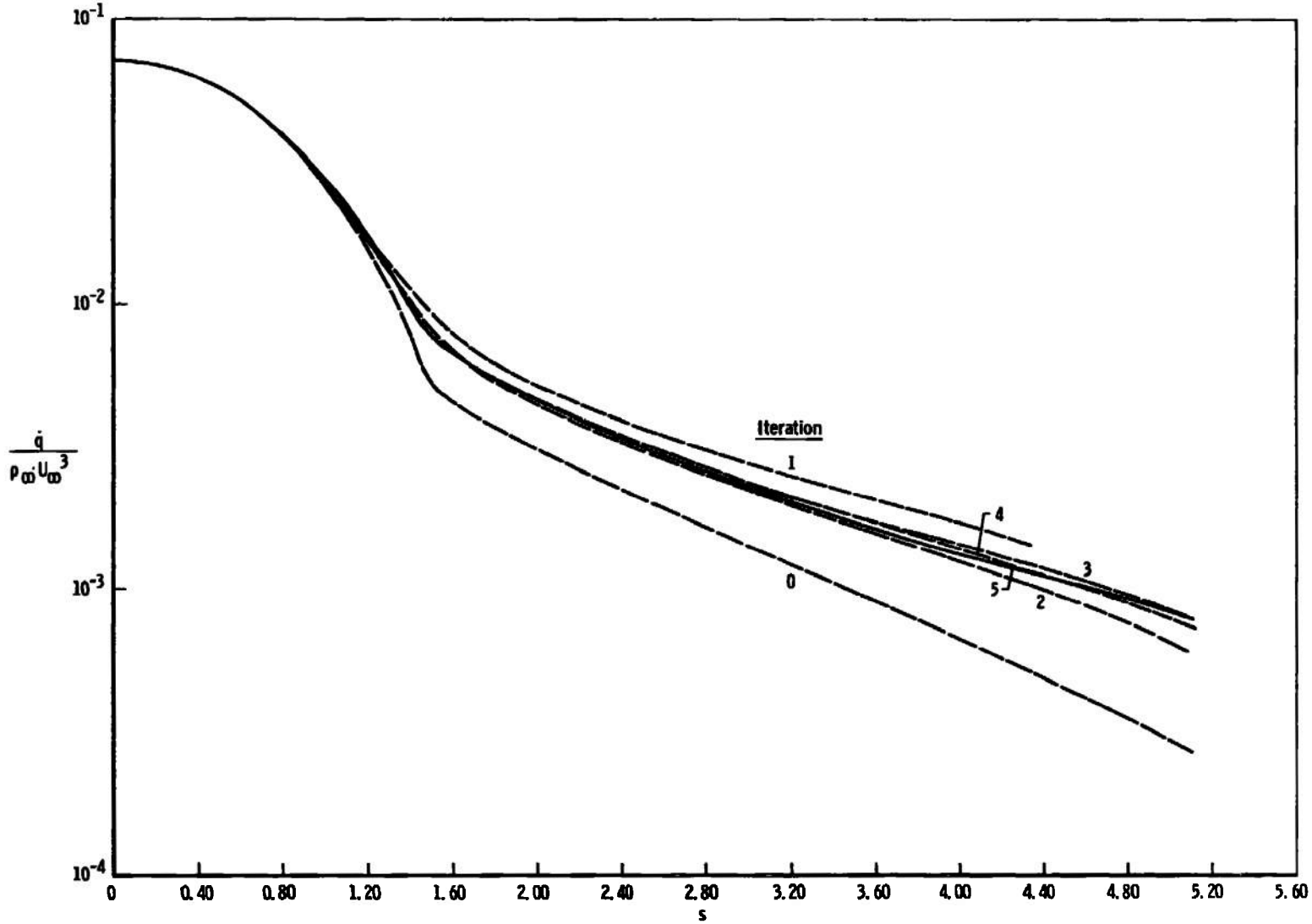

Fig. 12 Dimensionless Heat-Transfer Rate $\dot{q}/\rho_\infty U_\infty^3$ to the Cone with Argon Injection

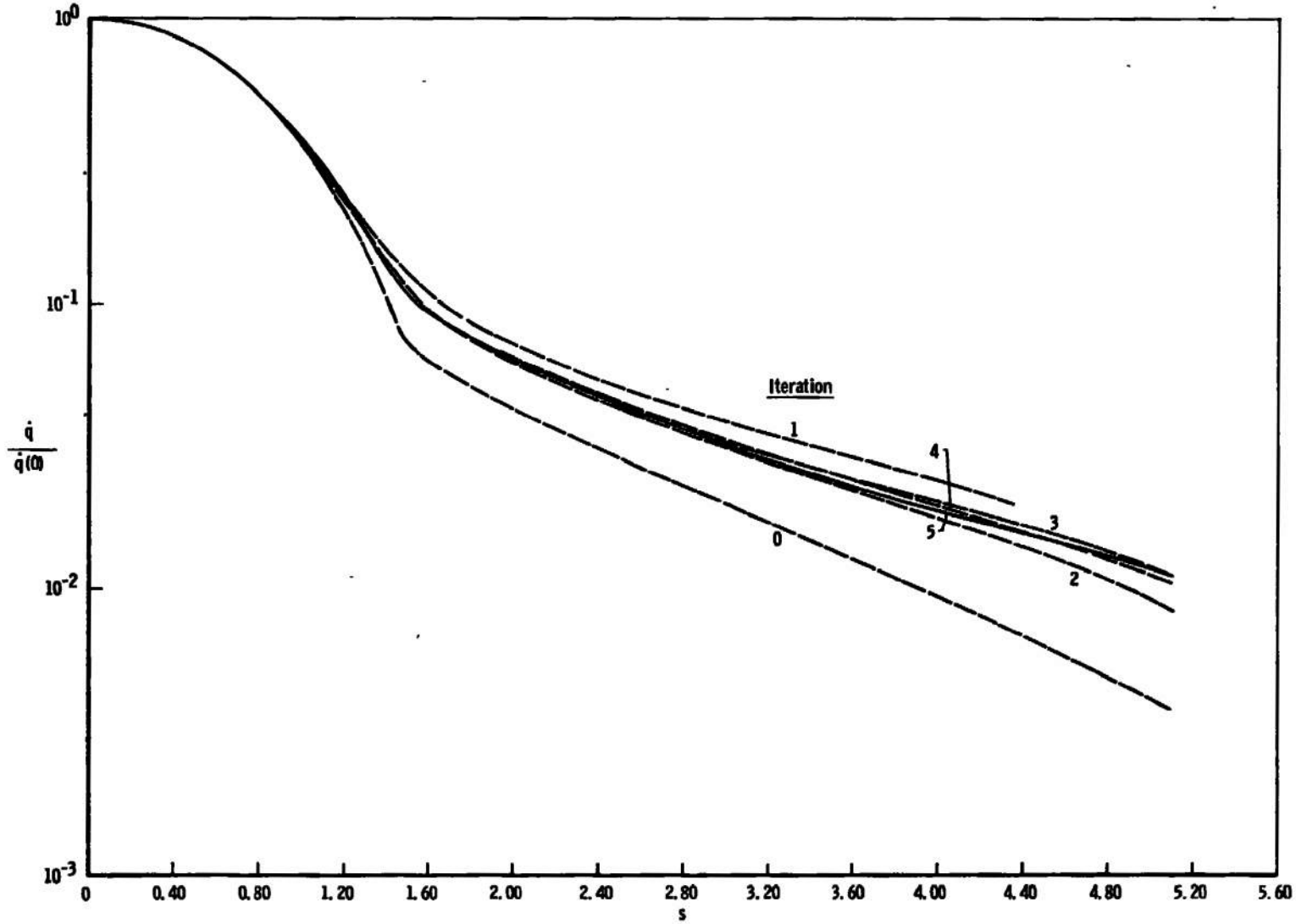

Fig. 13 Dimensionless Heat-Transfer Rate $\dot{q}/\dot{q}(0)$ to the Cone with Argon Injection

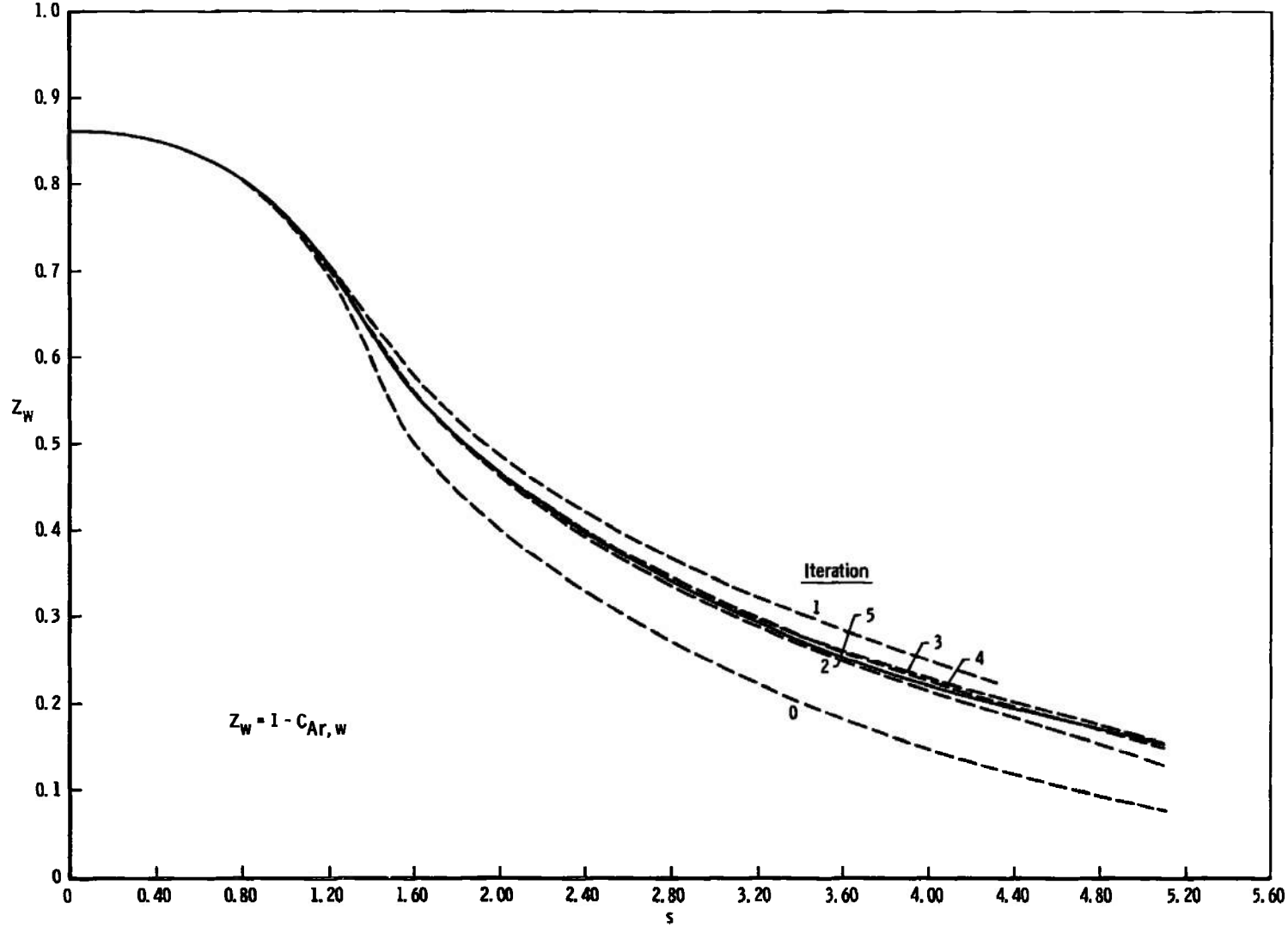

Fig. 14 Argon Mass Fraction Distribution over the Cone Surface

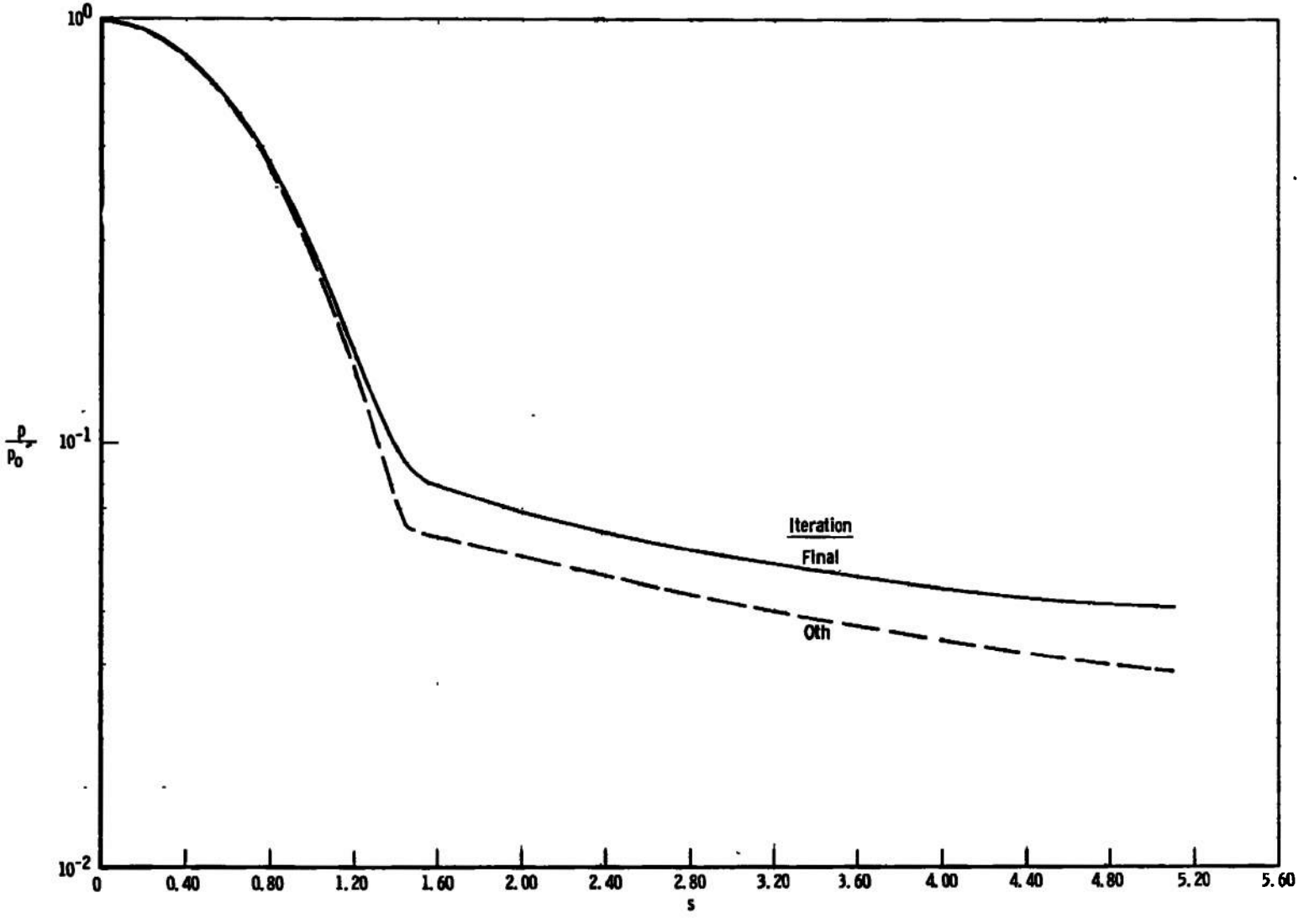

Fig. 15 Pressure Distribution over the Cone with Helium Injection

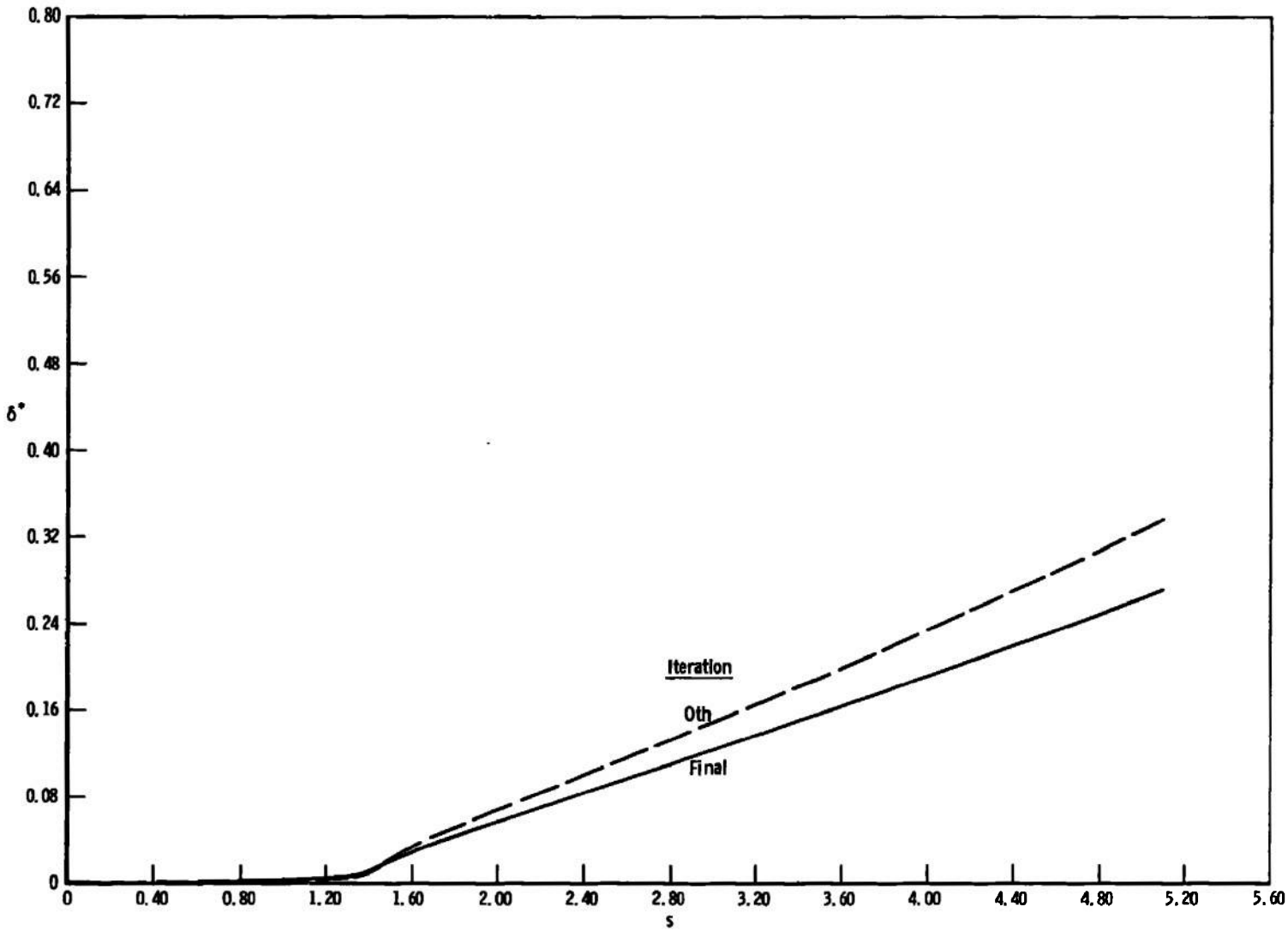

Fig. 16 Displacement Thickness over the Cone with Helium Injection

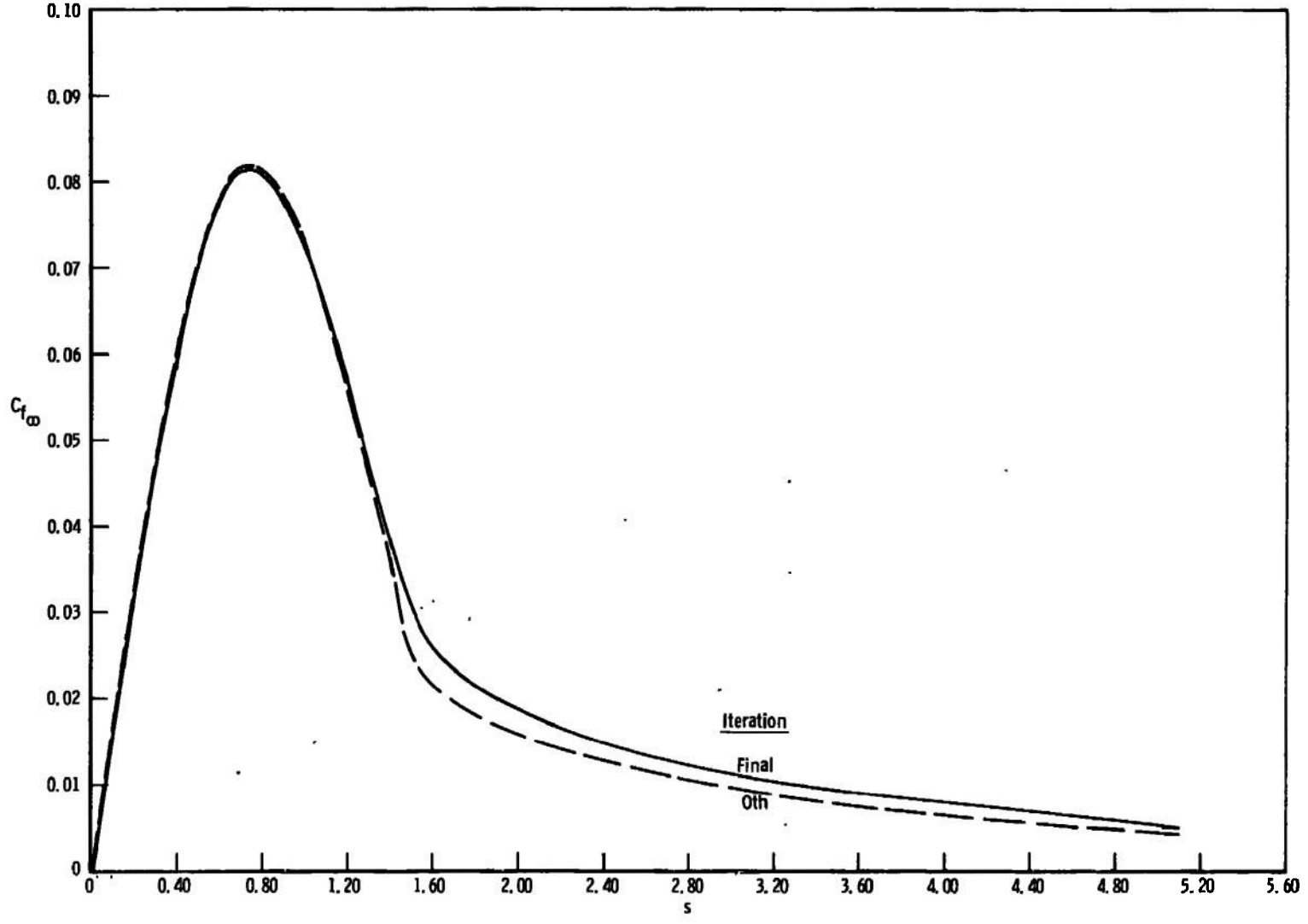

Fig. 17 Skin-Friction Distribution over the Cone with Helium Injection

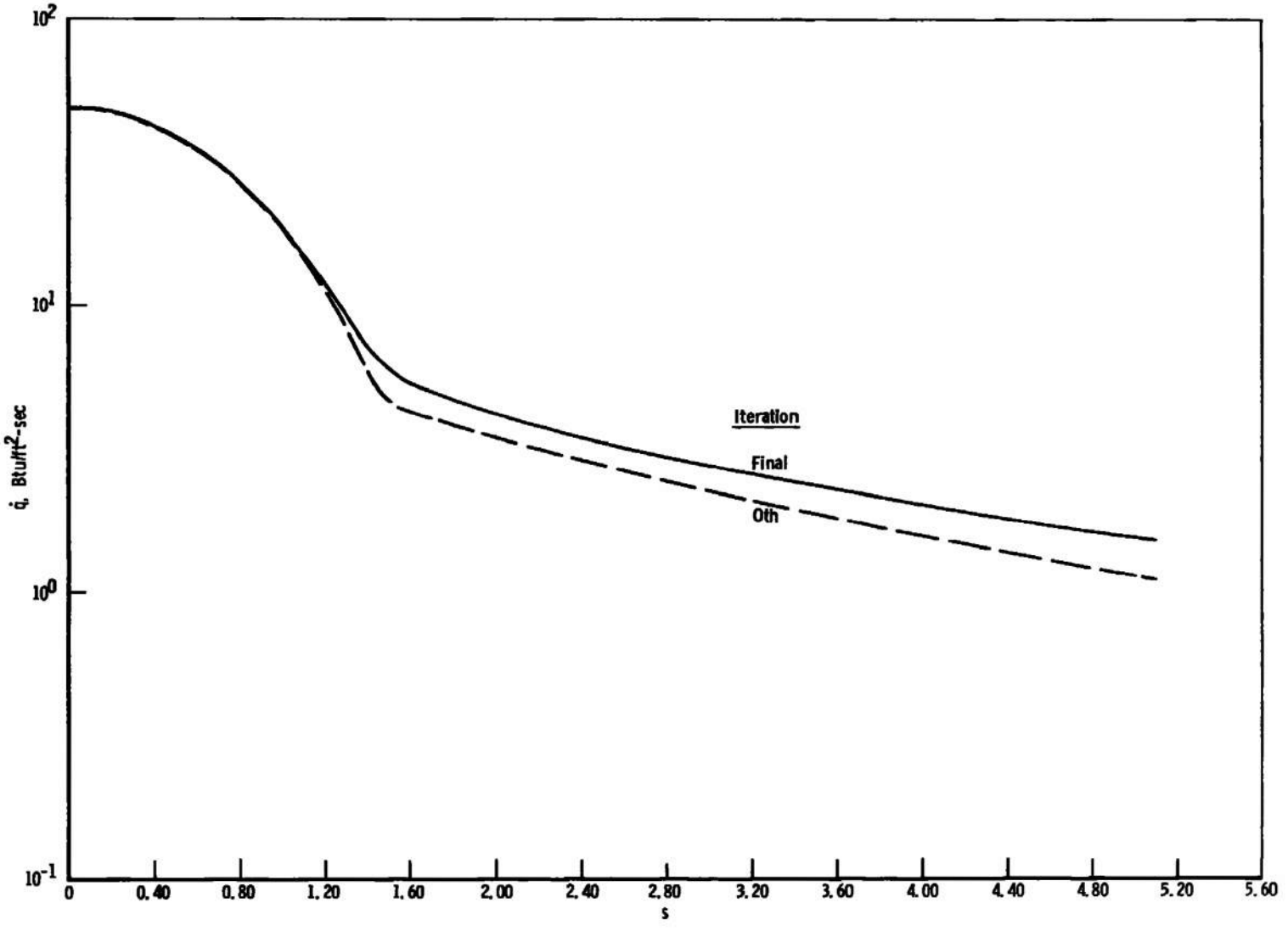

Fig. 18 Dimensional Heat-Transfer Rate to the Cone with Helium Injection

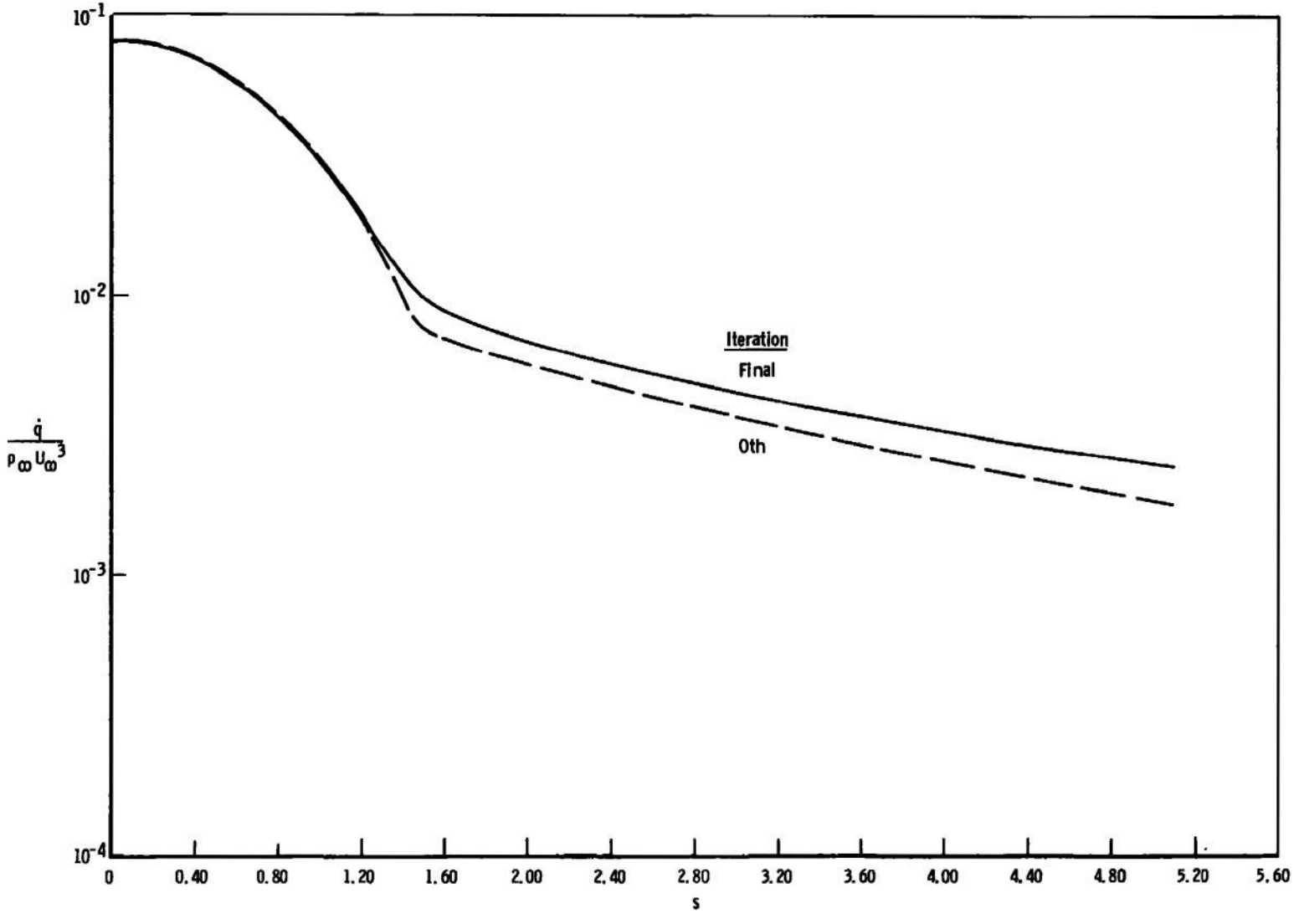

Fig. 19 Dimensionless Heat-Transfer Rate $\dot{q}/\rho_\infty U_\infty^3$ to the Cone with Helium Injection

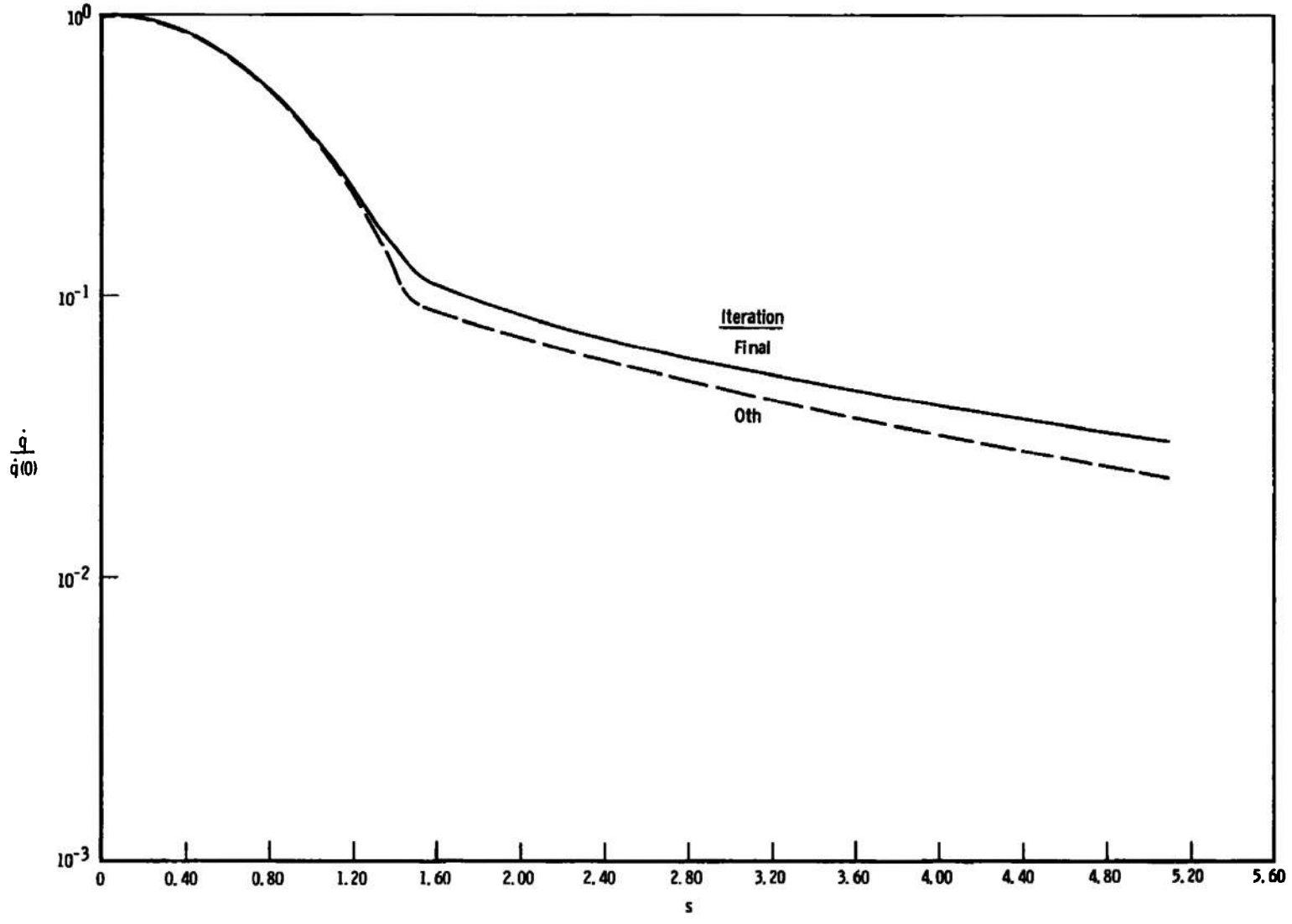

Fig. 20 Dimensionless Heat-Transfer rate $\dot{q}/\dot{q}(0)$ to the Cone with Helium Injection

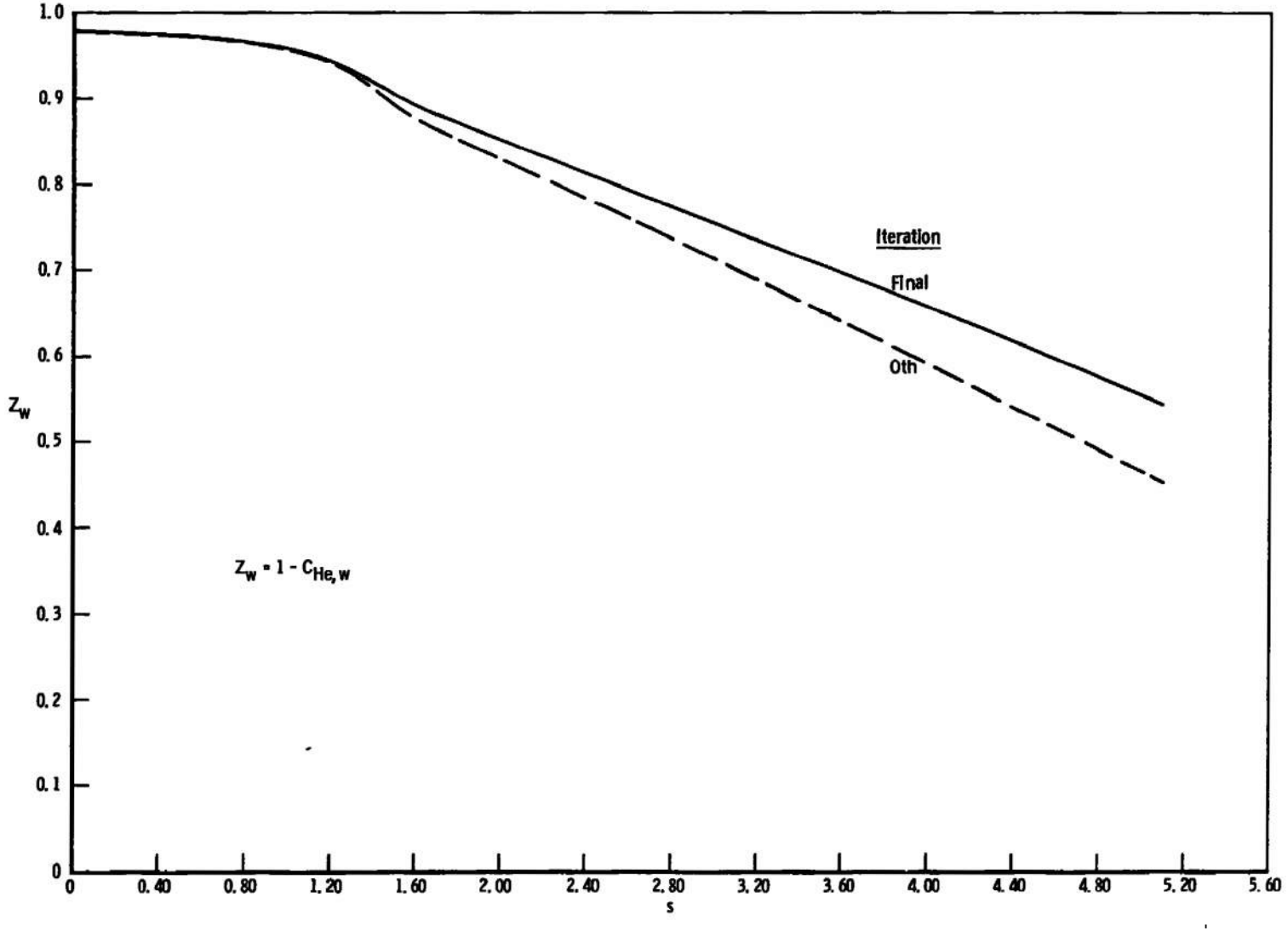

Fig. 21 Helium Mass Fraction Distribution over the Cone Surface

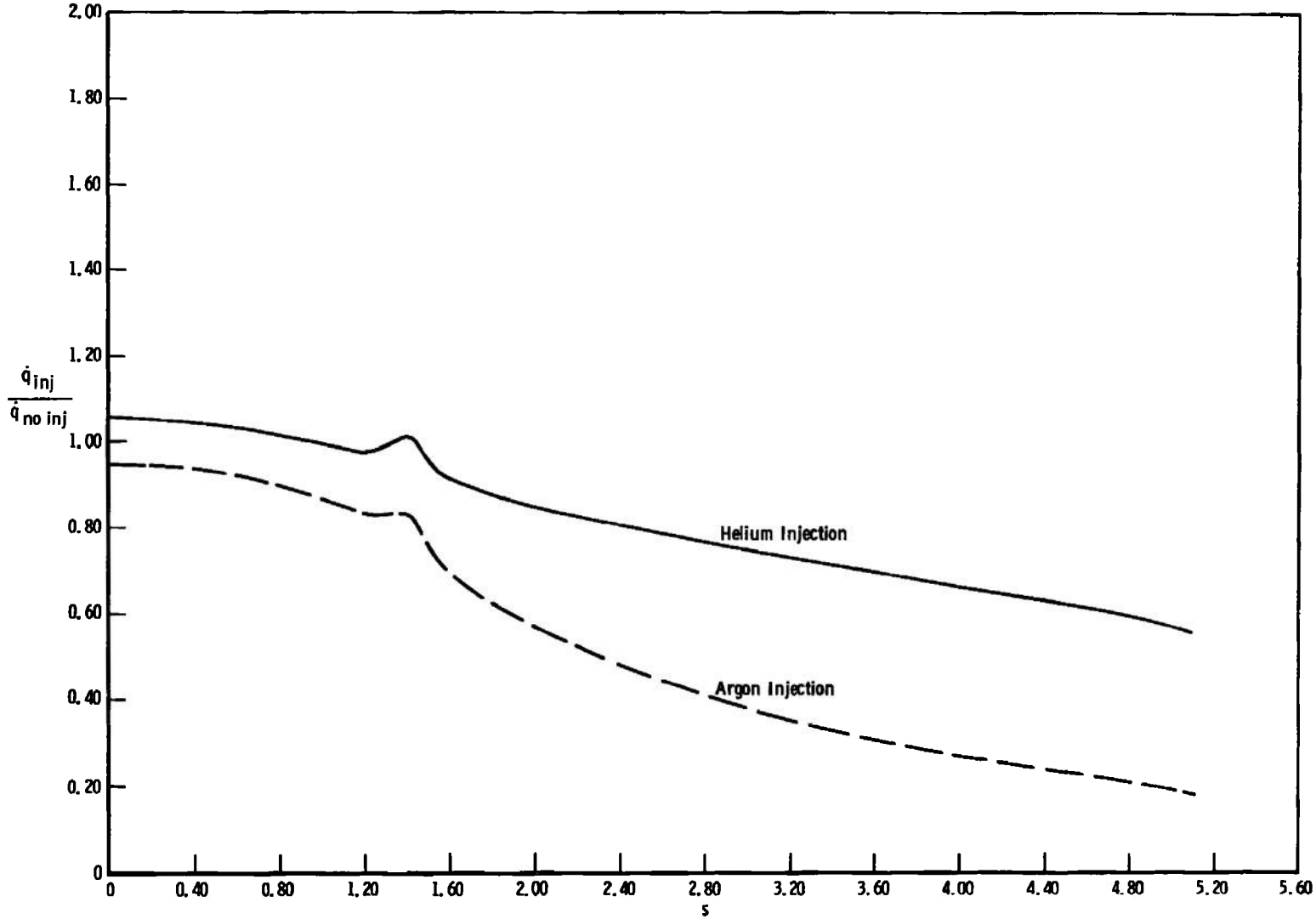

Fig. 22 Heat-Transfer with Injection to No-Injection Heat-Transfer Ratio Including the Effects of Displacement and Transverse Curvature

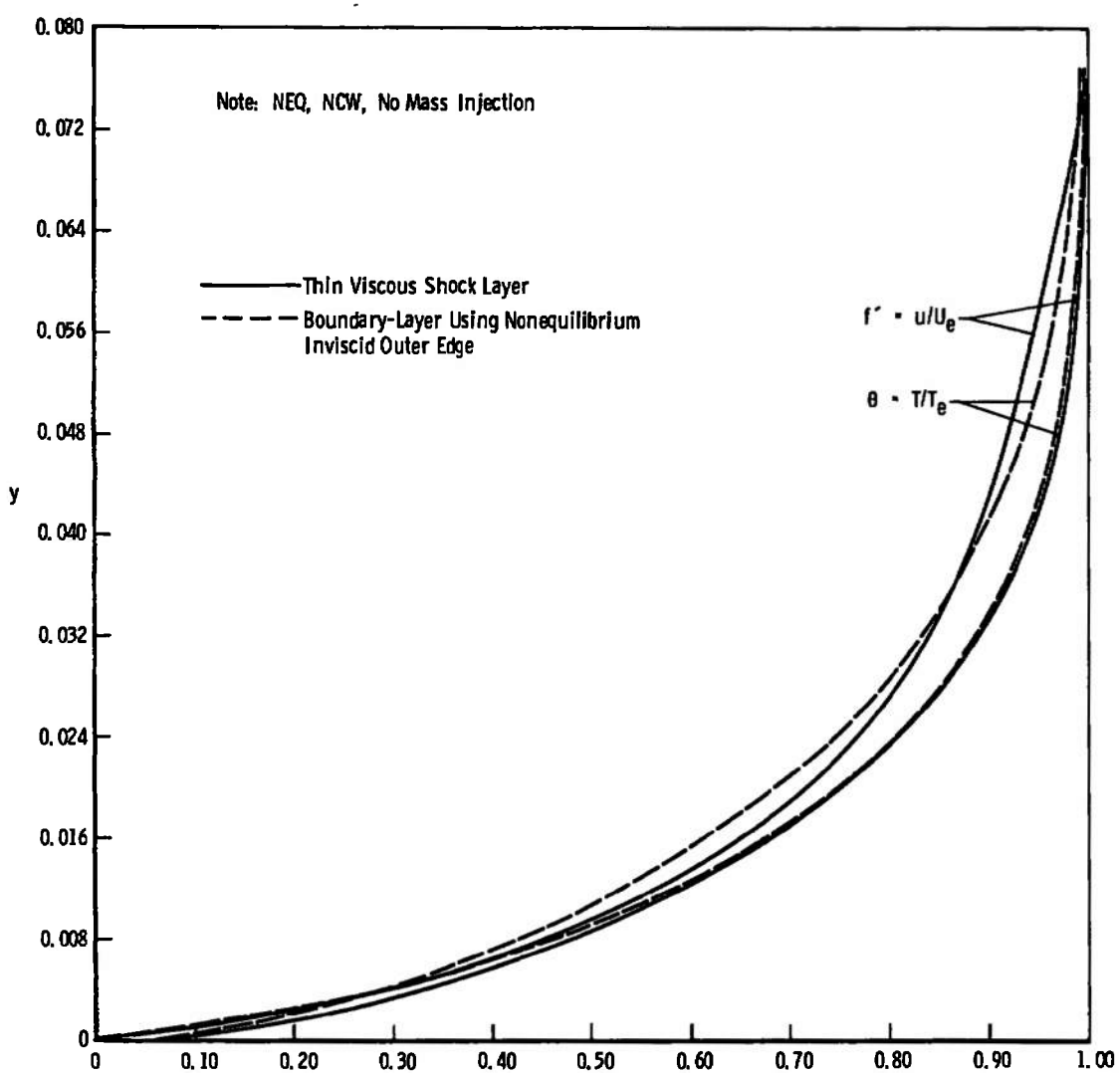

Fig. 23 Velocity and Temperature Profiles at the Stagnation Point under Nonequilibrium Conditions

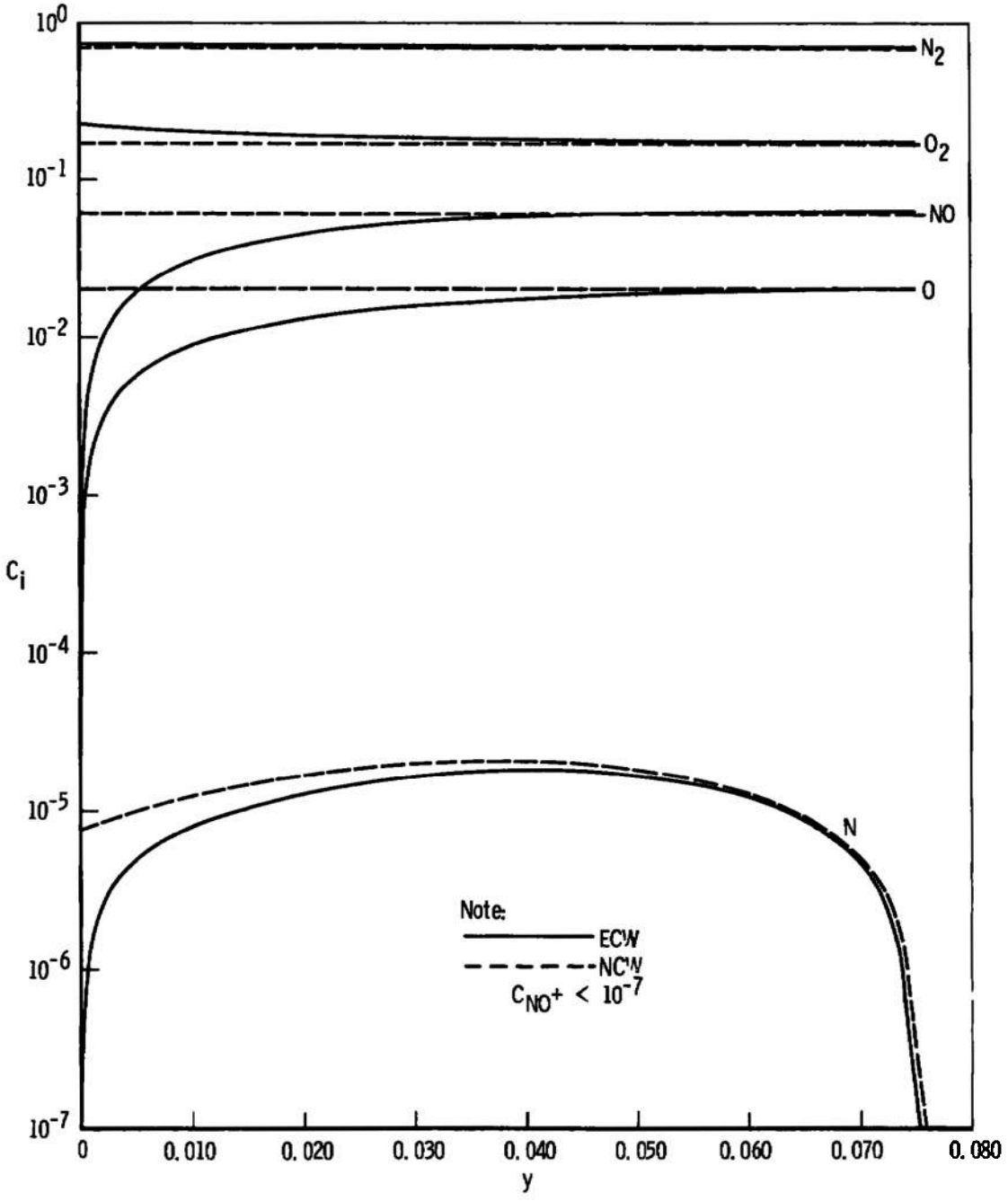

a. No Wall Mass Transfer

Fig. 24 Thin Viscous Shock Layer Specie Distributions

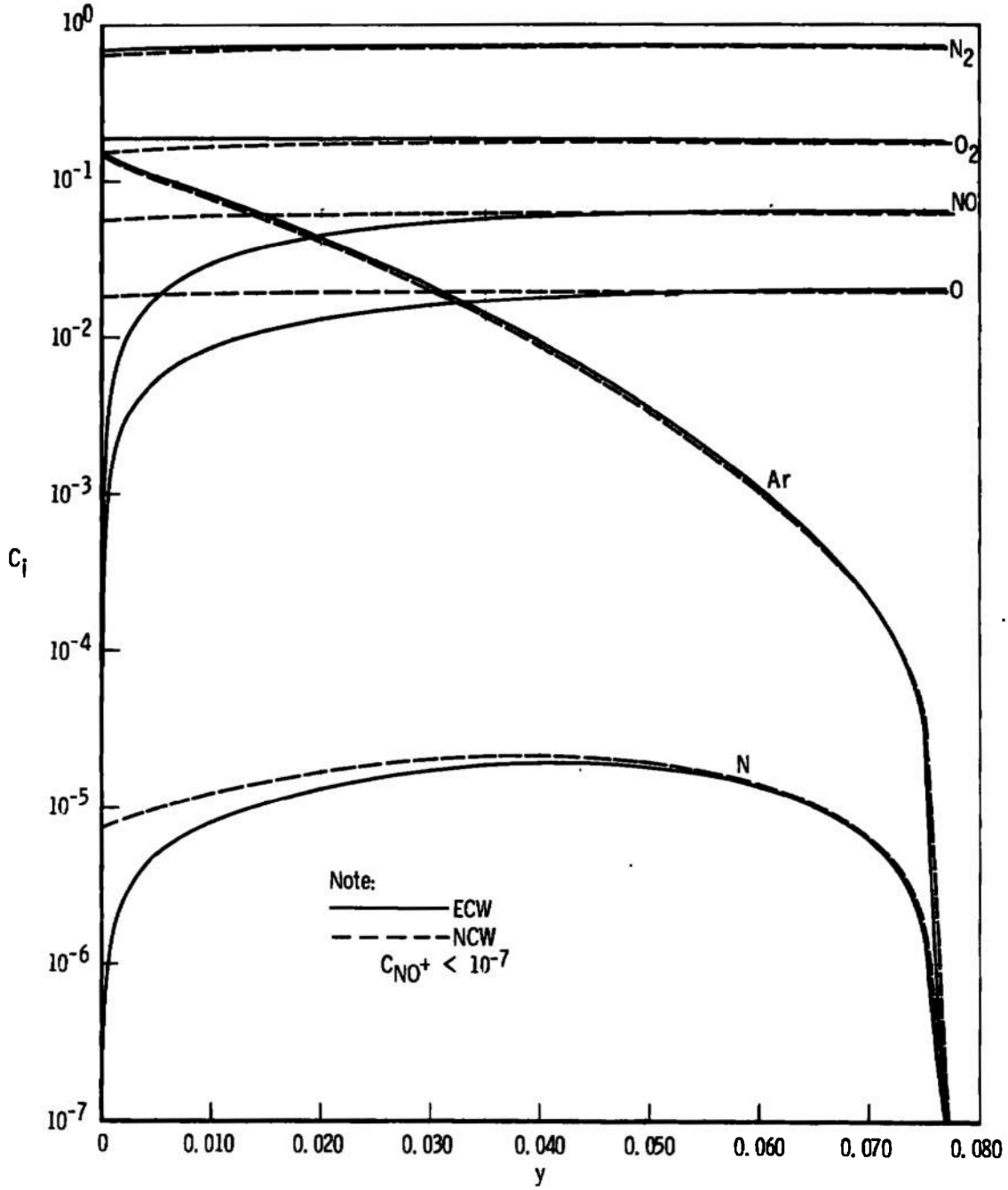

b. Argon Injection

Fig. 24 Continued

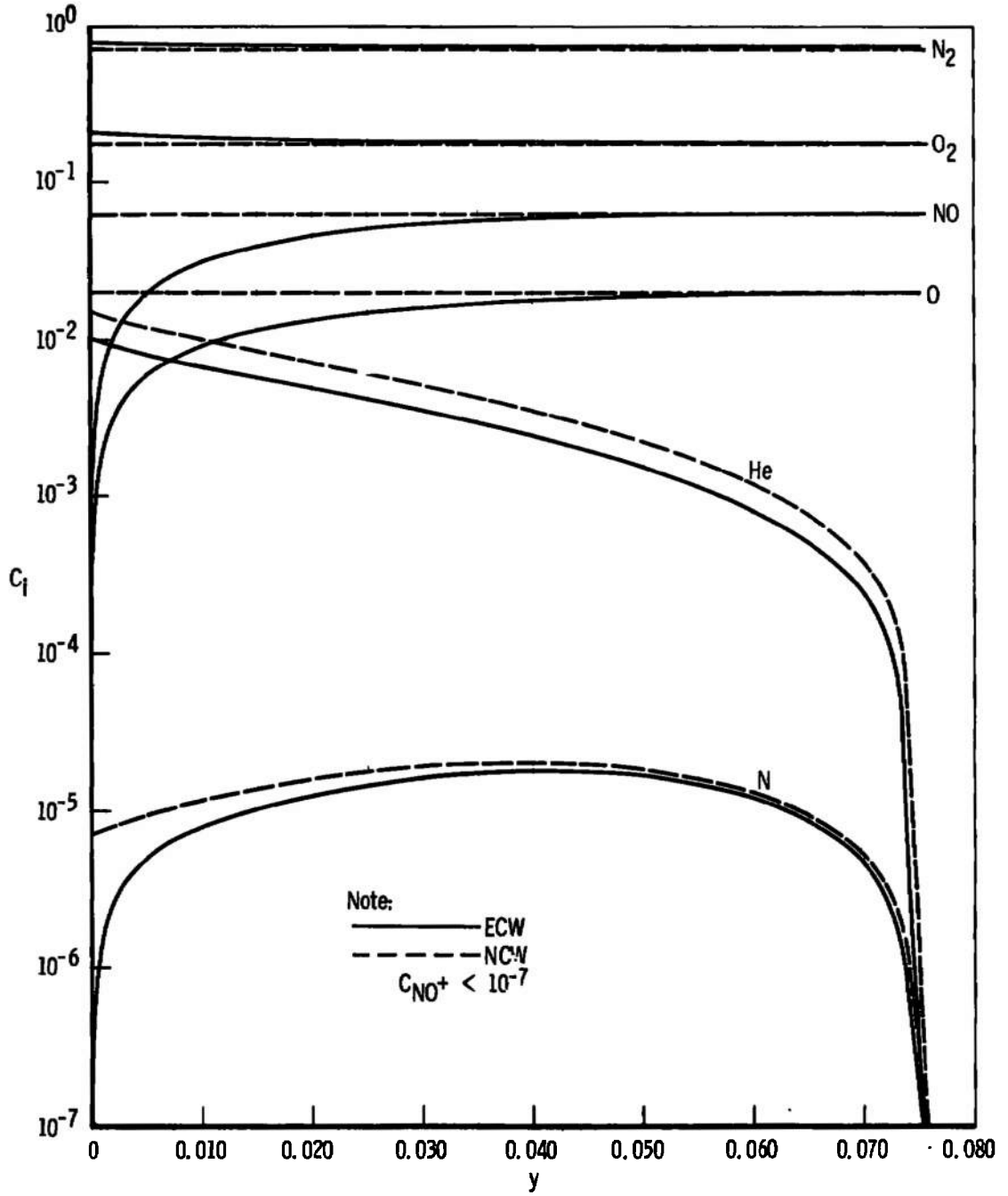

c. Helium Injection

Fig. 24 Concluded

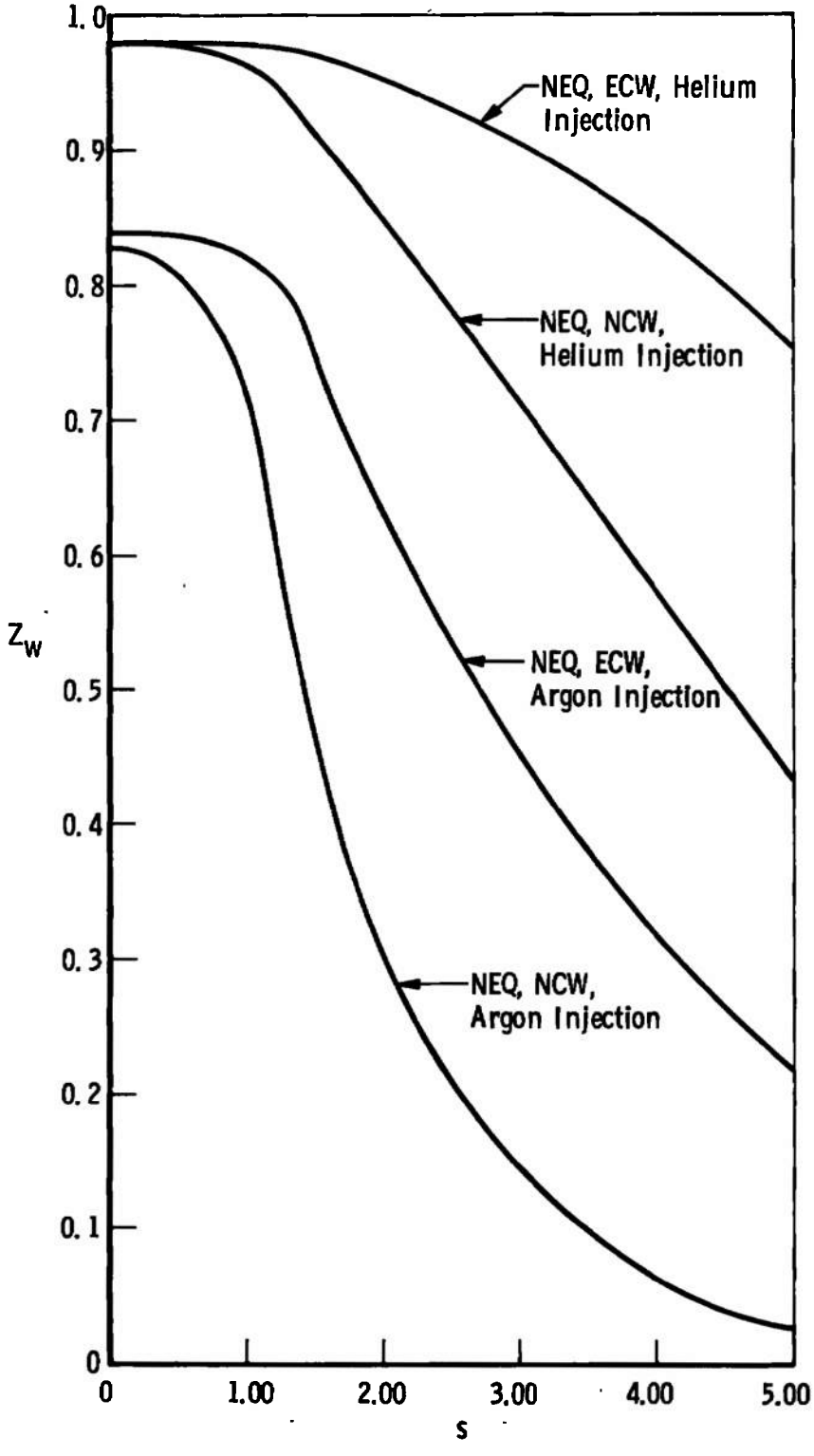

Fig. 25 Wall Mass Fraction of the Air Species under Nonequilibrium Conditions

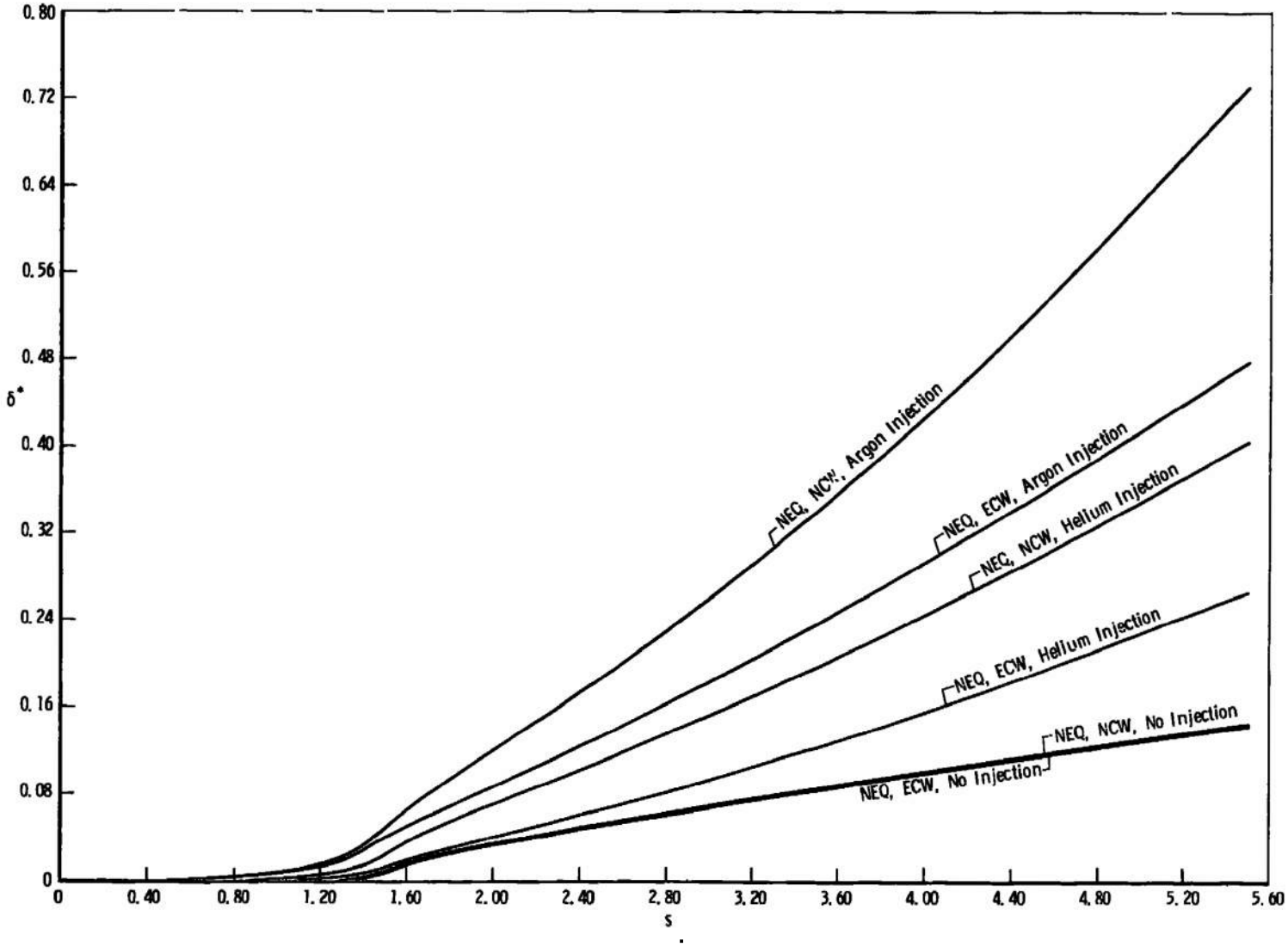

Fig. 26 Boundary-Layer Displacement Thickness Distribution under Nonequilibrium Conditions

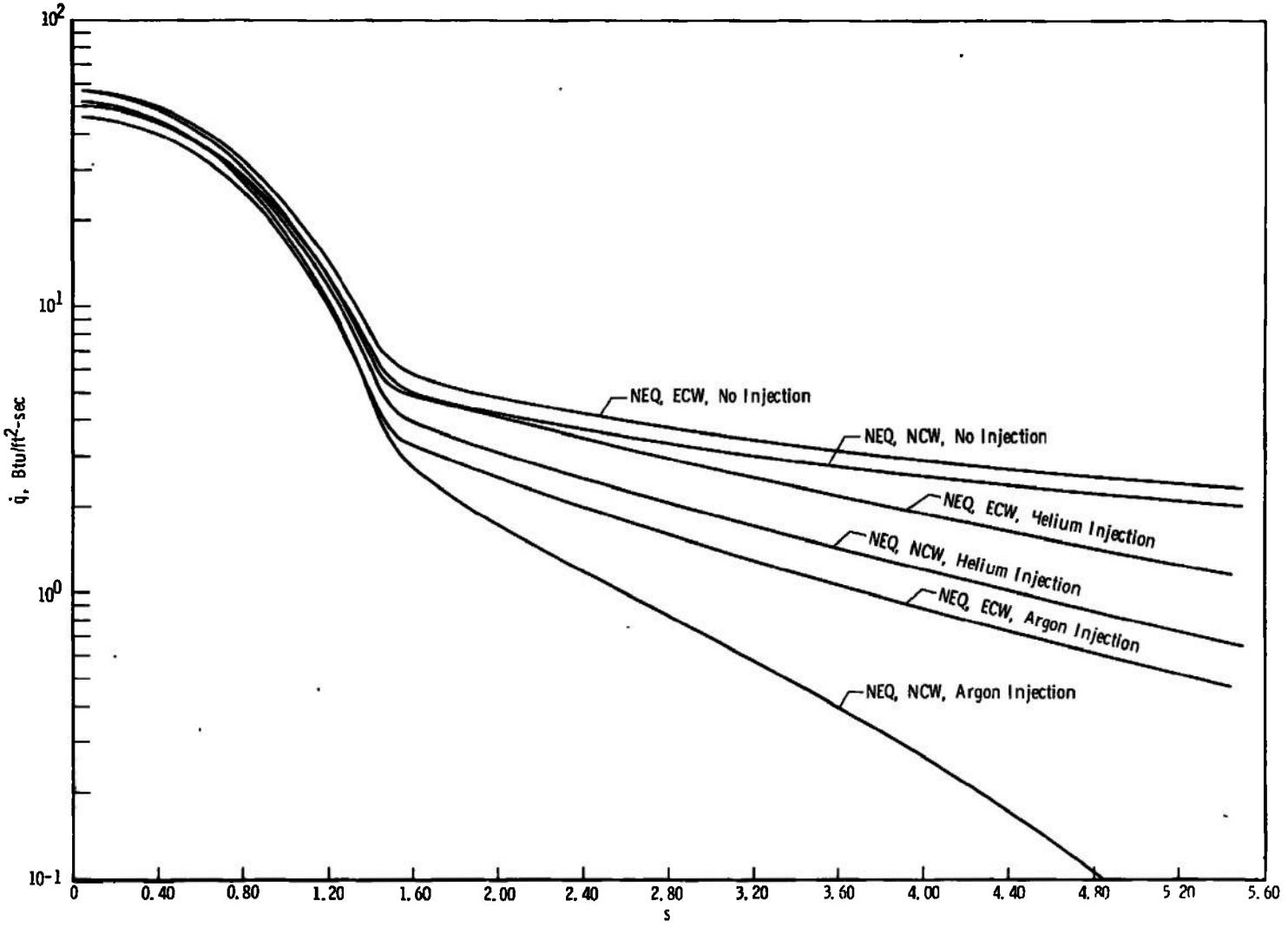

Fig. 27 Wall Heat-Transfer under Nonequilibrium Conditions

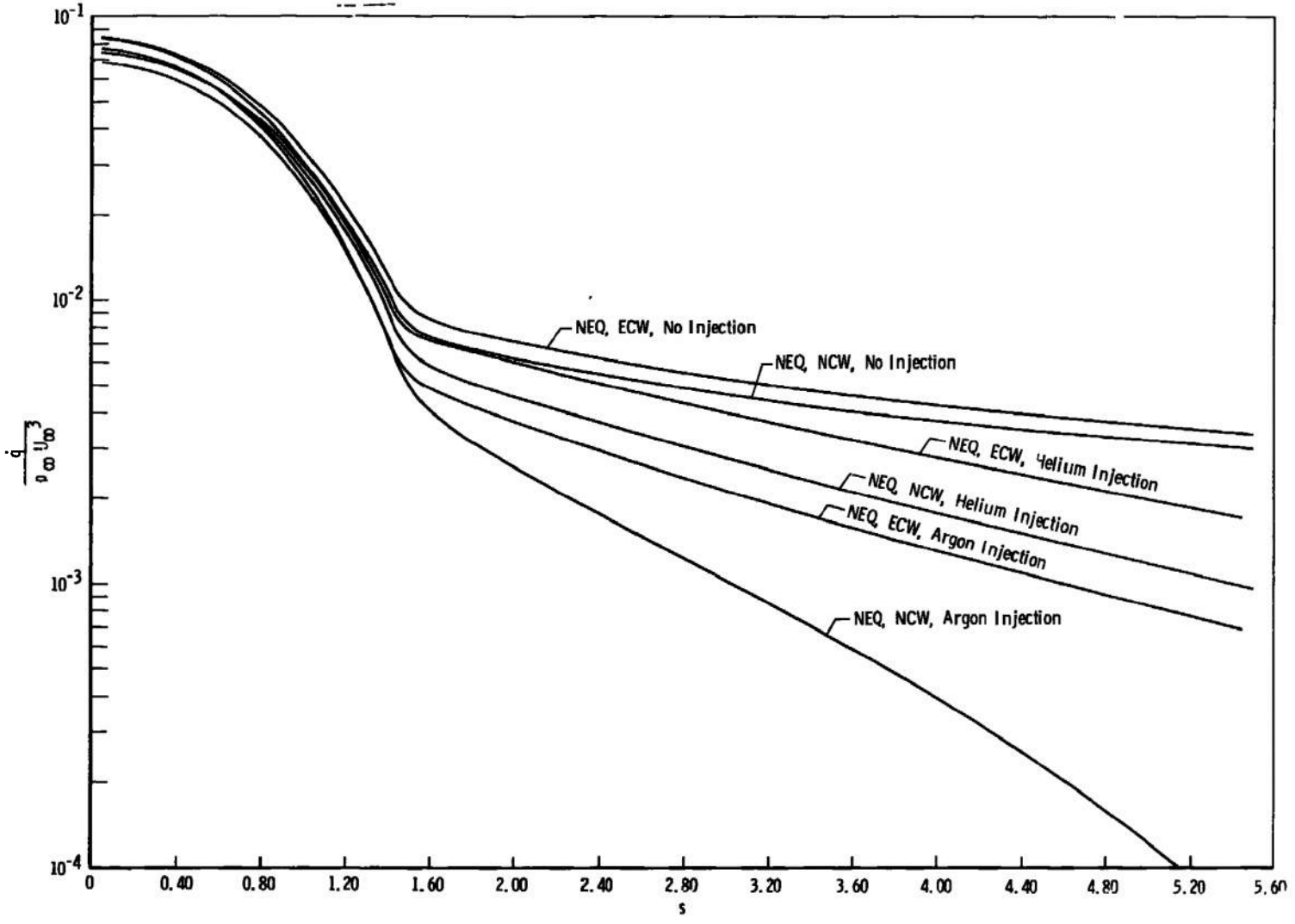

Fig. 28 Normalized Wall Heat-Transfer under Nonequilibrium Conditions

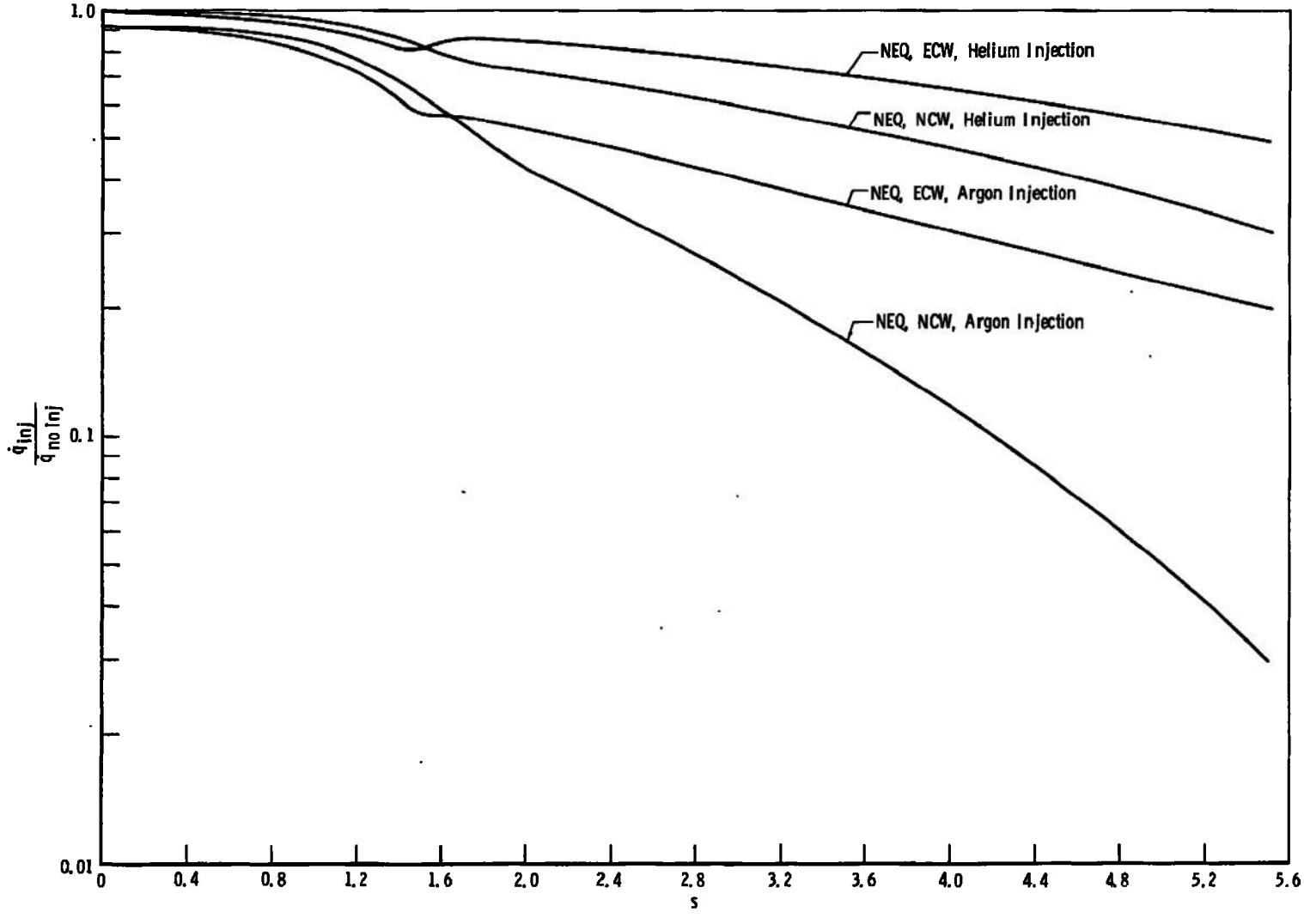

Fig. 29 Effects of Mass Injection on Wall Heat-Transfer under Nonequilibrium Conditions

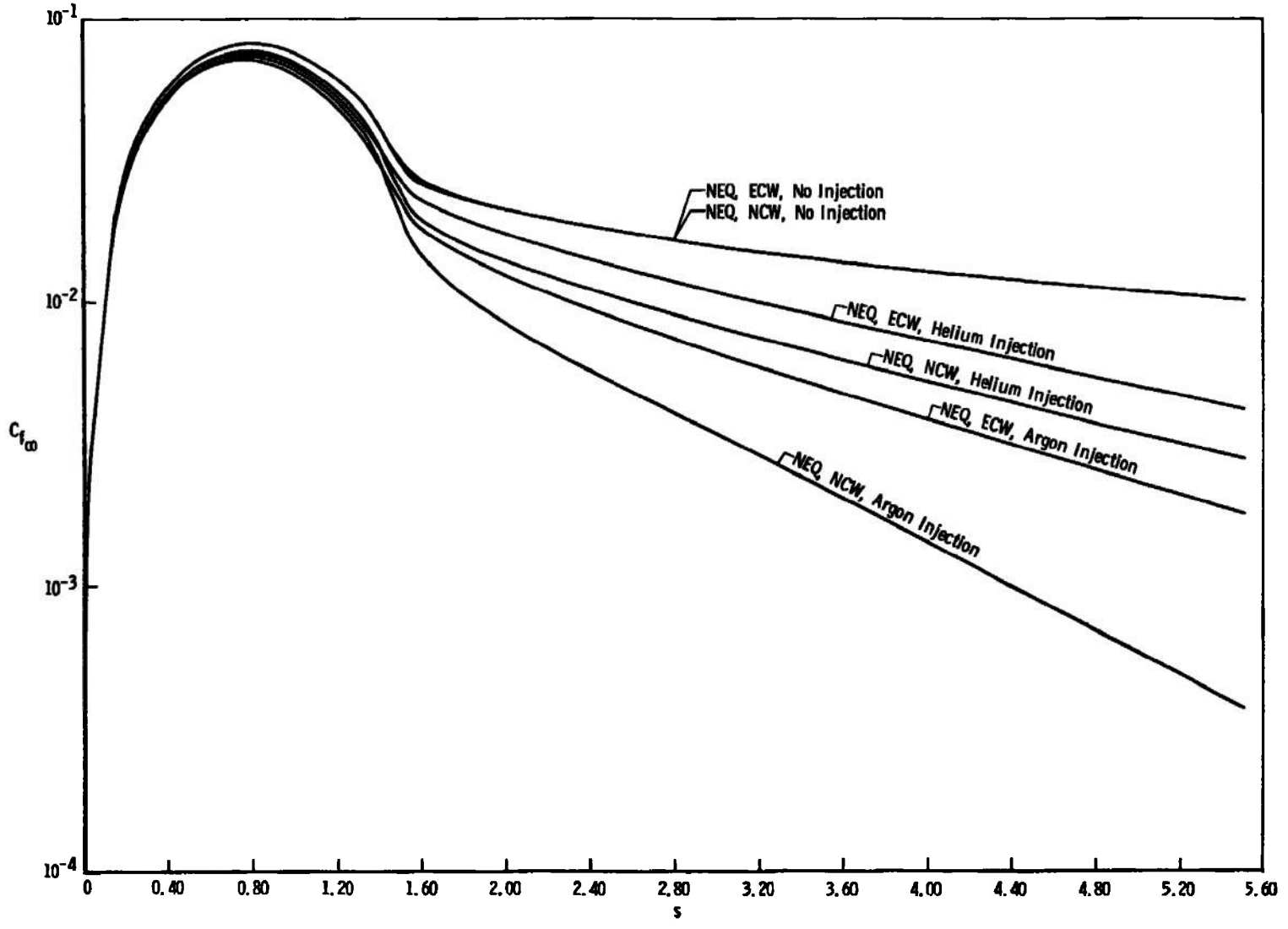

Fig. 30 Wall Skin-Friction under Nonequilibrium Conditions

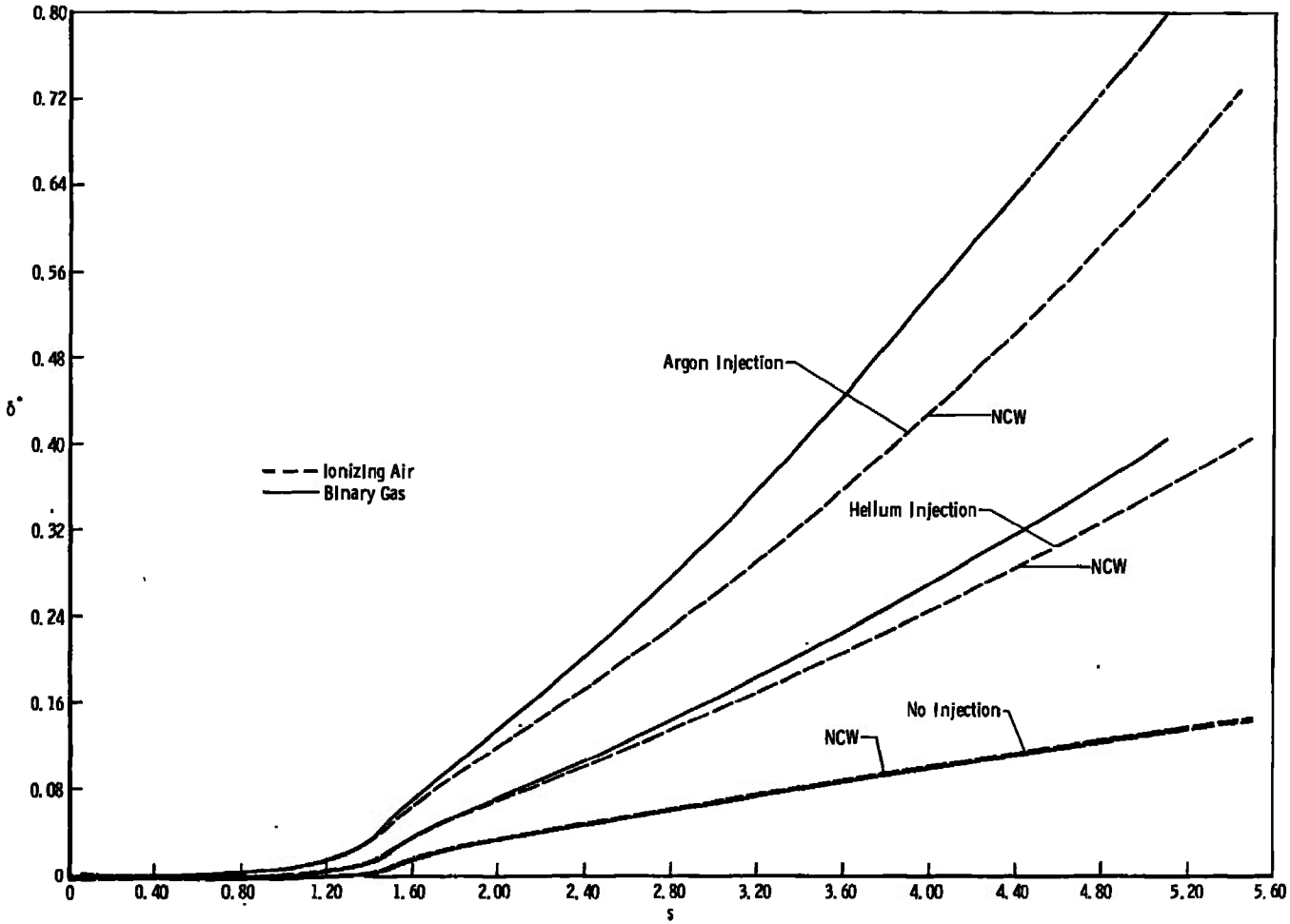

a. Displacement Thickness

Fig. 31 Comparison of Binary Gas and Ionizing Air Boundary-Layer Results without Transverse Curvature or Displacement Effects: $M_\infty = 13.2$, $\theta_c = 7.5$ deg, $T_w = 540°R$

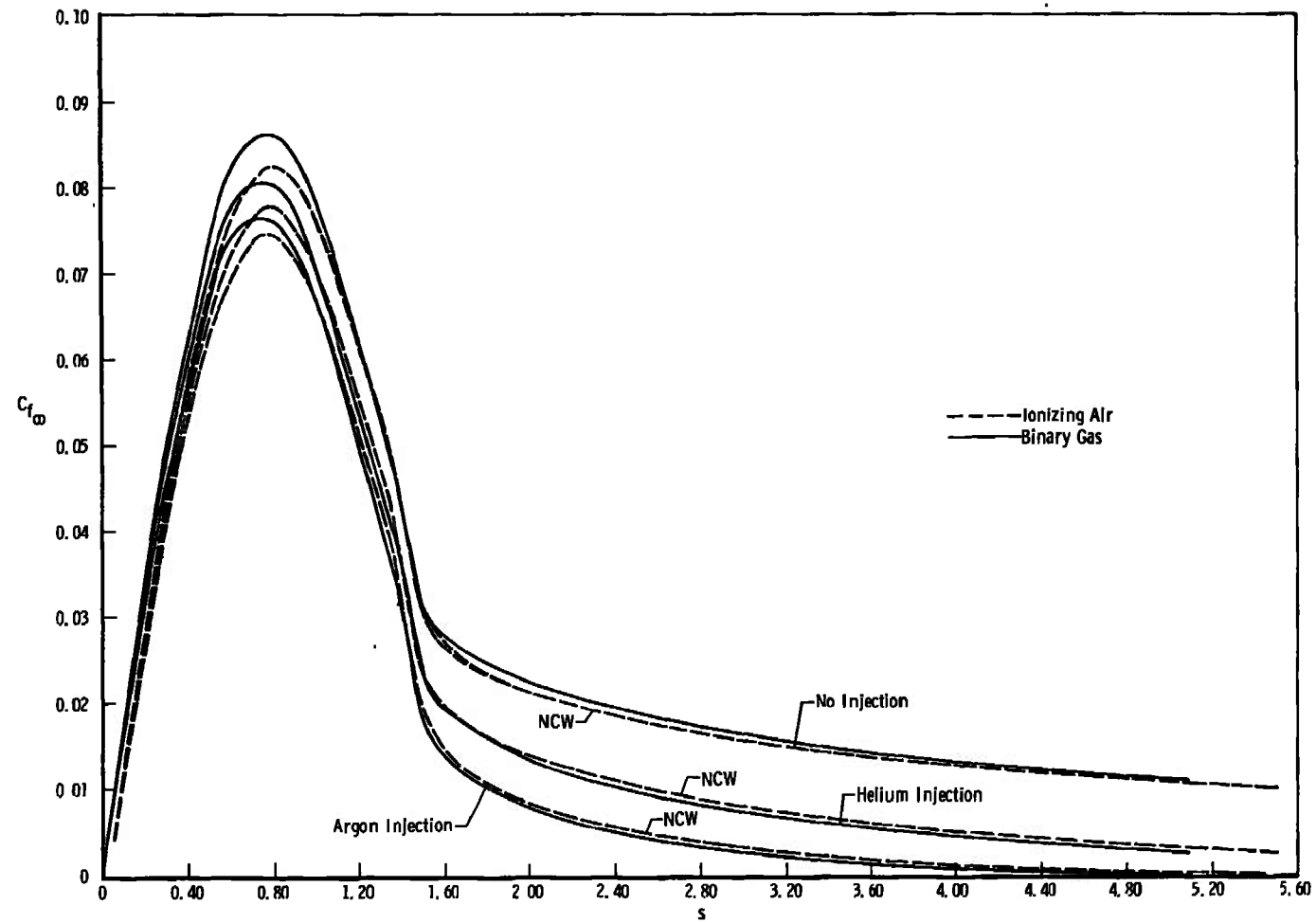

b. Skin-Friction Coefficient

Fig. 31 Continued

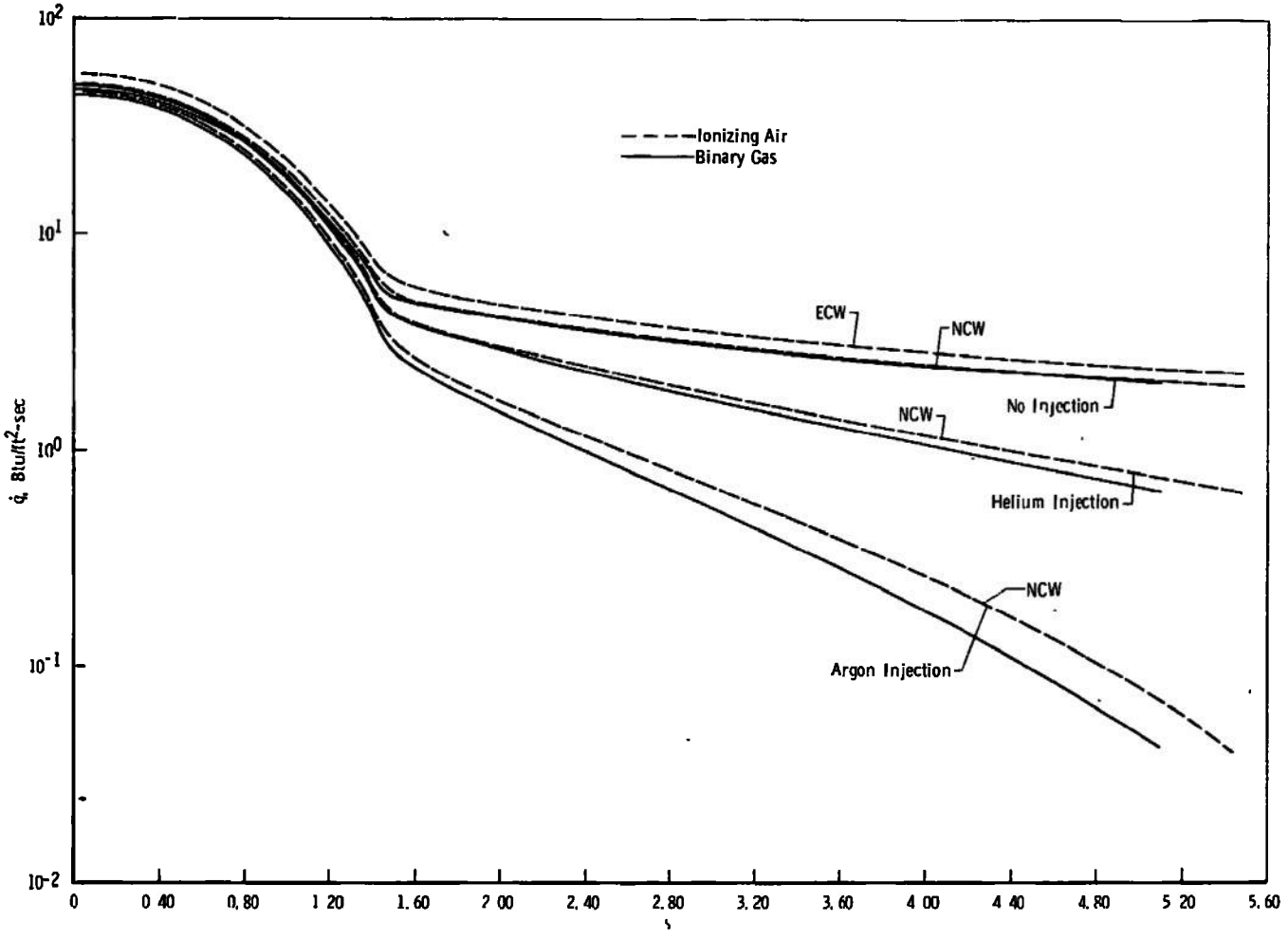

c. Dimensional Heat-Transfer Rate

Fig. 31 Continued

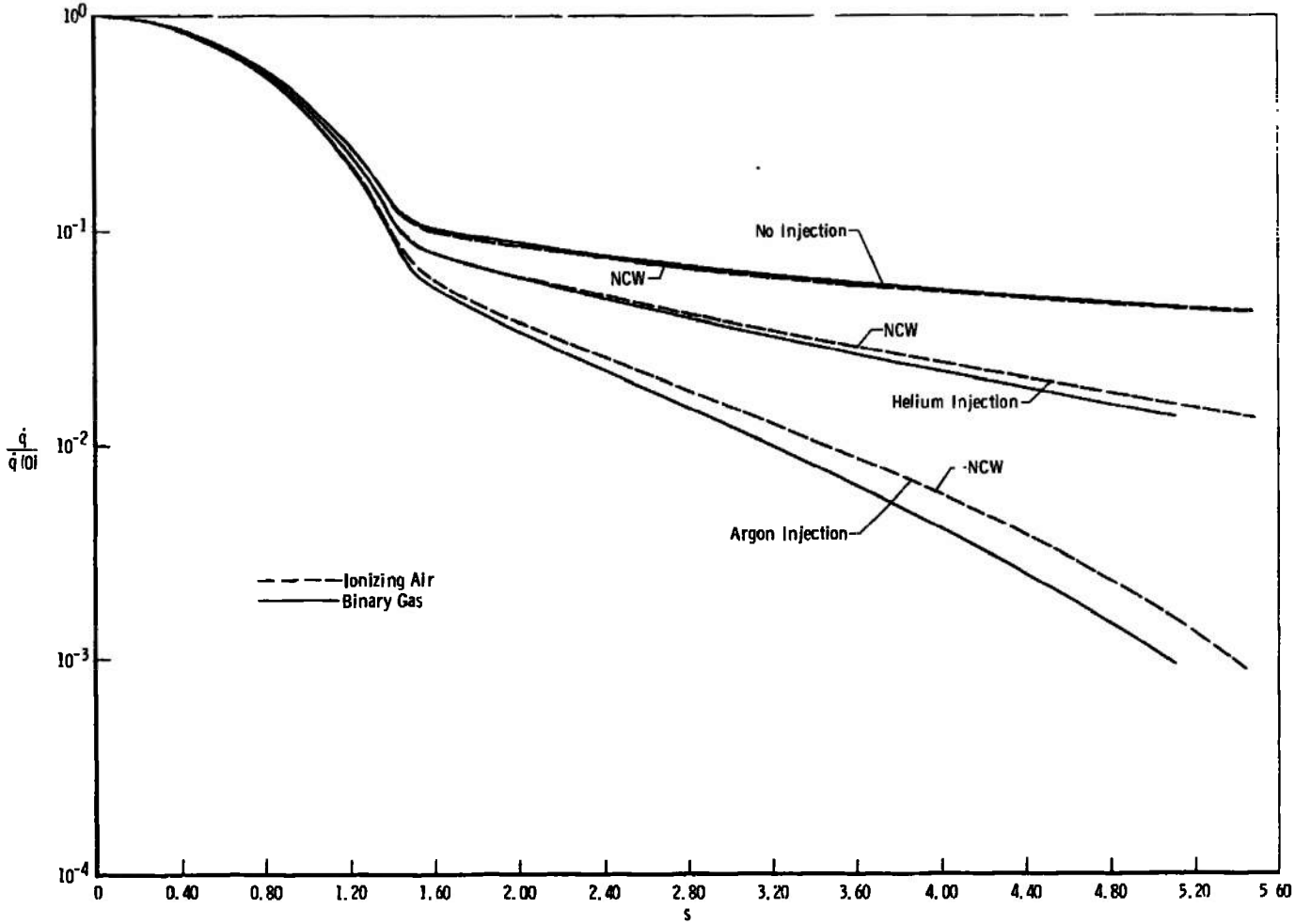

d. Heat-Transfer Ratio

Fig. 31 Continued

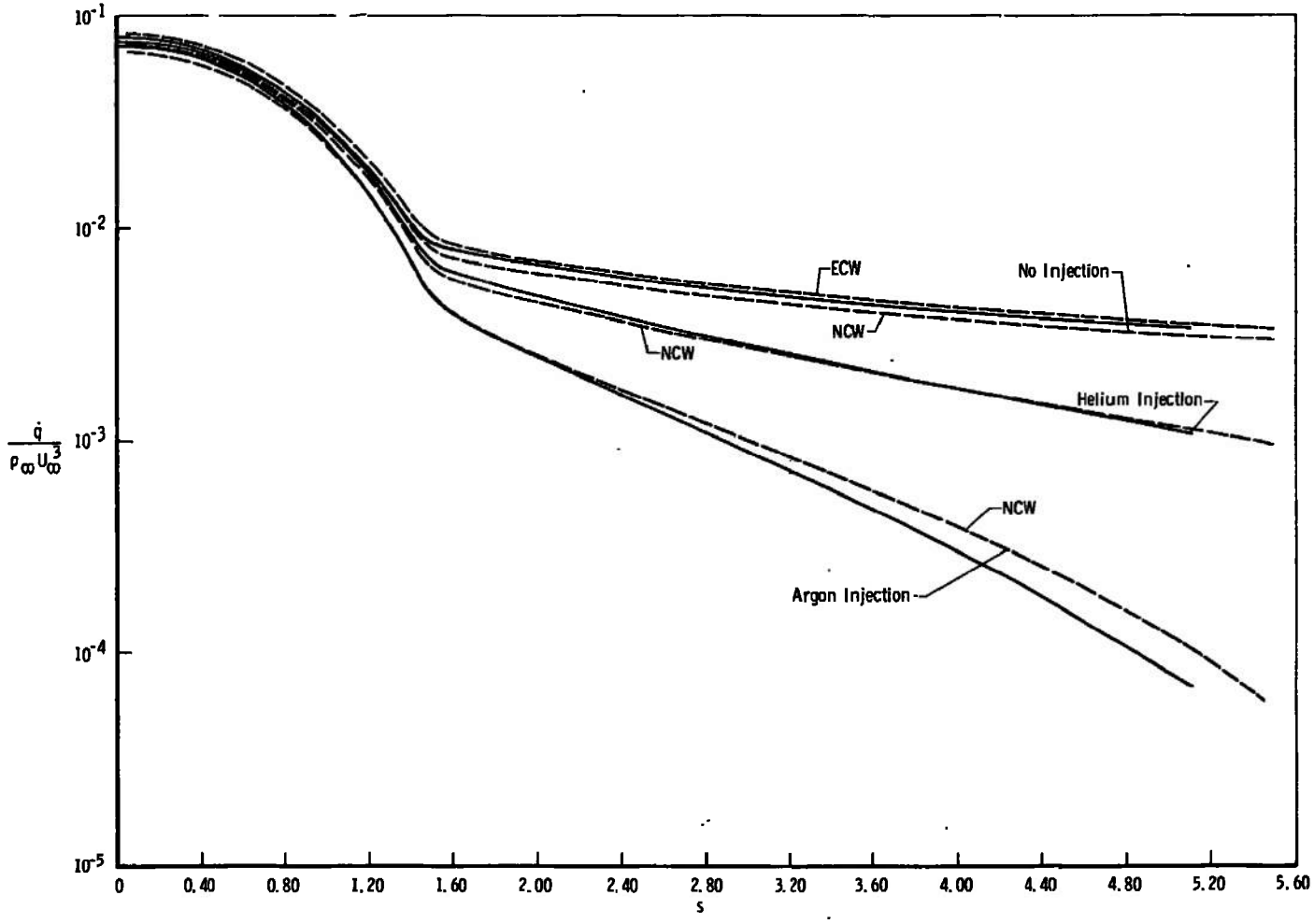

e. Dimensionless Heat-Transfer Rate

Fig. 31 Concluded

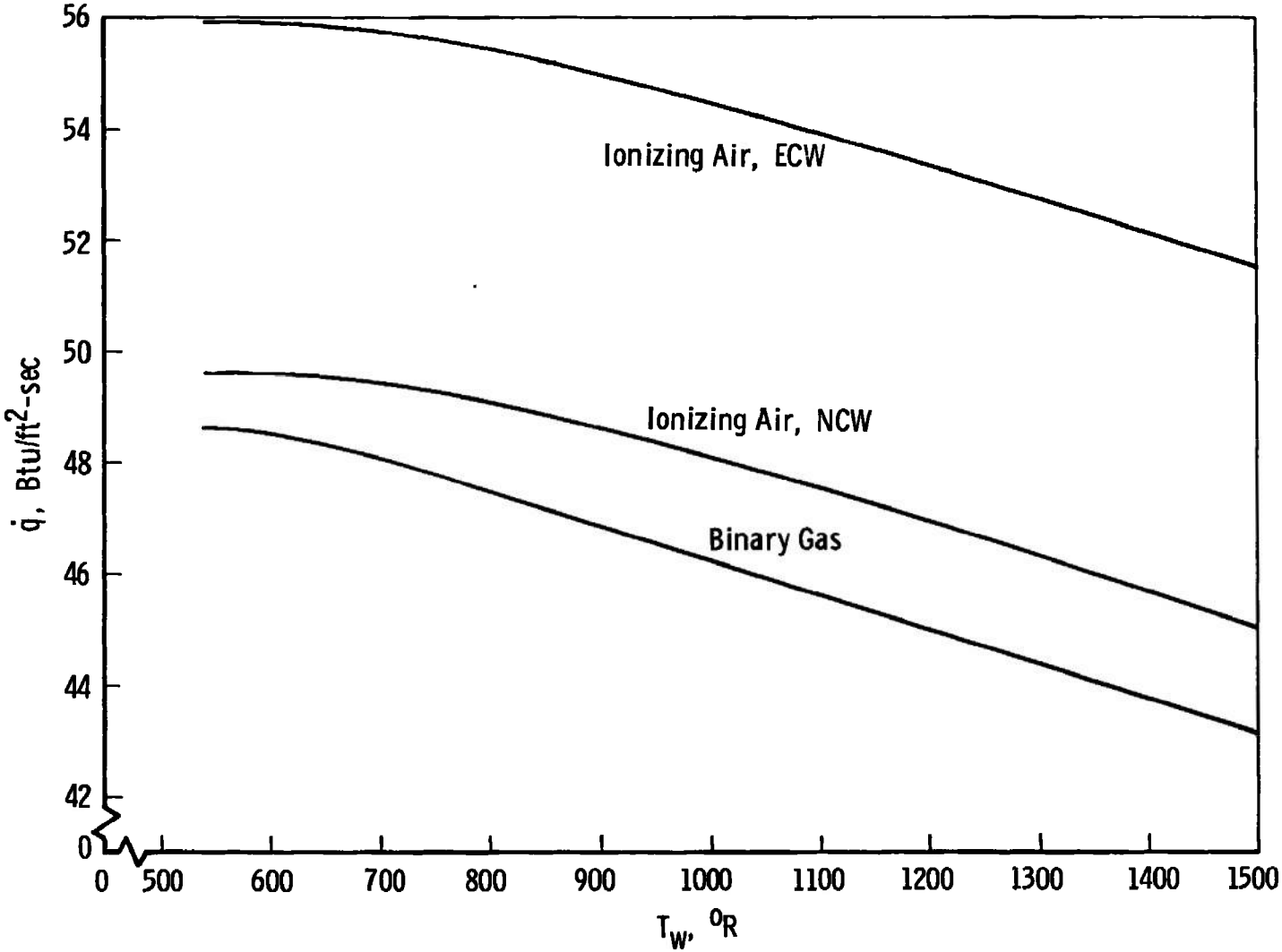

Fig. 32 Effects of Wall Temperature on No-Injection Stagnation Heat-Transfer Rate

TABLE I

FREE-STREAM AND STAGNATION CONDITIONS*

	Binary Gas Calculations	Nonequilibrium Calculations
M_∞	13.2	---
p_∞, lbf/ft^2	0.1944	0.1944
U_∞, ft/sec	10,680	10,850
T_∞, $^\circ$R	290.2	274
ρ_∞, slugs/ft^3	3.8998×10^{-7}	4.0716×10^{-7}
$\rho_\infty U_\infty$, lbf-sec/ft^3	0.004165	0.004418
p_o', lbf/ft^2	41.647	45.886
T_o', $^\circ$R	8204	8264.2
T_w, $^\circ$R	540	540
H_o, ft^2/sec^2	5.9047×10^7	6.6011×10^7
γ	1.313	---

*Free-stream chemical composition data, which are equivalent to the frozen normal shock specie concentrations, are given in Tables II, III, and IV.

TABLE II
NONEQUILIBRIUM STAGNATION POINT CONDITIONS WITH NO MASS INJECTION

	Boundary-Layer Solution NEQ Inviscid Outer Edge			Boundary-Layer Solution EQ Inviscid Outer Edge			Thin Viscous Shock Layer Frozen Normal Shock Crossing		
	Wall (NEQ,FCW)	Wall (NEQ,NCW)	Outer Edge (NEQ)	Wall (NEQ,FCW)	Wall (NEQ,NCW)	Outer Edge (EQ)	Wall (NEQ,FCW)	Wall (NEQ,NCW)	Behind Shock (Frozen)
O	0.0	2.3552-02	2.3186-02	0.0	2.3339-01	2.3146-01	0.0	2.0478-02	2.0432-02
O_2	2.3456-01	1.7634-01	1.7701-01	2.3456-01	3.2498-04	2.1200-04	2.3456-01	1.7996-01	1.8000-01
NO	0.0	6.5063-02	6.4895-02	0.0	8.7191-04	5.3410-03	0.0	6.4441-02	6.4455-02
N	0.0	1.3513-05	8.2880-05	0.0	3.3963-02	3.5750-02	0.0	7.9708-06	1.9295-09
NO^+	0.0	5.1212-09	3.5248-10	0.0	2.6158-05	6.4000-05	0.0	3.6449-08	3.6459-08
N_2	7.6544-01	7.3504-01	7.3482-01	7.6544-01	7.3143-01	7.2717-01	7.6544-01	7.3512-01	7.3537-01
$[-\dot{q}_w]_o$ (Btu/ft^2-sec)	55.94	49.61		101.63	51.22		66.68	59.63	
δ (at $f' = 0.995$)	0.0695	0.0696		0.0812	0.0819				
Δ			0.1091			0.1095	0.0753	0.0758	
p_o'(lbf/ft^2)			45.886			41.647			41.471*
T_o' ($^\circ$R)			8264.2			8204.0			8069.2**

NEQ (Nonequilibrium)
EQ (Equilibrium)
FCW (Fully Catalytic Wall)
NCW (Noncatalytic Wall)

*p_s (lbf/ft^2)
**T_s ($^\circ$R)

TABLE III

NONEQUILIBRIUM STAGNATION POINT CONDITIONS WTH ARGON INJECTION AT $\rho_w v_w = 1.182 \times 10^{-4}$ lbf-sec/ft^3

	Boundary-Layer Solution NEQ Inviscid Outer Edge			Thin Viscous Shock Layer Frozen Normal Shock Crossing		
	Wall (NEQ,ECW)	Wall (NEQ,NCW)	Outer Edge(NEQ)	Wall (NEQ,ECW)	Wall (NEQ,NCW)	Behind Shock (Frozen)
O	2.0438-40	2.0341-02	2.3186-02	2.0774-40	1.8196-02	2.0432-02
O_2	1.9646-01	1.4039-01	1.7701-01	1.8219-01	1.4905-01	1.8000-01
NO	7.4851-16	5.4120-02	6.4895-02	7.3557-16	5.5391-02	6.4455-02
N	2.0710-79	1.2308-05	8.2880-05	2.2299-79	7.5081-06	1.9295-09
NO^+	8.1040-86	4.0881-09	3.5248-10	8.4785-86	3.2054-08	3.6459-08
Argon (Inj)	1.6157-01	1.7168-01	0.0	1.4936-01	1.4442-01	0.0
N_2	6.4197-01	6.1346-01	7.3482-01	6.6845-01	6.3293-01	7.3537-01
$[-\dot{q}_w]_o$ (Btu/ft^2-sec)	51.29	45.56		61.82	55.20	
δ (at $f' = 0.995$)	0.0720	0.0720				
Δ			0.1091	0.0770	0.0773	
p_o'(lbf/ft^2)			45.886			41.471*
T_o' (^oR)			8264.2			8069.2**

ECW (Equilibrium Catalytic Wall)

*p_s (lbf/ft^2)

**T_s (^oR)

TABLE IV
NONEQUILIBRIUM STAGNATION POINT CONDITIONS WITH HELIUM INJECTION AT
$\rho_w v_w = 3.080 \times 10^{-5}$ lbf-sec/ft^3

	Boundary-Layer Solution NEQ Inviscid Outer Edge			Thin Viscous Shock Layer Frozen Normal Shock Crossing		
	Wall (NEQ,ECW)	Wall (NEQ,NCW)	Outer Edge (NEQ)	Wall (NEQ,ECW)	Wall (NEQ,NCW)	Behind Shock (Frozen)
O	2.3607-40	2.3292-02	2.3186-02	2.3645-40	2.0492-02	2.0432-02
O_2	2.2216-01	1.7118-01	1.7701-01	2.1250-01	1.7690-01	1.8000-01
NO	8.6475-16	6.3111-02	6.4895-02	8.5652-16	6.3385-02	6.4455-02
N	2.4428-79	1.3038-05	8.2880-05	2.5337-79	7.0991-06	1.9295-09
NO^+	9.4592-86	4.4639-09	3.5248-10	9.6420-86	3.5020-08	3.6459-08
Helium (Inj)	2.0138-02	2.0638-02	0.0	1.0434-02	1.5673-02	0.0
N_2	7.5770-01	7.2177-01	7.3482-01	7.7706-01	7.2355-01	7.3537-01
$[-\dot{q}_w]_o$ (Btu/ft^2-sec)	55.81	49.46		65.41	58.76	
δ (at $f' = 0.995$)	0.0651	0.0652				
Δ			0.1091	0.0753	0.0759	
p_o'(lbf/ft^2)			45.886			41.471*
T_o' ($^\circ$R)			8264.2			8069.2**

*p_s (lbf/ft^2)

**T_s ($^\circ$R)

TABLE V
CHEMICAL REACTIONS AND RATES

Reaction	Catalytic Body (M)	C_f	a_f	$e_{o,f}/k$ (^oK)	C_b	a_b	$e_{o,b}/k$ (^oK)
$O_2 + O_2 \rightleftarrows 2O + O_2$		2.3×10^{19}	-1	59,400	1.9×10^{16}	-1/2	0
$O_2 + O \rightleftarrows 2O + O$		8.5×10^{19}	-1	59,400	7.1×10^{16}	-1/2	0
$O_2 + M \rightleftarrows 2O + M$	N, N_2, NO, Inert	3.0×10^{18}	-1	59,400	2.5×10^{15}	-1/2	0
$N_2 + N_2 \rightleftarrows 2N + N_2$		3.8×10^{19}	-1	113,200	2.0×10^{18}	-1	0
$N_2 + N \rightleftarrows 2N + N$		1.3×10^{20}	-1	113,200	7.0×10^{18}	-1	0
$N_2 + M \rightleftarrows 2N + M$	O, O_2, NO, Inert	1.9×10^{19}	-1	113,200	1.0×10^{18}	-1	0
$NO + M \rightleftarrows N+O+M$	O, O_2, N, N_2, Inert	2.4×10^{17}	-1/2	75,500	6.0×10^{16}	-1/2	0
$NO + O \rightleftarrows O_2 + N$		4.3×10^{7}	3/2	19,100	1.8×10^{8}	3/2	3020
$N_2 + O \rightleftarrows NO + N$		6.8×10^{13}	0	37,750	1.5×10^{13}	0	0
$N_2 + O_2 \rightleftarrows 2NO$		2.0×10^{14}	0	61,600	1.0×10^{13}	0	40,000
$N + O \rightleftarrows NO^+ + e^-$		1.3×10^{8}	1	31,900	2.0×10^{19}	-1	0

Note: Reaction rates are from Bortner, M. H. "Chemical Kinetics in a Re-Entry Flow Field." GE TIS R63SD63, August 1963.

$k_f = C_f T^{a_f} \exp(-e_{o,f}/kT)$, cm^3/mole-sec $\qquad k_b = C_b T^{a_b} \exp(-e_{o,b}/kT)$

T in ^oK

TABLE VI
COMPARISON OF FULLY CATALYTIC WALL AND EQUILIBRIUM CATALYTIC WALL SPECIE MASS FRACTIONS UNDER NONEQUILIBRIUM CONDITIONS

Specie	Fully Catalytic Wall (FCW)	Equilibrium Catalytic Wall (ECW)
O	0.0	2.4038-40
O_2	2.3456-01	2.3451-01
NO	0.0	8.9306-16
N	0.0	2.4345-79
NO^+	0.0	9.5297-86
N_2	7.6544-01	7.6549-01

Note: Above conditions based on thin viscous shock layer analysis at the stagnation point without mass transfer.

TABLE VII
STAGNATION HEAT-TRANSFER RATE UNDER NONEQUILIBRIUM CONDITIONS

	$\left[\frac{\dot{q}_w, \text{ Thin Viscous-Shock Layer}}{\dot{q}_w, \text{ Boundary-Layer}}\right]_o$
No Injection	
NEQ, FCW	1.192
NEQ, NCW	1.202
Goldberg (Ref. 34)	≈ 1.19
Cheng (Ref. 28)	≈ 1.13
Argon Injection	
NEQ, ECW	1.205
NEQ, NCW	1.212
Helium Injection	
NEQ, ECW	1.172
NEQ, NCW	1.188

TABLE VIII
MASS TRANSFER EFFECTS ON DRAG REDUCTION

Gas Model	Displacement Iteration	TVC	Injectant	Noncatalytic Wall	Equilibrium Wall
Reacting	0	No	Argon	0.488	0.582
Reacting	0	No	Helium	0.671	0.759
Nonreacting	0	No	Argon	0.4494	---
Nonreacting	0	No	Helium	0.6501	---
Nonreacting	0	Yes	Argon	0.4502	---
Nonreacting	0	Yes	Helium	0.6578	---
Nonreacting	5	Yes	Argon	0.5299	---
Nonreacting	3	Yes	Helium	0.7395	---

*Values Given for Ratio $C_{D_f}{}_{inj} / C_{D_f}{}_{no\ inj}$

APPENDIX III
FLUID PROPERTIES USED IN THE BINARY GAS BOUNDARY-LAYER PROGRAM

To permit computations for which temperatures in the boundary layer exceed 6300°R, it was necessary to extend the range of validity of the fluid properties in the Jaffe, Lind, and Smith boundary-layer computer program (Ref. 5). The basic properties required are c_p and μ for each individual species and D_{ij} for the binary pairs of interest. Other needed species and mixture properties are calculated from these basic properties in the manner described in Ref. 5. The fluid properties have been extended to 12,600°R for the free-stream species air and the injectant species helium and argon.

The constant pressure specific heat for air from 0 to 12,600°R was taken from Dommett's data for undissociated air (Ref. 38), and was fit with two fifth-degree polynominals, one from 0 to 2000°R and another from 2000 to 12,600°R. The form of the polynominals and the values of the coefficients are given in Table III-1.

For helium and argon, only the contribution of the translational mode was considered in determining the specific heats. This results in a constant value of c_p for each of the two species of

$$c_p = (5/2)\, R$$

This does not involve any change from the data in Ref. 5, only an extension of the temperature range to which it is applied.

The viscosity of air from 90 to 720°R was computed from Sutherland's equation, and from 900 to 12,600°R the data from Peng and Pindroh (Ref. 39) at a density of 0.1 amagat were used. These two sets of data were smoothed together and fit with a fifth-degree polynominal. The form of the polynominal and the coefficients are given in Table III-2.

The viscosities of helium and argon as given in Ref. 5 were used up to 3000°R; from 3000 to 12,600°R the data of Amdur and Mason (Ref. 40) were used. These data were also fit with fifth-degree polynominals, and the coefficients are given in Table III-2.

The binary diffusion coefficients for helium and argon in air were computed using the Chapman-Enskog relation and the Lenard-Jones (6-12) intermolecular potential function. The force constants for the individual species were obtained from

Hirschfelder, Curtiss, and Bird (Ref. 41). The resulting diffusion coefficients were fitted with fifth-degree polynominals as given in Table III-3.

Plots of the various fluid properties just described are given in Figs. III-1, III-2, and III-3. These plots are from the values of the properties as computed by the appropriate fifth-degree polynominals and not the original data.

TABLE III-1
CONSTANT PRESSURE SPECIFIC HEAT OF AIR

$c_p = A + BT + CT^2 + DT^3 + ET^4 + FT^5$ $(ft^2/sec^2-{}^oR)$

Temperature	0 - 2000°R	2000 - 12,600°R
A	6.0371797×10^{3}	5.9028×10^{3}
B	$-9.4509125 \times 10^{-4}$	3.77072×10^{-1}
C	$-7.3022675 \times 10^{-4}$	9.64649×10^{-5}
D	$1.73022675 \times 10^{-6}$	-3.53769×10^{-8}
E	$-9.7657438 \times 10^{-10}$	3.48567×10^{-12}
F	$1.7465179 \times 10^{-13}$	-1.11502×10^{-16}

TABLE III-2
VISCOSITY OF AIR, HELIUM, AND ARGON

$\mu \times 10^7 = A + BT + CT^2 + DT^3 + ET^4 + FT^5$ $(lbf\text{-}sec/ft^2)$

Gas	Air	Helium	Argon
A	1.48066×10^{-1}	7.2044×10^{-1}	2.63154×10^{-1}
B	6.95936×10^{-3}	7.06794×10^{-3}	8.61381×10^{-3}
C	-1.49079×10^{-6}	-1.5363×10^{-6}	-1.84422×10^{-6}
D	2.3759×10^{-10}	2.80513×10^{-10}	3.16427×10^{-10}
E	-1.78242×10^{-14}	-2.28363×10^{-14}	-2.47897×10^{-14}
F	5.0725×10^{-19}	6.74097×10^{-19}	7.10697×10^{-19}

TABLE III-3
BINARY DIFFUSION COEFFICIENTS

$pD_{ij} = A + BT + CT^2 + DT^3 + ET^4 + FT^5$ (lbf/sec)

Species	Helium-Air	Argon-Air
A	-1.98803×10^{-1}	-6.39025×10^{-2}
B	2.31693×10^{-3}	6.67803×10^{-4}
C	2.60637×10^{-6}	1.26081×10^{-6}
D	-4.74411×10^{-11}	-1.02832×10^{-10}
E	-1.00312×10^{-14}	7.39182×10^{-15}
F	6.79428×10^{-19}	-2.18881×10^{-19}

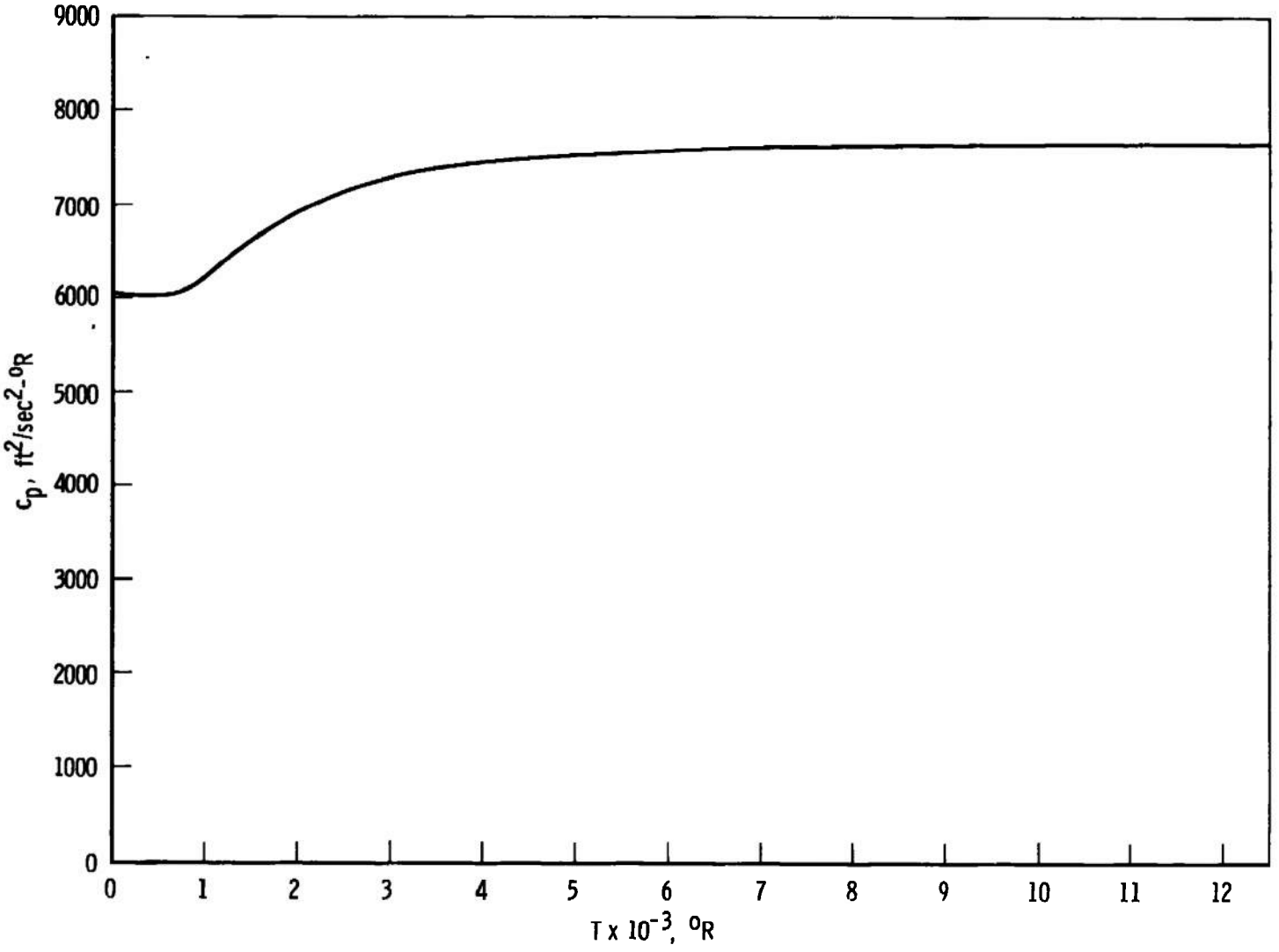

Fig. III-1 Specific Heat at Constant Pressure of Air

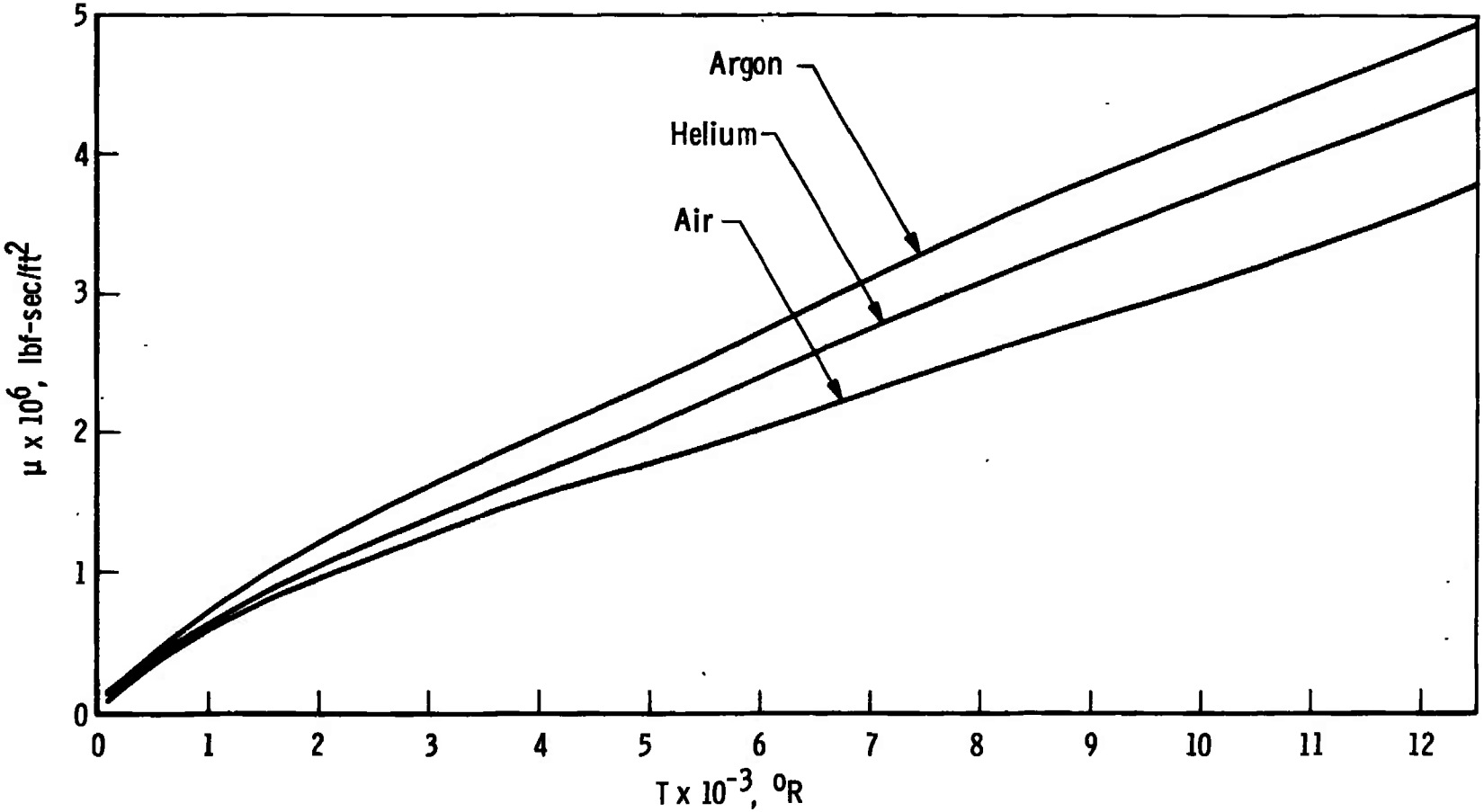

Fig. III-2 Viscosity of Air, Helium, and Argon

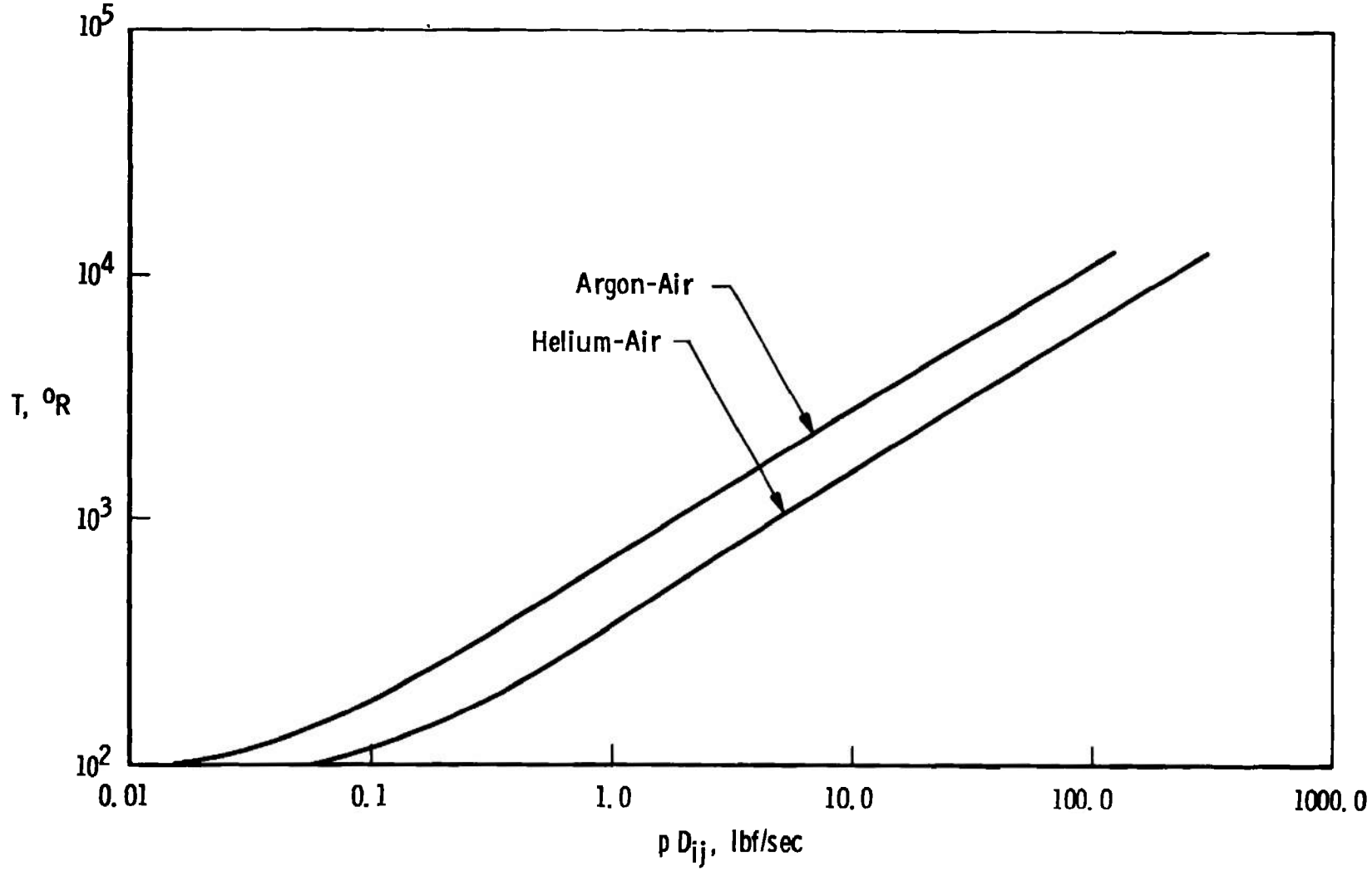

Fig. III-3 Binary Diffusion Coefficients for Helium and Argon in Air

APPENDIX IV
SURFACE HEAT-TRANSFER RELATIONS

For the case of nonreacting gas flow over a nonadiabatic surface with no mass injection, the resulting wall heat flux is given by the well-known Fourier law of heat conduction as

$$\dot{q}_w = k_w \left(\frac{\partial T}{\partial y}\right)_w \qquad \text{(IV-1)}$$

However, when the flow is chemically reacting or mass transfer is allowed, the classical definition above must be modified to include these effects. This appendix will be devoted to deriving a general surface heat-transfer expression which allows all of these effects to occur simultaneously and hence is valid for both reacting and nonreacting flows either with or without mass injection.

Following Chung (Ref. 21), the surface is assumed to be a rigid semipermeable membrane which does not allow the air species (denoted by subscript f) to flow into the porous surface but does allow the injected species (denoted by subscript i) to flow into the boundary-layer or shock layer. At the surface, energy is transported from the boundary-layer or shock layer to the surface by conduction and diffusion at the rate $\left(k \frac{\partial T}{\partial y} - \sum_{\alpha} j_\alpha h_\alpha\right)_w$ as shown in the sketch below. At the same time energy is transported away from the surface-gas interface by the normal mass flow $(\rho v)_w$ at the rate $(\rho v)_w \sum_{\alpha} C_{\alpha w} h_{\alpha w}$ and toward the solid-gas interface at the rate $(\rho v)_w \sum_{\beta} (C_{\beta w} h_{\beta w})_-$. The subscript (-) denotes the interior of the solid, whereas the subscript (β) denotes the injected species i. The subscript (α) denotes the air species f as well as the injected species i. In order to clarify this notation let us consider a six species air model (O, O_2, N, N_2, NO, NO^+) with injection of helium (He). For this example

$$f = O,\ O_2,\ N,\ N_2,\ NO,\ NO^+$$

$$i = He$$

$$\alpha = O,\ O_2,\ N,\ N_2,\ NO,\ NO^+,\ He \quad (\alpha = f + i)$$

$$\beta = He \quad (\beta = i)$$

where $(C_{\beta w})_- = 1.0$ since this quantity is evaluated in the interior of the solid and only one species is being injected. In

addition, $\sum_{\beta} (C_{\beta w})_{-} = 1.0$ and $\sum_{\alpha} C_{\alpha w} = 1.0$ are general restrictions which must be imposed in all cases.

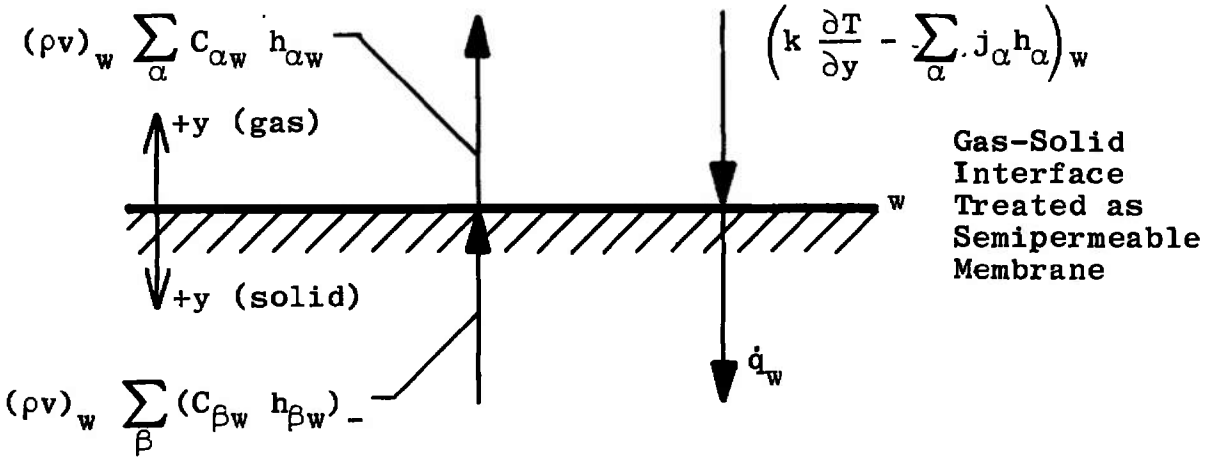

Based on the above sketch, the net rate of heat transfer into the solid is

$$\dot{q}_w = \left(k \frac{\partial T}{\partial y} - \sum_{\alpha} j_{\alpha} h_{\alpha}\right)_w - (\rho v)_w \left[\sum_{\alpha} C_{\alpha w} h_{\alpha w} - \sum_{\beta} (C_{\beta w} h_{\beta w})_{-}\right] \qquad \text{(IV-2)}$$

where a (+) value for $\dot{q}_w$ denotes heat transfer into the interior of the solid. Note that for the case of a nonreacting single species gas flow with no mass injection Eq. (IV-2) reduces to Eq. (IV-1).

In order to reduce Eq. (IV-2) to a simpler form, it is necessary to examine a mass transfer balance at the gas-solid interface as shown in the sketch below.

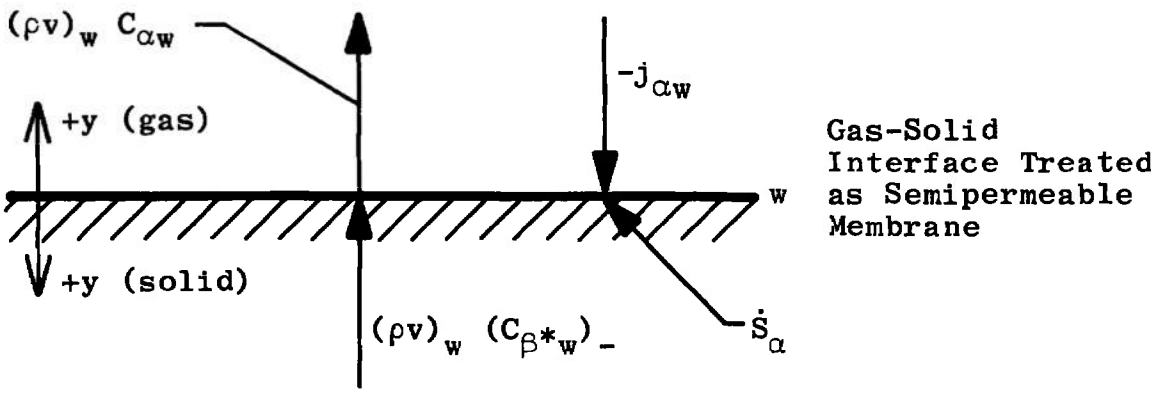

The component α is transported from the gas to the solid by diffusion at the rate $-j_{\alpha w}$. At the same time the component α is transported away from the interface by the normal mass flow $(\rho v)_w$ at the rate $(\rho v)_w C_{\alpha w}$ while the component α may possibly be transported toward the interface from within the solid at the rate $(\rho v)_w (C_{\beta^* w})_-$ where if $\beta^* \neq \alpha$, then $(C_{\beta^* w})_- = 0$. If $\beta^* = \alpha$, then $(C_{\beta^* w})_- = (C_{\alpha w})_-$ where the (-) subscript is to be interpreted as discussed previously. Summing these components gives the net rate of production of the component α by surface chemical reactions (denoted by $\dot{S}_\alpha$) as

$$\dot{S}_\alpha = j_{\alpha w} + (\rho v)_w \left[C_{\alpha w} - (C_{\beta^* w})_-\right] \qquad \text{(IV-3)}$$

For the case of a noncatalytic surface which allows no atom recombination on the surface, $\dot{S}_\alpha = 0$ for each component α. For cases in which heterogeneous chemical reactions are allowed to occur at the gas-solid interface, i.e., catalytic surface recombination of atoms, a detailed treatment of the surface chemical kinetics is required in order to evaluate $\dot{S}_\alpha$. Since the detailed theoretical treatment of the surface chemical kinetics is even more complex than that of the homogeneous ones, it will not be considered in the present work. The reader is referred to Chung (Ref. 21) for more details on this subject.

Returning to Eq. (IV-3), note that conservation of mass requires $\sum_\alpha \dot{S}_\alpha = 0$ and hence $\sum_\alpha j_{\alpha w} = 0$ since $\sum_\alpha C_{\alpha w} = 1.0$ and $\sum_{\beta^*} (C_{\beta^* w})_- = 1.0$. For the case of a noncatalytic wall ($\dot{S}_\alpha = 0$), Eq. (IV-3) reduces to

$$j_{\alpha w} = (\rho v)_w \left[(C_{\beta^* w})_- - C_{\alpha w}\right] \qquad \text{(IV-4)}$$

which yields the well-known noncatalytic wall boundary condition $j_{\alpha w} = 0$ for cases with no mass injection. Since $j_{\alpha w} \propto \left(\frac{\partial C_\alpha}{\partial y}\right)_w$ Eq. (IV-4) relates the concentration gradients to the actual concentrations for cases with mass injection through a noncatalytic surface. Furthermore, note that

$$\dot{S}_\alpha h_{\alpha w} = j_{\alpha w} h_{\alpha w} + (\rho v)_w h_{\alpha w} \left[C_{\alpha w} - (C_{\beta^* w})_-\right]$$

which results from multiplying Eq. (IV-3) by the static enthalpy of species α evaluated at the wall. Summing the above relation over all species yields

$$\sum_{\alpha} \dot{S}_{\alpha} h_{\alpha w} = \sum_{\alpha} J_{\alpha w} h_{\alpha w} + (\rho v)_w \sum_{\alpha} h_{\alpha w} \left[C_{\alpha w} - (C_{\beta^* w})_- \right] \quad \text{(IV-5)}$$

and recalling that, due to the relationship between α, β^*, and β discussed previously,

$$\sum_{\alpha} h_{\alpha w} (C_{\beta^* w})_- = \sum_{\beta} h_{\beta w} (C_{\beta w})_- \quad \text{(IV-6)}$$

Eq. (IV-2) becomes, upon substitution of Eqs. (IV-5) and (IV-6),

$$\dot{q}_w = \left(k \frac{\partial T}{\partial y} - \sum_{\alpha} \dot{S}_{\alpha} h_{\alpha} \right)_w \quad \text{(IV-7)}$$

which is an alternate form of the relation for the net rate of heat transfer into the interior of the solid. The physical interpretation of Eq. (IV-7) is clear: the right-hand side is the difference between the rate of heat conduction to the wall from the gas flow and the rate of heat absorption at the wall due to surface-catalyzed reactions, and the left-hand side is the total heat transfer into the interior of the solid. It is interesting to note that the heat carried to the surface by diffusion is precisely balanced by convection of heat due to mass transfer away from the surface and, hence, makes no net contribution to the "sensible" heat balance.

In order to evaluate Eq. (IV-7), the net rate of production $\dot{S}_{\alpha}$ must be known for each component α which, as discussed previously, is not easily evaluated for cases with surface catalyticity effects. However, for case of a noncatalytic surface, recall that $\dot{S}_{\alpha} = 0$ for each component α, and hence Eq. (IV-7) reduces to the classical form of the Fourier law of heat conduction, Eq. (IV-1), irrespective of mass injection effects. This is an important point since $\dot{S}_{\alpha} = 0$ for each α in the case of a nonreacting flow; this shows that one should properly compare nonreacting flow heat transfer with chemically reacting noncatalytic wall heat transfer in order for the comparison to have physical meaning. Furthermore, it is extremely important to note that mass transfer has no direct effect on the expression for the wall heat transfer, Eq. (IV-1), which is valid for the condition $\dot{S}_{\alpha} = 0$ irrespective of mass transfer.

In order to analyze flows with wall catalyticity effects, either Eq. (IV-2) or Eq. (IV-7) must be used. One of the most common assumptions with regard to a catalytic surface is that it be in local thermodynamic equilibrium at the given wall temperature and pressure. As discussed by Moore (Ref. 23) such an equilibrium catalytic wall condition requires a treatment of

local chemical equilibrium at the gas-solid interface including the effects of diffusion and mass injection. Since Moore describes this procedure in great detail, the reader is referred to his work for a complete description.

In summary, Eqs. (IV-2) and (IV-3) form a general set of heat and mass transfer relations at the gas-solid interface including the effects of mass injection through a porous surface considered as a rigid semipermeable membrane which does not allow the air species to flow into the porous surface but does allow the injected species to flow into the boundary-layer or shock layer. For the noncatalytic wall condition Eq. (IV-1) is the applicable heat transfer expression for cases both with and without mass injection. Furthermore, a noncatalytic wall condition must be imposed on a chemically reacting flow in order to permit meaningful comparison with nonreacting flow heat-transfer results. This restriction has obvious importance in interpreting the numerical results presented in this report and comparison with experimental wind tunnel data in a chemically reacting flow.

UNCLASSIFIED

Security Classification

DOCUMENT CONTROL DATA - R & D

(Security classification of title, body of abstract and indexing annotation must be entered when the overall report is classified)

1. ORIGINATING ACTIVITY (Corporate author)	2a. REPORT SECURITY CLASSIFICATION
Arnold Engineering Development Center ARO, Inc., Operating Contractor Arnold Air Force Station, Tennessee	UNCLASSIFIED
	2b. GROUP N/A

3 REPORT TITLE

EFFECTS OF MASS TRANSFER AND CHEMICAL NONEQUILIBRIUM ON SLENDER BLUNTED CONE PRESSURE AND HEAT-TRANSFER DISTRIBUTIONS AT M_∞ = 13.2

4 DESCRIPTIVE NOTES (Type of report and inclusive dates)

March 1 to July 15, 1968 - Final Report

5. AUTHOR(S) (First name, middle initial, last name)

Clark H. Lewis, J. C. Adams, and G. E. Gilley, ARO, Inc.

6. REPORT DATE	7a. TOTAL NO. OF PAGES	7b. NO. OF REFS
December 1968	94	41

8a. CONTRACT OR GRANT NO.	9a. ORIGINATOR'S REPORT NUMBER(S)
F40600-69-C-0001 b. PROJECT NO.	AEDC-TR-68-214
c.	9b. OTHER REPORT NO(S) (Any other numbers that may be assigned this report)
d.	N/A

10 DISTRIBUTION STATEMENT

This document has been approved for public release and sale; its distribution is unlimited.

11. SUPPLEMENTARY NOTES	12. SPONSORING MILITARY ACTIVITY
Available in DDC	NASA Ames Research Center Moffett Field, California 94035

13 ABSTRACT

The effects on the pressure and heat-transfer distributions of injecting helium and argon into an air laminar boundary layer over a spherically blunted 7.5-deg half-angle cone at M_∞ = 13.2 and Re_∞/in. = 1520 were considered. Calculations are presented for a binary perfect gas boundary layer including transverse curvature and displacement effects, an ionizing air nonequilibrium boundary layer without higher-order effects, and a nonequilibrium stagnation point thin viscous shock layer model. The effects of inviscid chemical equilibrium and nonequilibrium external conditions and wall catalyticity were investigated. Neglecting all higher-order effects, comparison of binary gas and ionizing air boundary-layer results showed reasonable agreement. Strong effects of inviscid chemical nonequilibrium on stagnation point heat transfer were found. Arguments are given for using inviscid nonequilibrium stagnation conditions rather than the usual chemical equilibrium conditions for nonequilibrium boundary-layer calculations.

DD FORM 1 NOV 65 1473

UNCLASSIFIED

Security Classification

14 KEY WORDS	LINK A		LINK B		LINK C	
	ROLE	WT	ROLE	WT	ROLE	WT
laminar boundary layers						
gas injection						
pressure distribution						
heat-transfer distribution						
helium						
argon						
chemical nonequilibrium						
nonequilibrium calculations						
conical bodies						
blunt bodies						

1. Blunted cones.
2. Cones -- Heat transfer
3. " -- Pressure distribution

1 - 2